# Multi-modal and quantitative Magnetic Force Microscopy – Application to Thin Film Systems with interfacial Dzyaloshinskii-Moriya Interaction

---

**Inauguraldissertation**
zur
Erlangung der Würde eines Doktors der Philosophie
vorgelegt der
Philosophisch-Naturwissenschaftlichen Fakultät
der Universität Basel
von

**Johannes Schwenk**

aus Deutschland

Basel, 2016

Genehmigt von der Philosophisch-Naturwissenschaftlichen Fakultät
auf Antrag von:

Prof. Dr. Hans J. Hug
Prof. Dr. Martino Poggio

Basel, den 24. Mai 2016

---

Prof. Dr. Jörg Schibler, Dekan

# Contents

# Introduction

The applications of thin film magnetism nowadays play an important role in our everyday life. Magnetic data storage devices for example, rely on magnetic thin film structures for the magnetic recording media itself as well as for the read heads of those devices. Furthermore, different types of electronic sensors exploit the properties of magnetic thin film systems, engineered specifically for the desired function and often relying on processes taking place at the nanometer scale[3].

Magnetic Force Microscopy (MFM) provides a tool for the microscopic magnetic characterization of these thin films and multilayers. An MFM is a variety of Scanning Force Microscopy (SFM). Both techniques probe the interaction arising between a sharp tip at the end of a cantilever and a sample of interest while scanning the tip over the surface of the sample. An MFM tip is equipped with a magnetic moment which leads to magnetic forces between the tip and the moments of a magnetic sample and can provide high sensitivities as well as high spacial resolution for the investigation of magnetic structures[4,5]. Only measurements in vacuum with high quality factor (Q) cantilevers can exhibit a sufficient signal-to-noise ratio (SNR) in reasonable a measurement bandwidth for a quantitative recovery of magnetic structures in the range of 10 nm. Under vacuum conditions the dual passage techniques often utilized for the tip sample distance control cannot be applied[6,7].

This thesis presents two novel techniques for the tip sample distance control in MFM suitable for vacuum conditions and for high-Q cantilevers. One of these techniques is later on used for the investigation of thin film mulitlayer samples with interfacial Dzyaloshinskii-Moria interaction. This interaction supports magnetic skyrmions in those films. Because of their topological stability magnetic skyrmions are expected to play a major role in future magneto-electronic and magnetic data storage devices.

# Outline of the thesis

Objective of the thesis was the development of improved distance control methods for quantitative Magnetic Force Microscope (MFM) measurements in vacuum, and the application of these techniques for the analysis of micromagnetic states in materials with interfacial Dzyaloshinskii-Moriya (DM) interaction.

Chapter 1 introduces the concepts of non-contact SFM. The specific challenges of distance control in the case of MFM are discussed. Furthermore, the methods of quantitative MFM as applied in this thesis are introduced.

Instrumental developments required to perform the measurements presented in this thesis and demagnetization procedures for samples are discussed in chapter 2.

Chapters 3 and 4 present two novel single passage measurement methods that use bimodal cantilever excitation suitable for operation in air and in vacuum. These are suitable for measurements performed in vacuum, and can map the topography and magnetic stray field of a sample simultaneously. The first method relies on the essentially different decay length of tip sample interactions of topographic and magnetic origin. The second method utilizes the tip sample capacitance as a proxy for the tip sample distance the tip sample distance which allows for a feedback which is independent from other conservative tip sample interactions.

The capacitive tip sample distance control method is applied for quantitative MFM measurements on multilayer samples with interfacial DM interactions presented in chapter 5. Data with substantially higher signal to noise ratios and lateral resolution in comparison to existing studies[8] are obtained from these measurements. Based on the quantitative analysis of the data, a significant local variation of the DM interaction in our mulitlayer systems was found.

# 1 Introduction to Magnetic Force Microscopy

A MFM is a type of Scanning Force Microscope (SFM) that is equipped with a ferromagnetic probe in order to measure the magnetic stray field above a sample of interest. Therefore, the general concepts of SFM are introduced in the next section 1.1 though the focus is MFM application.

## 1.1 SFM and MFM

A Scanning Force Microscope uses a sharp tip at the free end of a cantilever beam to map the interaction forces between tip and sample. The topographical structure and physical properties of the sample determine the local tip sample interaction. An image of the sample can be obtained from a measurement of the local tip sample interactions while scanning the tip laterally over the sample. This has been shown first in 1986 by G. Binnig C.F. Quate and C. Gerber and referred to as *Atomic Force Microscopy*[9]. A cantilever based SFM is illustrated in figure 1.1.

### 1.1.1 Cantilever deflection measurement

The interactions between tip and sample change the mechanical properties of the cantilever. The latter can be determined by a measurement of the time-dependent deflection of the cantilever. The deflection sensor has originally been implemented by a tunnel current setup but can also utilize a capacitance measurement, a piezoresistive or a piezoelectric coating on the cantilever or interferometry[4]. Today, most commercial instruments, like the one used in this thesis, make use of a beam de-

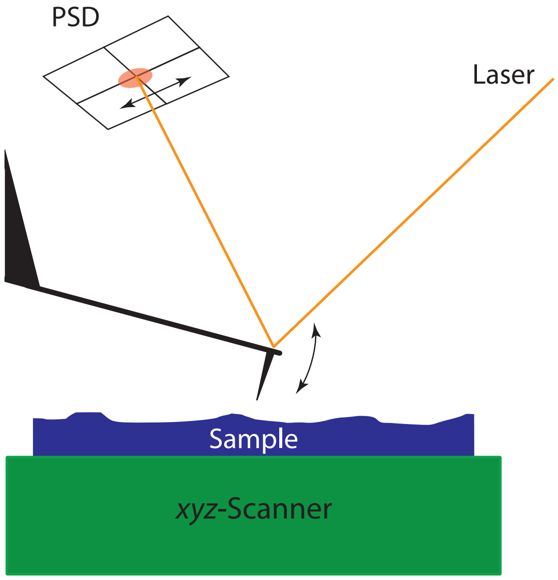

Figure 1.1: A cantilever based SFM brings the sharp tip at the end of a cantilever in close proximity to the surface of a sample. The optical lever or beam deflection technique that uses a PSD and a laser reflected on the backside of the cantilever in order to detect its deflection is illustrated.

flection sensor, similar to the illustration in figure 1.1. In this setup a laser beam is reflected from the backside of the cantilever and a position sensitive photodetector (PSD) is placed in the reflected beam path. In this way, depending on the distance between cantilever and photodetector, a small deflection of the cantilever causes a displacement of the laser spot on the detector. The detector consists of 4 photosensitive quadrants such that the difference in light intensity on the quadrants is a measure of the cantilever deflection. The flexural deflection is measured by the difference between the two upper and two lower quadrants whereas a torsion of the cantilever leads to a difference between the two left and two right ones. The measured electronic signal obtained from the PSD is proportional to the cantilevers bending at the point where the laser is reflected at the backside of the cantilever and to the reflected laser intensity. This proportionality is the sensitivity of the beam deflection sensor and typically measured in volts per nanometer.

### 1.1.2 Operation modes

In so called *contact mode* SFM measurements the tip is brought into direct contact to the sample's surface. A constant load is applied to the tip by keeping a predefined bending of the cantilever i.e., by moving the support of the cantilever up or down while scanning over the sample. The resulting trajectory of the cantilever support is a convolution of the sample's topography and the SFM tip. The tips for this operation mode have to provide a high structural stability and are thus relatively blunt. Magnetic or electrostatic forces acting between tip and sample change the deflection of the cantilever very little, because the tip sample contact exhibits a high stiffness.

In *non-contact mode*, where the tip is scanned in close proximity above the sample surface, a much better sensitivity for tip sample forces is achieved. Therefore, MFM measurements are most commonly carried out in this mode. In such a measurement the tip sample forces, among them magnetic forces, lead to a static deflection of the cantilever at each scanning position. However, a measurement of the static deflection of a cantilever is affected by instrumental drift which leads to force offsets during a measurement. Additionally, $1/f$-noise limits the signal-to-noise ratio of static measurements. A dynamic detection of the tip sample interaction can overcome these limitations[10,11,12] and, since the preferred detection method in MFM, is described in the following section 1.1.3.

### 1.1.3 Cantilever dynamics

The dynamic non-contact mode in SFM is based on the dynamics of an oscillating cantilever beam to measure tip sample interactions.

A cantilever beam exhibits multiple resonant oscillation modes. The SFM cantilever is modelled by a beam with a clamped and a free end. The assumption of a free end of the cantilever only holds when the tip sample force gradients are small in comparison to the cantilever stiffness. The envelope of a specific oscillation mode $z_n$ of such a beam is described by equations 1.2 and 1.2 as a function of the position $\xi$ along the cantilever[13,14].

$$\begin{aligned} z_{\mathrm{n}}(\xi) &= \frac{A_{\mathrm{n}}}{2}\left[\cos(\alpha_{\mathrm{n}}\xi/l) - \cosh(\alpha_{\mathrm{n}}\xi/l)\right. \\ &\left. - \frac{\cos(\alpha_{\mathrm{n}}) + \cosh(\alpha_{\mathrm{n}})}{\sin(\alpha_{\mathrm{n}}) + \sinh(\alpha_{\mathrm{n}})}\left(\sin(\alpha_{\mathrm{n}}\xi/l) - \sinh(\alpha_{\mathrm{n}}\xi/l)\right)\right] \end{aligned} \tag{1.1}$$

with:

$$\cos\left(\alpha_{\mathrm{n}}\right)\cosh\left(\alpha_{\mathrm{n}}\right) = -1 \tag{1.2}$$

The parameter $l$ is the length of the cantilever and the amplitude $A_{\mathrm{n}}$ describes the maximum deflection, obtained for the specific oscillation mode, at the free end $\xi = l$ of the cantilever. The eigenvalues $\alpha_{\mathrm{n}}$ are given by the solutions of equation 1.2 and listed in table 1.1 for n=1...5. The resulting shapes for the first three oscillation modes are illustrated in figure 1.2. Since a beam deflection sensor measures the slope of the cantilever instead of the the deflection amplitude at the end of the cantilever, the different slopes at the cantilever end for different oscillation modes, all with the same amplitude $A_{\mathrm{n}} = A_0$, lead to a different optical sensor sensitivity for each mode. The increase of the sensitivity for higher modes is therefore defined by the ratio of the derivatives at the cantilevers free end $z'_{\mathrm{n}}(\xi = l)/z'_1(\xi = l)$ and listed in table 1.1.

| n | $\alpha_{\mathrm{n}}$ | $f_{\mathrm{n}}/f_1$ | $k_{\mathrm{n}}/k_1$ | $z'_{\mathrm{n}}(l)/z'_1(l)$ |
|---|---|---|---|---|
| 1 | 1.87510 | 1 | 1 | 1 |
| 2 | 4.69409 | 6.26692 | 39.2743 | 3.473 |
| 3 | 7.85476 | 17.5476 | 307.917 | 5.702 |
| 4 | 10.9955 | 34.3860 | 1182.39 | 7.989 |
| 5 | 14.1372 | 56.8431 | 3231.14 | 10.27 |

Table 1.1: Numerical values for $\alpha_{\mathrm{n}}$ resembling the solutions of equation 1.2, and the related ratios for higher modes frequencies, the respective modal stiffness values and the slope at the free cantilever free end.

The resonance frequencies of those oscillation modes are given by equation 1.3[14] and depend on the cantilever dimensions namely thickness $t$ and length $l$, and the material properties mass density $\rho$ and the Young's modulus $E_{\mathrm{mod}}$ of the material.

$$f_{\mathrm{n}} = \frac{\alpha_{\mathrm{n}}^2}{2\pi l^2}\sqrt{\frac{E_{\mathrm{mod}} t^2}{12\rho}} \tag{1.3}$$

Furthermore, the motion of the tip at the free end of the cantilever can be described by a point mass model where the resonance frequency of its harmonic oscillation is[15]

$$f_{\mathrm{n}} = \frac{1}{2\pi}\sqrt{\frac{k_{\mathrm{n}}}{m^*}}\ . \tag{1.4}$$

Here $m^*$ is an effective mass and $k_{\mathrm{n}}$ a modal stiffness in z-direction. For the first resonance it is related to the resonance frequency by[16]

$$k_1 = \frac{2\pi^3\sqrt{12^3}}{\alpha_1^6} \cdot \frac{w\left(l f_1 \sqrt{\rho}\right)^3}{\sqrt{E_{\mathrm{mod}}}} = 59.3061 \cdot \frac{w\left(l f_1 \sqrt{\rho}\right)^3}{\sqrt{E_{\mathrm{mod}}}}. \tag{1.5}$$

Thus, the first-mode cantilever stiffness can be determined from the measured resonance frequency $f_1$, the E-modulus and the specific mass $\rho$ of the cantilever material[1], and the width $w$ and the length $l$ of the cantilever. Taking into account the same effective mass $m^*$ for all modes[19] in equation 1.4 we find $k_{\mathrm{n}} \propto \alpha_{\mathrm{n}}^4$. According to this, the ratios for higher mode stiffnesses $k_{\mathrm{n}}$ and resonance frequencies $f_{\mathrm{n}}$ are given in table 1.1. It is important to note that the higher oscillation modes are not harmonics of the first one. The cantilever can be driven at any of its oscillation modes. For a selected drive frequency $f$ and applied driving force $F_{\mathrm{exc}}$ the steady-state oscillation amplitude becomes[15]:

$$A_{\mathrm{n}}(f) = \frac{F_{\mathrm{exc}}}{4\pi^2 m^* f_{\mathrm{n}}^2} \cdot \left(\sqrt{\left(1-\frac{f^2}{f_{\mathrm{n}}^2}\right)^2 + \left(\frac{f}{f_{\mathrm{n}} Q_{\mathrm{n}}}\right)^2}\right)^{-1}. \tag{1.6}$$

As depicted in figure 1.3 the dimensionless quality factor $Q_{\mathrm{n}}$ defines the width of the resonance peak which, for $Q_{\mathrm{n}} \gg 1$, is $\sqrt{3} \cdot f_{\mathrm{n}}/Q_{\mathrm{n}}$ at amplitudes of $A(f_{\mathrm{n}})/2$ and $f_{\mathrm{n}}/Q_{\mathrm{n}}$ at $A(f_{\mathrm{n}})/\sqrt{2}$ respectively.

---

[1] For silicon cantilevers the material properties are: $\rho_{\mathrm{Si}} = 2330\,\frac{\mathrm{kg}}{\mathrm{m}^3}$[17] and $E_{\mathrm{mod,Si}} = 169\,\mathrm{GPa}$[18]

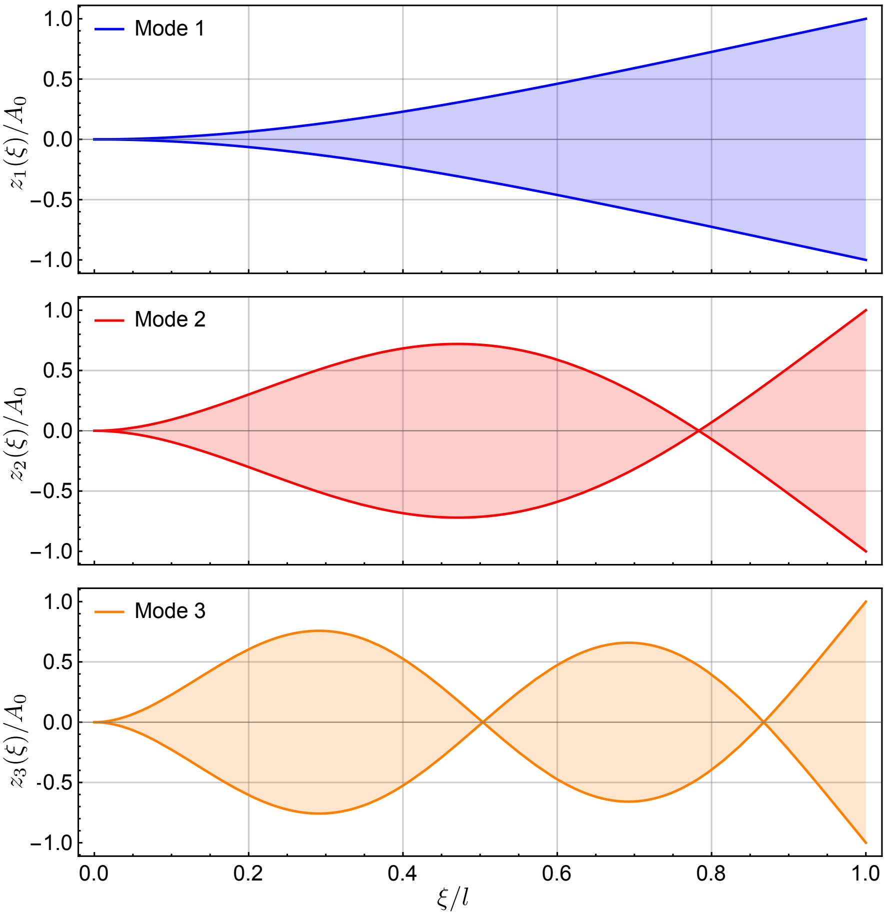

Figure 1.2: Position dependent envelopes for a cantilever oscillating with a maximum deflection $A_0$ at the free end, illustrated for the first three resonant oscillation modes. The different slopes at the free end of the cantilever cause different sensitivities of a beam deflection detector for different modes. The relative slopes are listed in table 1.1.

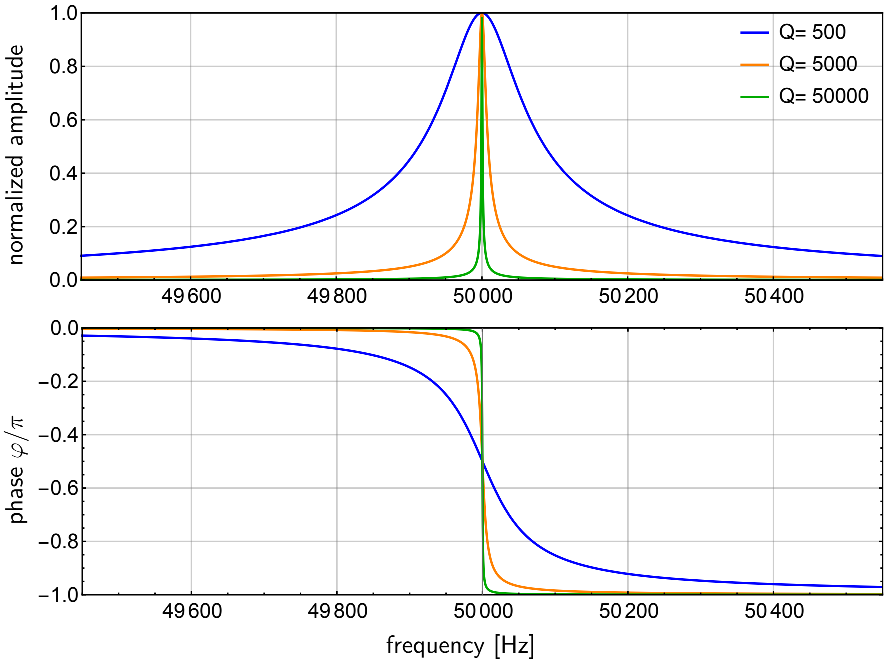

Figure 1.3: Plot of resonance curves for quality factor values of $Q = 500$ (blue), $Q = 5000$ (orange) and $Q = 50000$ (green) and for a resonance frequency of 50 kHz. The range of quality factors resembles the typical difference between ambient and UHV operation conditions.
*Upper:* Amplitude response as a function of the driving force frequency.
*Lower:* Phase lag between the cantilever oscillation and the drive oscillation as a function of the driving force frequency.

### 1.1.4 Quality factor of SFM cantilevers

The minimum measurable force for a given SFM cantilever and resonance mode depends on the quality factor $Q_\mathrm{n}$, as described in section 1.1.6. High quality factors are required for sensitive measurements of small tip sample interactions such as the force gradients related to magnetic structures of small lateral size. Low noise measurements of these force gradients are a prerequisite for a quantitative analysis of high resolution MFM data.

Besides the relation between the resonance's width and the quality factor of the respective oscillation mode given in section 1.1.3, the quality factor also describes the energy loss per cycle $\Delta W_\mathrm{n}$[20]:

$$Q_\mathrm{n} = 2\pi \frac{W_\mathrm{n}}{\Delta W_\mathrm{n}}, \tag{1.7}$$

where $W_\mathrm{n}$ is the total energy stored in the oscillation mode. The total energy loss per oscillation cycle is the sum of various energy loss processes of different physical nature. Hence, the total quality factor $Q_\mathrm{n}$ becomes[20]:

$$\frac{1}{Q_\mathrm{n}} = \frac{1}{Q_\mathrm{env}} + \frac{1}{Q_\mathrm{clamping}} + \frac{1}{Q_\mathrm{TED}} + \frac{1}{Q_\mathrm{volume}} + \frac{1}{Q_\mathrm{surface}} + \ldots\ . \tag{1.8}$$

The most important term is $Q_\mathrm{env}$ which describes the energy loss processes arising from the motion of the cantilever withing the medium surounding it. In air, the cantilever quality factor is reduced to typically 300-500 while the same cantilever can reach 150 k - 200 k under ultra high vacuum (UHV) conditions. A prerequisite for a significant influence of any of the other dissipation mechanisms is thus the absence of viscous damping caused by gaseous or, more crucially, liquid media around the cantilever. Clamping losses arise from the high strain at the attachment point of the cantilever to its support chip structure and are estimated as[20] $Q_\mathrm{clamping} \approx 2.17 \cdot l^3/t^3$. The third contribution, the thermoelastic dissipation (TED), is caused by the opposing expansion and compression of the cantilever material on the upper and lower side of the cantilever during each half oscillation cycle. This leads to respective cooler and warmer spots followed by a dissipative heat flow among them. This mechanism becomes negligible for cantilevers with a thickness $t < 2\,\mu$m because of the reduced strains. The term $Q_\mathrm{volume}$ refers to dissipation processes at the atomic scale, for example arising from strain-induced positional changes of atoms at lattice dislocations. Yasumara et. al[20] showed that for long, narrow and thin single crystalline SFM cantilevers, where $l \gg w \gg t$ and $t < 2\,\mu$m, the terms $\frac{1}{Q_{\text{clamping}}}$, $\frac{1}{Q_{\text{TED}}}$ and $\frac{1}{Q_{\text{volume}}}$ are negligible. In this case, losses arising from thin layers of different material at the cantilever surfaces become the limiting factor for the cantilever's quality factor. Different Young´s modulus of surface layers and bulk material and dissipation within the surface layers, contribute to this energy loss process. For thin surface layers with thickness $\sigma$, modelling[20] shows that $Q_{\text{surface}} \propto {}^{t}\!/\!_{\sigma}$. For uncoated cantilevers, a surface layer is present in the form of various adsorbates as for example water. The thickness of these layers can therefore be reduced by baking the cantilever in vacuum or controlled gas atmosphere. In UHV extended baking at high temperatures can even remove the amorphous oxide layer on the surface of single-crystalline silicon cantilevers. Another source of dissipation arises from additional metal layers for example added to increase the reflectivity of the cantilever backside, or to provide a magnetic moment to perform MFM. The dissipation arising from these coatings can be reduced by minimizing the required coating thickness, or by limiting the spatial extent of these layers. More details on the specific fabrication process are given in section 2.2.

### 1.1.5 Measuring the resonance frequency

The cantilever is forced to oscillate at a frequency $f$ typically chosen to match the frequency of one of its eigenmodes. The phase shift between the oscillatory deflection signal and the driving force of an harmonic oscillator is[15]

$$\varphi_{\text{n}}(f) = \arctan\left(\frac{f \cdot f_{\text{n}}/Q}{f_{\text{n}}^2 - f^2}\right), \tag{1.9}$$

as plotted in figure 1.3. The driving force is applied to the cantilever by a piezoelectric shaker and an electric excitation signal, generated by the local oscillator of the measurement electronics. For high-Q cantilevers, the shift of the resonance frequency induced by the tip-sample interaction typically becomes much larger than the width of the resonance peak. Hence, the electronics used to drive the cantilever oscillation must track the actual resonance of the cantilever. This is typically achieved by a Phase Locked Loop (PLL) system that shifts the excitation frequency to keep the measured phase at $-\pi/2$ apart from a phase offset produced by the electronic circuitry or arising from the mechanical coupling of the excitation piezo to the cantilever. The frequency shift of the PLL local oscillator then reflects the tip-sample interaction, while the deviation of the measured phase shift from $-\pi/2$ is the error signal. The latter is typically used to tune the P,I-parameters of the PLL to obtain an experimentally acceptable measurement bandwidth and noise. Since the different cantilever resonance modes do not overlap, different modes can be driven independently, using further PLL systems.

### 1.1.6 Tip sample interaction

The resonance frequencies of all cantilever oscillation modes (also other dynamic properties of the cantilever) change, if the tip is approached to the surface of a sample into the range of the relevant tip-sample interaction forces. The resonance frequency then becomes

$$f_{\mathrm{n,eff}}(z) = \frac{1}{2\pi}\sqrt{\frac{\langle k_{\mathrm{n,eff}}(z)\rangle}{m^*}} \tag{1.10}$$

where $m^*$ is the effective cantilever mass and $\langle k_{\mathrm{n,eff}}(z)\rangle$ is weighted average of the effective cantilever stiffness

$$\langle k_{\mathrm{n,eff}}(z)\rangle = k_{\mathrm{n}} - \langle k_{\mathrm{ts}}(z)\rangle\,. \tag{1.11}$$

The tip sample stiffness $k_{ts}(z) = \frac{\partial F_{\mathrm{z}}(z)}{\partial z}$ is the local z-derivative of the total tip-sample interaction force. The average tip sample stiffness $\langle k_{\mathrm{ts}}(z)\rangle$ at the average tip sample separation[2] $z$ is given by an integration over the oscillation path of the

---

[2] Note that in an experiment the tip sample distance $d_{\mathrm{ts}}$ at the lower turning point of the tip is determined. Hence, $z = d_{ts} + A_{\mathrm{n}}$.

tip $q(t) = A_\mathrm{n}\cos(2\pi f_\mathrm{n}\cdot t)$[21]:

$$\langle k_\mathrm{ts}(z)\rangle = \frac{2}{\pi A_\mathrm{n}^2}\int_{-A_\mathrm{n}}^{A_\mathrm{n}} F_\mathrm{ts}(z-q)\frac{q}{\sqrt{A_\mathrm{n}^2-q^2}}dq \tag{1.12}$$

$$= \frac{2}{\pi A_\mathrm{n}^2}\int_{-A_\mathrm{n}}^{A_\mathrm{n}} k_\mathrm{ts}(z-q)\sqrt{A_\mathrm{n}^2-q^2}dq. \tag{1.13}$$

For small amplitudes $A_\mathrm{n}$ the tip sample stiffness in the range of the tip oscillation path can be approximated as $k_\mathrm{ts}(z-q) \approx k_\mathrm{ts}(z)$. In this case the integral in equation 1.13 simplifies to a factor of $\frac{\pi}{2}A_\mathrm{n}^2$ and we get $\langle k_\mathrm{ts}(z)\rangle \approx k_\mathrm{ts}(z)$.

For most MFM experiments $\langle k_\mathrm{ts}\rangle \ll k_\mathrm{n}$ holds. Then, a Taylor expansion of the expression 1.10 gives:

$$f_\mathrm{n,eff} = f_\mathrm{n} + \Delta f_\mathrm{n} = f_\mathrm{n}\left(1 - \frac{\langle k_\mathrm{ts}\rangle}{2k_\mathrm{n}}\right), \tag{1.14}$$

where $\Delta f_\mathrm{n}$ is the shift of the resonance frequency for each mode:

$$\Delta f_\mathrm{n} = -f_\mathrm{n}\frac{\langle k_\mathrm{ts}\rangle}{2k_\mathrm{n}}. \tag{1.15}$$

The thermal energy, present in each oscillation mode, is the product of the Boltzmann constant $k_\mathrm{B}$ and measurement temperature $T$, leading to stochastic fluctuations of the cantilever oscillation. This thermal noise of the cantilever fundamentally limits the tip sample force derivative that is measurable within a measurement bandwidth $1/\tau_\mathrm{m}$, to a minimum of[12,10,22]:

$$\left.\frac{\partial}{\partial z}F_\mathrm{z}\right|_\mathrm{min} = \frac{1}{A_\mathrm{n}}\sqrt{\frac{4k_\mathrm{B}Tk_\mathrm{n}}{Q_\mathrm{n}2\pi f_\mathrm{n}\tau_\mathrm{m}}}. \tag{1.16}$$

The minimally measurable $\partial F_\mathrm{z}/\partial z$ scales inversely with the oscillation amplitude $A_\mathrm{n}$, which would make larger amplitudes advantageous. But as indicated above, the measured frequency shift signal decays for higher $A_\mathrm{n}$ because larger amplitudes average $k_{ts}$ over a larger z-range spanning from $z_\mathrm{min}$, the tip-sample distance at the lower turning point to $z_\mathrm{max} = z_\mathrm{min} + 2\cdot A_\mathrm{n}$. Consequently, the best signal-to-noise ratio is obtained with an oscillation amplitude that averages over the relevant interaction length of the measured force gradient[23].

Apart from the measurement temperature, the best obtainable sensitivity is given by the ratio $\frac{k_\mathrm{n}}{f_\mathrm{n} Q_\mathrm{n}}$. The ratio $\frac{k_\mathrm{n}}{f_\mathrm{n}}$ is proportional to $\frac{1}{\alpha_\mathrm{n}}$. Assuming a similar $Q_\mathrm{n}$ for all oscillation modes, which is often found experimentally in vacuum, higher modes hence provide a smaller sensitivity.

### 1.1.7 Tip sample interaction force

The force between tip and sample is a superposition of individual contributions at each lateral position of the tip as described in equation 1.17. In some cases the different force components can be disentangled for example by modulating one of them or changing its sign by means of an external field. Alternatively measurement conditions can be tuned to change the relative contributions to the measured frequency shift via differences in their interaction lengths.

$$F_\mathrm{ts} = F_\mathrm{cap} + F_\mathrm{vdW} + F_\mathrm{atom} + F_\mathrm{mag} \tag{1.17}$$

**The *capacitive* or *electric* force** $F_\mathrm{cap}$ can exhibit the longest interaction length in the range of several hundreds of nanometres up to a few micrometres. This force is given by the derivative of the energy stored in the capacitor that is formed by tip and sample being in close proximity[24]:

$$F_\mathrm{cap} = \frac{1}{2}\frac{\partial C}{\partial z}\left(U_\mathrm{Bias} - U_\mathrm{CPD}\right)^2 \tag{1.18}$$

The effective potential in equation 1.18 is composed of the sum of an externally applied bias potential $U_\mathrm{Bias}$ and the contact potential difference (CPD) between tip and sample materials $U_\mathrm{CPD}$. A material's contact potential (CP) is the difference between the fermi energy $E_\mathrm{f}$ and the vacuum level $E_\mathrm{vac}$ for an electron with charge $e$ with $U_\mathrm{CP} = \left(E_\mathrm{vac} - E_\mathrm{f}\right)/e$. The derivative of the capacitance is described by Hudlet *et al.*[25] for the common case of a sharp conical tip by an analytic approximation. For a tip with apex radius $R$, a small half opening angle $\vartheta_0$ and height $h$

they find:

$$\begin{aligned}\frac{\partial C}{\partial z} &= 2\pi\varepsilon_0 \left[\frac{R^2}{z(z+R)} + \left(\ln\tan(\frac{\vartheta_0}{2})\right)^{-4}\right. \\ &\quad \cdot \left.\left(\ln\frac{z+R}{h} - 1 + \frac{R}{(z+R)\sin\vartheta_0}\right)\right] .\end{aligned} \tag{1.19}$$

Shorter expressions are obtained by the asymptotic limits where $F_{\mathrm{cap}} \approx \pi\varepsilon_0 R/z$ for small distances $z \ll R$ and $F_{\mathrm{capacitive}} \propto \pi\varepsilon_0 \ln{(h/z)}$ for $z \gg R$. A more detailed discussion of the capacitive tip sample interaction for the case of time dependent bias is presented in chapter 4.

**The Van der Waals force** $F_{\mathrm{vdW}}$ between two bodies arises from fluctuating electrical dipoles in one of the bodies which induces a fluctuating dipole in the second body, attracting the dipole of the first body. This interaction also occurs between a SFM tip and a sample, where the respective interaction length is mainly related to the tip geometry. The van der Waals force acting on a conical tip is described by[26]

$$F_{\mathrm{vdW}}(z) = -\frac{H}{6}\left(\frac{R}{z^2} + \frac{(\tan\vartheta_0)^2}{z+R'} - \frac{R'}{z(z+R')}\right) \tag{1.20}$$

The parameter $R'$ describes the height of the spherical tip apex and is given by $R' = R(1-\sin\vartheta_0)$, whereas $H$ is an average Hamaker constant. Asymptotic limits are $F_{\mathrm{vdW}}(z) = -\frac{H}{6}\left(\frac{R}{z^2} - \frac{R}{z(z+R)}\right)$ for high aspect ratio tips with $\vartheta_0 \to 0$ and $F_{\mathrm{vdW}}(z) = -\frac{H}{6}\frac{R}{z^2}$ for short distances $z \ll R$. The latter expression is identical for the often used spherical model of the tip.

**The interatomic force** $F_{\mathrm{atom}}$ results from the overlap of the tip's and sample's electronic wave functions. A typical interaction length is in the order of 1 Å. For a two-body potential, the distance dependence can be described by the derivative of a Morse potential[26]:

$$F_{\mathrm{atom}} = \frac{2U_0}{\lambda}\left(\exp(-\frac{2(z-z_0)}{\lambda}) - \exp(-\frac{z-z_0}{\lambda})\right) . \tag{1.21}$$

The depth of the potential is defined by $U_0$ and is typically of the order of a few electron volts. The repulsive part of the force crosses zero at the offset distance $z_0$. The latter is typically required to correctly describe the height of an atomic-scale tip apex, or mini-tip, with respect to the conical or spherical tip with spherical end used to model the van der Waals interaction in equation 1.20.

**The magnetic tip sample force** $F_{\mathrm{mag}}$ arises from the interaction between the magnetic moment of a MFM tip and the stray field produced by the distribution of magnetic moments or currents in the sample. Under the assumption that the change of the micromagnetic state of the sample in the presence of the tip stray field can be neglected, the z-component of the total magnetic force acting on the tip is given by the integral of the derivative of the position dependent sample's stray field $\frac{\partial}{\partial z}\mathbf{H}_{\mathrm{sample}}$ and the local magnetic moment $\mathbf{M}_{\mathrm{tip}}$ distributed along the tip[27]:

$$F_{\mathrm{mag}}(\mathbf{r}, z) = \mu_0 \iint_{V'} \mathbf{M}_{\mathrm{tip}}(\mathbf{r}', z') \cdot \frac{\partial}{\partial z}\mathbf{H}_{\mathrm{sample}}(\mathbf{r}+\mathbf{r}', z+z')\, d\mathbf{r}'dz', \tag{1.22}$$

with the coordinate vector $\mathbf{r} = (x, y)$ and the vacuum permeability $\mu_0$. The integral is carried out over the tip's volume $V'$. The interaction length of the magnetic force depends on the magnetic structure of the sample and more specifically on the lateral size of the magnetic features present at the sample. Therefore, the interaction length can vary from below 10 nm to 100 nm and more. Details of the magnetic tip sample interaction and the relation to the measured frequency shift are discussed in section 1.3. From equation 1.33 it becomes apparent that a narrow spacial distribution of the tip magnetic moment is needed for high resolution measurements. Experimental details of the preparation of magnetically sensitive tips with the mentioned prerequisites are provided in section 2.2.

## 1.2 Distance feedback in MFM

In order to maintain a chosen distance between tip and sample while scanning, a feedback loop is required. The output of this feedback loop is used to control the position of the tip in $z$-direction and defines the tip trajectory. This output is typically referred to as topography signal although this signal is only a measure of the topography and can depart substantially from the true topography of the sample in some measurement modes. The term $z$-signal gives a more adequate description. In the absence of magnetic interactions and large variations of the contact potential difference, the derivative of the tip sample force and consequently the frequency shift serve as a good measure of the tip sample separation. In this case, both parameters show a monotonic dependence on the tip sample distance in the attractive part of the force curve, i.e., a higher attractive force derivative corresponds to a smaller tip sample separation and vice versa.

As long the tip remains in the attractive region of the tip-sample force, the measured frequency shift can be used as input for the feedback of the tip-sample distance, and the feedback output signal is a good measure of the sample topography. Note that generally feedback setpoints corresponding to a stronger tip-sample interaction force as, for example, more negative frequency shift setpoints, will reduce the tip-sample distance and result in topography images with sharper local features better representing the true topography. However, the risk of a tip crash is increased at such setpoints, because the margin for acceptable feedback errors is reduced at small tip-sample distances. Moreover, compared to the situation over flat surface areas, the van der Waals force over sharp topographical features is reduced such that the frequency shift may remain smaller than the frequency shift setpoint even at the smallest tip-sample distance, before repulsive forces occur. In this case, the tip collides with the sample surface. Large variations of the contact potential, that are not compensated by an additional Kelvin feedback loop generate strong local variations of the attractive electrostatic force. Consequently, a topography image obtained under such conditions would not be a good representation of the true sample topography. The same problem occurs in the presence of magnetic tip-sample interaction forces. A schematic trajectory resuling from a feedback with a constant frequency shift setpoint in the presence of magnetic forces is shown in figure 1.4. In this case, a repulsive magnetic force gradient stronger than the sum attractive force gradients from the van der Waals and electrostatic forces even leads to a collision of the tip with the surface of the sample.

Several methods have been developed to map magnetic forces at well controlled tip-sample separations which are described in the following sections 1.2.1 – 1.2.4.

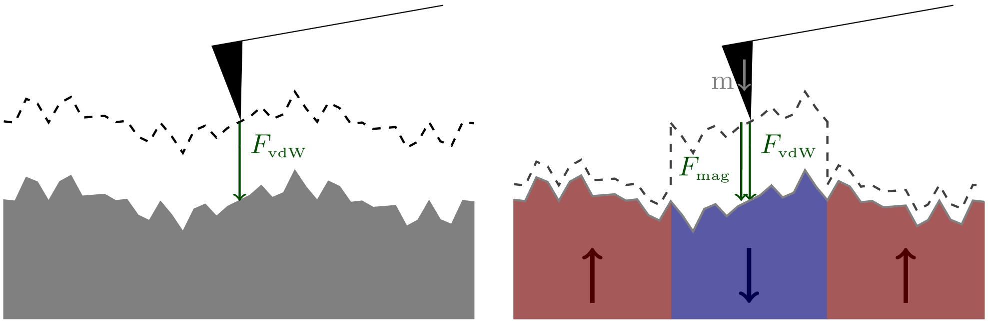

Figure 1.4: Distance feedback with a tip-sample interaction given by attractive van der Waals forces (*left*) and in the presense of additional magnetic forces (*right*). In the latter case the constant force contour does no longer reflect the topography of the sample. Moreover the feedback will fail at tip xy-positions where repulsive magnetic forces become larger than the attractive van der Waals forces.

### 1.2.1 Bias induced force offset

In the presence of magnetic forces the total interaction force gradient and thus the frequency shift can become non-monotonous or can change its sign for different xy-positions of the tip (*cf.* fig. 1.4). With a sufficiently strong bias potential, applied between tip and sample, the resulting electrostatic force dominates the magnetic forces. The frequency shift remains monotonous and keeps a constant sign for all xy-positions, and can then be used as input signal for the distance feedback. While scanning, the latter adjusts the tip-sample distance such that the frequency shift signal arising from the van der Waals and electrostatic forces compensates local frequency shift variations of the magnetic force. The measured z-position signal then contains both magnetic and topographical information.

### 1.2.2 Constant *average* force

A *slow* distance feedback can be used to keep the tip sample interaction and therefore their separation constant *on average*. The term *slow* refers to the characteristic reaction time of the feedback in comparison to the time between substantial variations of the tip-sample interaction and is therefore related to the scanning speed. With adequate feedback parameters, the feedback solely corrects a tilt of the sample relative to the slow axis of the scan-plane or a drift of the tip-sample distance. Local variations of the magnetic forces, but also local variations of the van der Waals force arising from topography-related variations of the tip-sample distance, generate a frequency shift signal, as the error signal of the feedback loop.

### 1.2.3 Lift mode

A commonly used method for MFM measurements is the lift mode technique: each scanline is recorded twice. In order to record an accurate profile of the topography in the first pass the tip sample separation has to be kept small such that the interaction is dominated by non magnetic tip sample interactions. Therefore, the topography is measured typically in an intermittent contact mode. Then the tip is retracted by a user-selected *lift-height* and the same line is scanned again along the previously recorded profile to measure the magnetic interaction. The latter is typically determined by the phase shift between the cantilever oscillation and the corresponding drive signal. However, the intermittent contact mode is difficult to apply in vacuum required for high lateral resolution MFM, because the energy loss per cycle occurring during the (intermittent) tip-sample contact is much larger than the intrinsic energy loss of a high quality factor cantilever. Thus, a stable oscillation of the cantilever is no longer possible.

### 1.2.4 Dual mode approaches

Two new single-passage methods have been developed, that allow to disentangle magnetic force and topography. Both operation modes have in common, that the the magnetic tip-sample interaction is reflected by the shift of the resonance frequency of the fundamental cantilever oscillation mode, while the second mode is used to control the tip-sample distance. Both operation modes are suitable for operation in vacuum. Details are given in chapters 3 and 4.

## 1.3 Quantitative MFM

An MFM measures stray fields emanating from the surface of a magnetic sample. Each spatial Fourier component of the stray field decays exponentially with the distance from the sample surface[27]. The relevant interaction volume of the tip with the sample stray field thus depends on the nature of the decay of the stray field and on the extent of the magnetic charge pattern at the surfaces of the magnetic coating of the tip. It is convenient to describe the measured frequency shift contrast that arises from the magnetic forces, in a two dimensional Fourier space where the Fourier transform of a general function $\mathbf{G}(\mathbf{r}, z)$ is

$$\hat{\mathbf{G}}(\mathbf{k}, z) = \mathcal{F}\left\{\mathbf{G}(\mathbf{r}, z)\right\} = \int \mathbf{G}(\mathbf{r}, z) e^{-i\mathbf{k}\cdot\mathbf{r}} d\mathbf{r} \tag{1.23}$$

with the coordinate vector in Fourier space $(\mathbf{k}, z) = (k_\mathrm{x}, k_\mathrm{y}, z)$.

### 1.3.1 Sample stray field

The Fourier transform of the stray field is

$$\hat{\mathbf{H}}(\mathbf{k}, z) = \int \mathbf{H}(\mathbf{r}, z) e^{-i\mathbf{k}\cdot\mathbf{r}} d\mathbf{r} \tag{1.24}$$

In the case of $\vec{\nabla} \times \mathbf{H} = \mu_0 \mathbf{j} = 0$ a scalar potential $\Phi_\mathrm{m}$ exists with $\mathbf{H} = -\vec{\nabla}\Phi_\mathrm{m}$ and $\hat{\mathbf{H}} = -\hat{\nabla}\hat{\Phi}_\mathrm{m}$. Thus the stray field is completely determined by the spectral distribution of its z-component[4,28] $\hat{H}_\mathrm{z}(\mathbf{k}, z)$ with:

$$\hat{\mathbf{H}}(\mathbf{k}, z) = -\frac{1}{k}\nabla_\mathrm{k} \cdot \hat{H}_\mathrm{z}(\mathbf{k}, z), \tag{1.25}$$

where the nabla operator is

$$\text{in real space:} \quad \nabla = \left(\frac{\partial}{\partial x}, \frac{\partial}{\partial y}, \frac{\partial}{\partial z}\right) \text{ and} \tag{1.26}$$

$$\text{in Fourier space:} \quad \hat{\nabla} = (ik_\mathrm{x}, ik_\mathrm{y}, -k) \quad \text{with:} \quad k = \sqrt{k_\mathrm{x}^2 + k_\mathrm{y}^2}. \tag{1.27}$$

For a film which is uniformly magnetized throughout the film thickness $d$, the magnetization pattern in Fourier space hence determines the stray field with

$$\hat{H}_{\mathrm{z}}(\mathbf{k},z) = -\frac{1}{2k}\left[e^{-kz}\left(1-e^{-kd}\right)\right]\begin{pmatrix} ik_{\mathrm{x}} \\ ik_{\mathrm{y}} \\ -k \end{pmatrix}\cdot \mathbf{M}(\mathbf{k}). \tag{1.28}$$

In equation 1.28 the factor $e^{-kz}$, often named as *distance loss*, describes the exponential decay of the magnetic stray field above the sample surface. The factor $(1-e^{-kd})$ is called *thickness loss* and accounts for the reduction of the stray field arising from the finite thickness $d$ of a thin film sample. The complete expression of equation 1.28 can also be interpreted as a superposition of the stray fields generated by opposite equivalent magnetic surface charges at the top and bottom surface of the magnetic film. These stray field contributions of opposite sign are superimposed with their respective distance loss, which is $e^{-kz}$ for the upper and $e^{-k(z+d)}$ for the lower magnetic charge distribution. Using equations 1.27 and 1.28 the z-derivative of the z-component of the stray field becomes

$$\frac{\partial \hat{H}_{\mathrm{z}}(\mathbf{k},z)}{\partial z} = -k\cdot\hat{H}_{\mathrm{z}}(\mathbf{k},z) = \frac{1}{2}\left[e^{-kz}\left(1-e^{-kd}\right)\right]\begin{pmatrix} ik_{\mathrm{x}} \\ ik_{\mathrm{y}} \\ -k \end{pmatrix}\cdot \mathbf{M}(\mathbf{k}). \tag{1.29}$$

### 1.3.2 Magnetic tip sample force

The force on the MFM tip placed in the stray field of a sample is[28]

$$\mathbf{F}_{\mathrm{mag}}(\mathbf{r},z) = \mu_0 \iint_{V'}\left(\vec{\nabla}\cdot\mathbf{M}_{\mathrm{tip}}(\mathbf{r}',z')\right)\mathbf{H}_{\mathrm{sample}}(\mathbf{r}+\mathbf{r}',z+z')\,d\mathbf{r}'dz'. \tag{1.30}$$

Equation 1.30 is a two-dimensional cross-correlation of $\left(\vec{\nabla}\cdot\mathbf{M}_{\mathrm{tip}}(\mathbf{r}',z')\right)^* = \vec{\nabla}\cdot\mathbf{M}_{\mathrm{tip}}(\mathbf{r}',z')$ and $\mathbf{H}_{\mathrm{sample}}(\mathbf{r},z+z')$. Thus we can make use of the cross-correlation theorem[3] and obtain the Fourier transform of equation 1.30 by a multiplication in

---

[3] The cross-correlation is defined by $\mathbf{G}\star\mathbf{J} = \int_{-\infty}^{\infty}\mathbf{G}^*(\tau)\mathbf{J}(t+\tau)d\tau$ where $^*$ dentotes the complex conjugate. The Fourier transform of the cross-correlation product is $\mathcal{F}\{\mathbf{G}\star\mathbf{J}\} = \hat{\mathbf{G}}^*\cdot\hat{\mathbf{J}}$.

Fourier space:

$$\begin{aligned}\hat{\mathbf{F}}(\mathbf{k},z) &= \mu_0 \int \left[ \begin{pmatrix} ik_\mathrm{x} \\ ik_\mathrm{y} \\ \frac{\partial}{\partial z} \end{pmatrix} \cdot \hat{\mathbf{M}}_\mathrm{tip}(\mathbf{k},z') \right]^* \cdot \hat{\mathbf{H}}_\mathrm{sample}(\mathbf{k},z+z')dz' \\ &= \mu_0 \int \begin{pmatrix} -ik_\mathrm{x} \\ -ik_\mathrm{y} \\ \frac{\partial}{\partial z} \end{pmatrix} \cdot \hat{\mathbf{M}}^*_\mathrm{tip}(\mathbf{k},z')\hat{\mathbf{H}}_\mathrm{sample}(\mathbf{k},z+z')dz'. \qquad (1.31)\end{aligned}$$

Since $\hat{\mathbf{H}}_\mathrm{sample}(\mathbf{k},z+z') = \hat{\mathbf{H}}_\mathrm{sample}(\mathbf{k},z)e^{-\mathbf{k}z'}$ we can write $\hat{\mathbf{H}}_\mathrm{sample}(\mathbf{k},z)$ as a factor outside the integral and obtain

$$\hat{\mathbf{F}}(\mathbf{k},z) = \mu_0 \underbrace{\int \begin{pmatrix} -ik_\mathrm{x} \\ -ik_\mathrm{y} \\ \frac{\partial}{\partial z} \end{pmatrix} \cdot \hat{\mathbf{M}}^*_\mathrm{tip}(\mathbf{k},z')e^{-\mathbf{k}z'}dz'}_{=:\,\sigma^*_\mathrm{tip}(\mathbf{k})} \cdot \hat{\mathbf{H}}_\mathrm{sample}(\mathbf{k},z). \qquad (1.32)$$

The quantity $\sigma^*_\mathrm{tip}(\mathbf{k})$ in equation 1.32 denotes the complex conjugate of $\sigma_\mathrm{tip}(\mathbf{k})$. The real space equivalent of the latter, $\sigma_\mathrm{tip}(\mathbf{r})$ is the two-dimensional density of an tip-equivalent magnetic surface charge located in a plane at the tip apex and thus completely describes the magnetic imaging properties of an MFM tip,

$$\hat{\mathbf{F}}(\mathbf{k},z) = -\mu_0\sigma^*_\mathrm{tip}(\mathbf{k})\frac{1}{k}\hat{\nabla}\hat{H}_\mathrm{z}(\mathbf{k},z). \qquad (1.33)$$

### 1.3.3 Measured frequency shift

The magnetic tip sample interaction described above leads to a shift of the resonance frequency of all oscillation modes. As described in section 1.1.6 the first mode typically provides the highest sensitivity. It is hence convenient to acquire the shift $\Delta f_1$ of the first mode resonance to obtain a high signal-to-noise ratio. The latter often imposes limits when deconvolving the stray field or the magnetization distribution of the sample from the measured MFM contrast. For this reason, all equations in this and following sections, are given for the first cantilever oscillation mode, although valid also for higher modes.

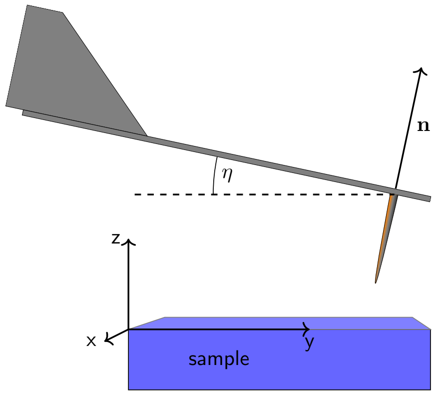

Figure 1.5: Schematic of the alginment of the cantilever with respect to the sample coordinates $y$ and $z$.

As developed in equation 1.15 the first mode frequency shift is

$$\Delta f_1 = -\frac{f_1}{2k_1} \langle k_{\mathrm{ts}} \rangle \,. \tag{1.34}$$

The $z_{\mathrm{n}}$-axis of the cantilever is tilted with respect to the sample coordinate system and parallel to the normal vector $\mathbf{n} = (0, \sin(\eta), \cos(\eta))$, where $\eta$ is the angle formed by the long cantilever axis $\xi$ and the $y$-axis of the sample coordinate system as illustrated in figure 1.5. The relevant force derivative for the measured frequency shift is the component parallel to the tip's oscillation path

$$\mathbf{q}(t) = \begin{pmatrix} 0 \\ q_{\mathrm{y}}(t) \\ q_{\mathrm{z}}(t) \end{pmatrix} = \mathbf{n}q(t) = \mathbf{n} \cdot A_1 \cos(2\pi f_1 t). \tag{1.35}$$

Thus the first mode frequency shift, caused by the magnetic interaction is

$$\Delta \hat{f}_{1,\mathrm{mag}} = -\frac{f_1}{2k_1} \left\langle \mathbf{n} \cdot \hat{\nabla} \hat{F}_{\mathrm{n}} \right\rangle , \tag{1.36}$$

with 1.33

$$\begin{aligned}\hat{F}_{\mathrm{n}}(\mathbf{k},z) &= \mathbf{n}\cdot\hat{\mathbf{F}}(\mathbf{k},z)\\ &= -\mu_0\sigma^*_{\mathrm{tip}}(\mathbf{k})\mathbf{n}\cdot\frac{1}{k}\hat{\nabla}\hat{H}_{\mathrm{z}}(\mathbf{k},z)\\ &= \mu_0\sigma^*_{\mathrm{tip}}(\mathbf{k})LCF(\mathbf{k},\eta)\hat{H}_{\mathrm{z}}(\mathbf{k},z).\end{aligned}\tag{1.37}$$

$LCF(\mathbf{k},\eta) := -\frac{1}{k}\mathbf{n}\cdot\hat{\nabla}$ defines the lever-canting-Function ($LCF$). The force gradient acting perpendicular to the cantilever plane and the $z$-derivative of the stray field is given by:

$$\begin{aligned}\mathbf{n}\cdot\hat{\nabla}\hat{F}_{\mathrm{n}}(\mathbf{k},z) &= \mathbf{n}\cdot\hat{\nabla}\mu_0\sigma^*_{\mathrm{tip}}(\mathbf{k})LCF(\mathbf{k},\eta)\hat{H}_{\mathrm{z}}(\mathbf{k},z)\\ &= -k\cdot LCF(\mathbf{k},\eta)\mu_0\sigma^*_{\mathrm{tip}}(\mathbf{k})LCF(\mathbf{k},\eta)\hat{H}_{\mathrm{z}}(\mathbf{k},z)\\ &= \mu_0\sigma^*_{\mathrm{tip}}(\mathbf{k})\cdot LCF^2(\mathbf{k},\eta)\frac{\partial\hat{H}_{\mathrm{z}}(\mathbf{k},z)}{\partial z}.\end{aligned}\tag{1.38}$$

For small oscillation amplitudes $A_1 \ll \frac{1}{k}$ the Fourier transform of the measured frequency shift can be calculated with equation 1.36:

$$\Delta\hat{f}^{A_1\to 0}_{1,\mathrm{mag}}(\mathbf{k},z) = -\frac{\mu_0 f_1}{2k_1}\sigma^*_{\mathrm{tip}}(\mathbf{k})\cdot LCF^2(\mathbf{k},\eta)\frac{\partial\hat{H}_{\mathrm{z}}(\mathbf{k},z)}{\partial z}.\tag{1.39}$$

For finite amplitudes $A_1$ the magnetic tip sample force varies with the sinusoidal oscillation of the cantilever $\mathbf{q}(t)$. The frequency shift is obtained by an integration over one oscillation cycle. In Fourier space the component $q_{\mathrm{y}}(t)$ leads to a phase shift of $e^{ik_{\mathrm{y}}q_{\mathrm{y}}(t)}$ whereas the $q_{\mathrm{z}}(t)$ component leads to a distance loss factor of $e^{kq_{\mathrm{z}}(t)}$. According to equations 1.13, 1.15 and 1.37, the frequency shift in Fourier space becomes

$$
\begin{aligned}
\Delta\hat{f}^{A_1>0}_{1,\mathrm{mag}} &= \frac{f_1}{2k_1}\frac{2}{\pi A_1^2} \\
&\quad \cdot \int_{-A_1}^{A_1} \mu_0 \sigma^*_{\mathrm{tip}}(\mathbf{k}) \cdot LCF(\mathbf{k},\eta)\hat{H}_{\mathrm{z}}(\mathbf{k},z) e^{ik_{\mathrm{y}}\sin(\eta)q} e^{k\cos(\eta)q} \frac{q}{\sqrt{A_1^2-q^2}} dq \\
&\quad \text{using: } iky\sin(\eta) + k\cos(\eta) = \hat{\nabla}\cdot\mathbf{n} \\
&= \frac{f_1}{2k_1}\frac{2}{\pi A_1^2} \int_{-A_1}^{A_1} \mu_0 \sigma^*_{\mathrm{tip}}(\mathbf{k}) \cdot LCF(\mathbf{k},\eta)\hat{H}_{\mathrm{z}}(\mathbf{k},z) e^{\hat{\nabla}\cdot\mathbf{n}q} \frac{q}{\sqrt{A_1^2-q^2}} dq \\
&= \frac{f_1}{2k_1}\frac{2}{A_1} \mu_0 \sigma^*_{\mathrm{tip}}(\mathbf{k}) \cdot LCF(\mathbf{k},\eta)\hat{H}_{\mathrm{z}}(\mathbf{k},z) \frac{1}{\pi A_1} \qquad (1.40) \\
&\quad \cdot \int_{-A_1}^{A_1} e^{\hat{\nabla}\cdot\mathbf{n}q} \frac{q}{\sqrt{A_1^2-q^2}} dq
\end{aligned}
$$

With the definition of the first order modified Bessel function of the first kind

$$
I_1(\tilde{z}) = \frac{1}{\pi}\int_0^{\pi} e^{\tilde{z}\cos\psi}\cos(\psi)d\psi \quad \text{with:} \quad \tilde{z} = A_1\mathbf{n}\cdot\hat{\nabla} \text{ and } \cos\psi = \frac{q}{A_1} \tag{1.41}
$$

follows

$$
\frac{1}{\pi A_1}\int_{-A_1}^{A_1} e^{\nabla\cdot\mathbf{n}q} \frac{q}{\sqrt{A_1^2-q^2}} dq = -I_1(\tilde{z}) \tag{1.42}
$$

and equation 1.41 becomes

$$
\begin{aligned}
\Delta\hat{f}^{A_1>0}_{1,\mathrm{mag}}(\mathbf{k},z) &= -\frac{\mu_0 f_1}{2k_1}\sigma^*_{\mathrm{tip}}(\mathbf{k}) \cdot \frac{2}{A_1} LCF(\mathbf{k},\eta)\hat{H}_{\mathrm{z}}(\mathbf{k},z) I_1(\tilde{z}) \\
&= TF(\mathbf{k}) \cdot \frac{2}{A_1} LCF(\mathbf{k},\eta)\hat{H}_{\mathrm{z}}(\mathbf{k},z) I_1(\tilde{z}), \qquad (1.43)
\end{aligned}
$$

where the prefactor in equations 1.39 and 1.43 is defined as

$$
TF(\mathbf{k}) := -\frac{\mu_0 f_1}{2k_1}\sigma^*_{\mathrm{tip}}(\mathbf{k}) \tag{1.44}
$$

This tip-transfer-function ($TF$) is determined by characteristic parameters of the cantilever and the conjugated Fourier transform of the tip equivalent magnetic surface charge distribution $\sigma^*_{\mathrm{tip}}(\mathbf{k})$. It describes the imaging properties of the tip in Fourier space.

Expressing the frequency shift in equation 1.43 as a function of the z-derivative of the stray field yields

$$\Delta \hat{f}^{A_1>0}_{1,\mathrm{mag}}(\mathbf{k},z) = TF(\mathbf{k})\cdot \underbrace{\frac{2}{A_1} LCF(\mathbf{k},\eta) I_1(\tilde{z})\frac{1}{-k}\frac{\partial \hat{H}_{\mathrm{z}}(\mathbf{k},z)}{\partial z}}_{=:\ \left.\frac{d\hat{H}^{\mathrm{A}_1}_{\mathrm{n}}(\mathbf{k},z)}{dn}\right|_{\mathrm{eff}}} \quad . \tag{1.45}$$

The expression

$$\left.\frac{d\hat{H}^{\mathrm{A}_1}_{\mathrm{n}}(\mathbf{k},z)}{dn}\right|_{\mathrm{eff}} := \frac{2}{A_1} LCF(\mathbf{k},\eta) I_1(\tilde{z})\frac{1}{-k}\frac{\partial \hat{H}_{\mathrm{z}}(\mathbf{k},z)}{\partial z} \tag{1.46}$$

denotes an effective stray field derivate along the n-axis, and can be interpreted as a stray field derivative that generates the same frequency shift for a cantilever oscillating with an infinitesimally small amplitude. The following table summarizes the results of this section.

| **Summary** | | | |
|---|---|---|---|
| small Amplitude limit: | $\Delta \hat{f}^{A_1\to 0}_{1,\mathrm{mag}}(\mathbf{k},z)$ | $=$ | $TF(\mathbf{k})\cdot LCF^2(\mathbf{k},\eta)\frac{\partial \hat{H}_{\mathrm{z}}(\mathbf{k},z)}{\partial z}$ |
| finite Amplitudes: | $\Delta \hat{f}^{A_1>0}_{1,\mathrm{mag}}(\mathbf{k},z)$ | $=$ | $TF(\mathbf{k})\cdot \left.\frac{d\hat{H}^{\mathrm{A}_1}_{\mathrm{n}}(\mathbf{k},z)}{dn}\right\|_{\mathrm{eff}}$ |
| Tip transfer function: | $TF(\mathbf{k})$ | $:=$ | $-\frac{\mu_0 f_1}{2k_1}\sigma^*_{\mathrm{tip}}(\mathbf{k})$ |
| effective stray field derivative: | $\left.\frac{d\hat{H}^{\mathrm{A}_1}_{\mathrm{n}}(\mathbf{k},z)}{dn}\right\|_{\mathrm{eff}}$ | $:=$ | $\frac{2}{A_1} LCF(\mathbf{k},\eta) I_1(\tilde{z})\frac{1}{-k}\frac{\partial \hat{H}_{\mathrm{z}}(\mathbf{k},z)}{\partial z}$ |

### 1.3.4 Determination of the *tip-transfer-function* $TF$

The $TF$ is derived as the deconvolution of a known or estimated stray field distribution $\mathbf{H}_{cal}(\mathbf{r},z_0)$ and the measured frequency shift data $\Delta f_1(\mathbf{r},z_0)$ recorded at a fixed average distance $z_0$ above the calibration sample. An example of such a measurement of $\Delta f_1$ at a tip sample distance of $z_0 = d_{\mathrm{ts}} + A_1 = 17\,\mathrm{nm}$ with $d_{\mathrm{ts}} = 12\,\mathrm{nm}$ and $A_1 = 5\,\mathrm{nm}$ is depicted in figure 1.6(a). Note that the stray field gradient scales exponentially with tip sample distance and thus an accurate measurement and control of the tip sample distance $z_0$ is crucial for a correct calibration. The influence of the measurement distance $z$, oscillation amplitude $A_1$, canted tip oscillation path along to $\mathbf{n}$ and the film thickness $d$ is known and included in the effective stray field gradient $\frac{d\hat{H}_{\mathrm{n}}^{\mathrm{A}_1}(\mathbf{k},z)}{dn}\Big|_{\mathrm{eff}}$. Thus only $TF(\mathbf{k})$ needs to be determined from calibration measurements.

In a sample with sufficiently strong perpendicular magnetic anisotropy, the magnetization points up or down in the domains and rotates between the two directions in the narrow domain walls. Hence, the white and black domains in figure 1.6(a) can be identified as up and down domains provided the tip had a down magnetization. A magnetization pattern could thus be obtained from discriminating the measured frequency shift pattern arising from the domains in figure 1.6(a). This however leeds to artifacts, because the stray field and hence the measured $\Delta f_1$ decay in the center of larger domains. Moreover the domain walls apear asymmetric along the y-direction because of the canted oscillation of the cantilever. Both problems can at least be partially overcome, when a frequency shift pattern $\Delta f_{1,\mathrm{dec}}$ is calculated from the measured one using:

$$\Delta\hat{f}_{1,\mathrm{dec}}^{A_1=0}(\mathbf{k},z_{\mathrm{sim}}) = \Delta\hat{f}_1 \cdot \left(LCF(\mathbf{k})\frac{1}{A_1}I_1(\tilde{z})\right)^{-1} \cdot \exp^{-k(z_{\mathrm{sim}}-z_0)}. \tag{1.47}$$

The data resulting from the application of equation 1.47 with $z_{\mathrm{sim}}$=5 nm is shown in figure 1.6(b). An estimation of the magnetization pattern can then be obtained by applying a threshold to the data shown in figure 1.6(b) and including the correct domain wall profile. The latter can be calculated from the perpendicular magnetic anisotropy and the exchange stiffness. The resulting estimated magnetization pattern in figure 1.6(c). From this magnetization pattern the stray field derivative (figure 1.6(d)) and effective derivative (figure 1.6(e)) at z = 17 nm are calculated with equations 1.29 and 1.46, respectively.

According to equation 1.43, the tip-transfer function $TF(\mathbf{k})$ relates the effective stray field derivative to the the measured frequency shift as

$$\Delta\hat{f}_{1,\mathrm{meas}}^{\mathrm{subtr}}(\mathbf{k}) = TF(\mathbf{k})\frac{d\hat{H}_{\mathrm{n}}^{\mathrm{A}_1}(\mathbf{k},z)}{dn}\Big|_{\mathrm{eff}}. \tag{1.48}$$

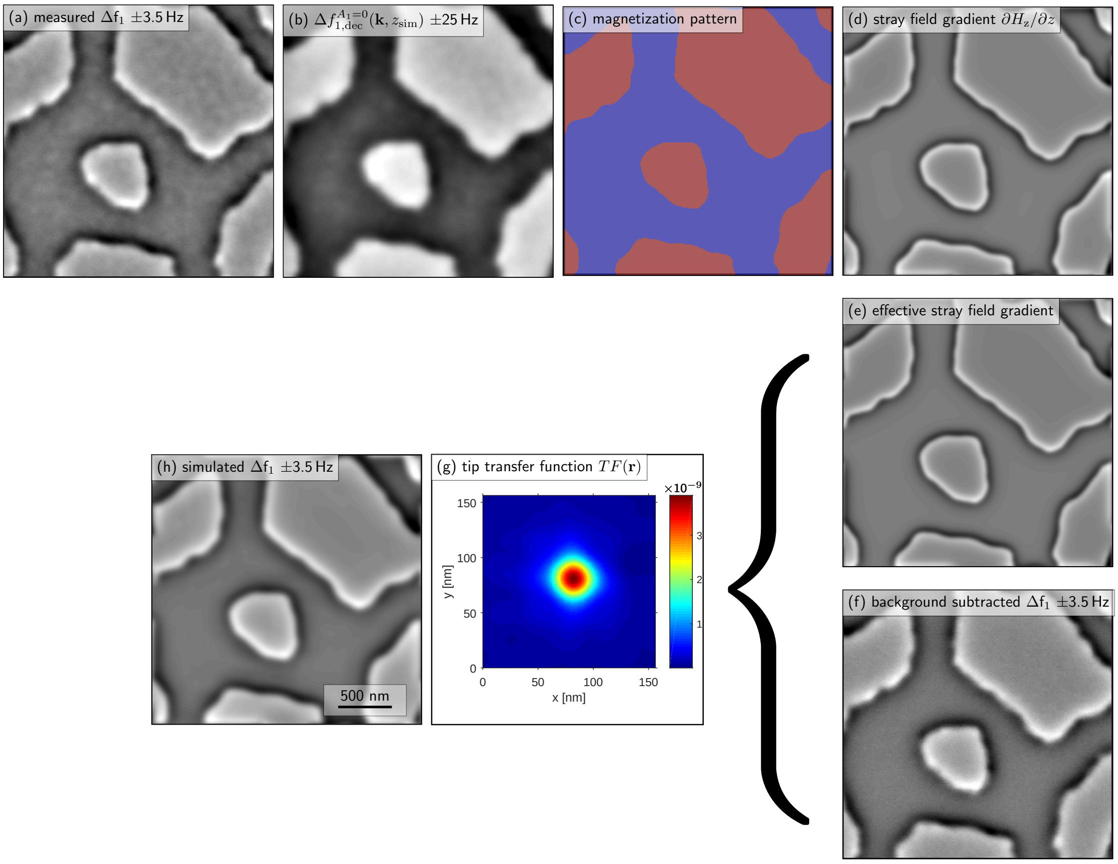

Figure 1.6: Illustration of the tip calibration procedure. All images show the real space distribution of the specified quantities. Panel (a) shows the measured frequency shift data with a contrast scale (white to black) of ±3.5 Hz. The data was measured with a cantilever with a stiffness $k_1$ of 0.85 N/m, a resonance frequency $f_1$ of 50280 Hz, oscillating with an amplitude $A_1$ of 5 nm, and at a tip-sample distance $d_{\mathrm{ts}}$=12 nm. (b): Frequency shift obtained using equation 1.47, displayed at a contrast scale of ±25 Hz. Note that the asymmetry of the domain walls along the y-direction and the decay of the frequency shift in the center of larger domains is removed. (c): estimated magnetization pattern obtained by discrimination of the simulated frequency shift data depicted in (b). The red and blue domains correspond to positive and negative saturation magnetization $\pm M_{\mathrm{sat}}$ of the sample. $M_{\mathrm{sat}}$ is determined from vibrating sample magnetometry. (e): Simulated effective stray field gradient along the canted tip oscillation path $\mathbf{n}$. (f): The background frequency shift variation is subtracted from the measured frequency shift data (a). (g): Transfer function represented in real space in units of Hz·m/T. It represents an equivalent magnetic charge distribution in a plane located at the tip apex. (h): Simulated frequency shift data derived from the stray field gradient in (e) and the transfer function in (g).

From equation 1.48 $TF(\mathbf{k})$ can be formally obtained by division of the frequency shift by the effective stray field derivative. However, in practice, the effective stray field can be small, particularly for small spatial wavelengths. This amplifies the noise at smaller spatial wavelengths, if a simple division is performed. Equation 1.48 is hence an ill-posed problem which requires a regularization which is discussed further in chapter 5. In the present example the measured raw data displayed in figure 1.6(a) shows a pattern of micron sized up and down domains, and a weaker granular frequency shift variation (background). Data acquired in saturation proves that this granular background is not noise, but is either caused by a local variation of the stray field or van der Waal's force. The latter arises from local sample roughness induced variations of the tip-sample distance, when the tip is scanned parallel to the sample surface at a constant average tip-sample distance (see also chapter 4). The origin of this background contrast is discussed in detail in chapter 5. It will be further shown how this background is removed from the measured frequency shift data before the tip-transfer function can be determined. Data obtained after removing this background from the measured frequency shift is depicted in figure 1.6(f). From this and the calculated effective stray field derivative, the tip-transfer function illustrated in figure 1.6(g) can be calculated.

The fidelity of the tip transfer function can be tested by comparing the background subtracted data with simulated MFM data in figure 1.6(h).

Note that a transfer function that is obtained from a single MFM image and from the effective stray field derivative obtained from a magnetization image estimated from the MFM image contains errors arising from the difference between the real and estimated magnetization pattern and from spatial variations of the sample thickness and tip sample distance. In order to obtain an improved estimate of the tip-transfer function the described process must be repeated for a large number of measurements and all obtained transfer functions must be averaged.

# 2 Instrumentation

## 2.1 Experimental setup: hr-MFM

An *hr-MFM* instrument supplied by the company $NanoScan$ is used for the experiments in chapter 3 and 4. Several modifications have been made to obtain a noise floor and drift rates sufficiently small to perform the measurements reported in this thesis.

The scanning force microscope setup of the *hr-MFM* is located in a vacuum chamber in order to obtain high vacuum conditions with base pressure of approximately $1 \cdot 10^{-6}$ mbar. The tip can be positioned with sub-micrometer precision at any location of a disk-shaped sample holder with a diameter of 95 mm. A perpendicular field option enables measurements in applied B-fields up to ≈0.6 T perpendicular to the sample surface. This option is implemented by a permanent magnet which can be approached to the backside of the sample. The instrument features a linearized flexure-stage scanner with an $x \times y \times z$ range of $12\,\mu\mathrm{m} \times 12\mu\mathrm{m} \times 2\mu\mathrm{m}$. Because of the 16 bit digital-to-analog converters (DACs), the bit-resolution is limited to 0.18 nm laterally and 0.03 nm in the z-direction, which is sufficient for all MFM measurements presented here. A *National Instruments PXI Embedded-Controler* with one or optionally two FPGA based input/output cards with each eight analog inputs and outputs for fast data acquisition is used as a control system. The PLL system of Nanoscan has been replaced by a *Zurich Instruments* lock in amplifier *HF2PLL*.

### Cantilever deflection noise

The deflection of the cantilever is measured by the means of a beam deflection sensor with a detection bandwidth of roughly 1 MHz. A spectrum of the spectral noise density is depicted in the plots of figure 2.1.

The left-hand panel shows the spectrum of the as-delivered instrument. Several noise peaks are apparent that have a size comparable to the thermal noise peaks of the cantilever. Depending on the exact location of the cantilever resonance, this prevents MFM measurements with high sensitivity. After re-configuring the grounding of all relevant instrument components, i.e. implementing a star-like grounding concept avoiding ground loops, peaks at 50Hz, multiples thereof and in the high kHz range are removed and the noise background is lowered. This is visible in the right-hand panel, where the thermal noise peaks of the first three resonance modes dominate the spectrum. A low white noise floor of approximately $100\,\mathrm{fm}/\sqrt{\mathrm{Hz}}$ can be reached up to 200 kHz, which is above the frequency range of first mode resonance frequencies of typical cantilevers used for magnetic force microscopy. Note that the sensitivity of typically 90 nm/V is determined for the first mode of a cantilever with $225\,\mu$m length. For higher modes or shorter cantilevers a given deflection of the tip at the cantilever end leads to a larger angular deflection. Consequently a higher sensitivity for the tip deflection is obtained (see arrows and second scale in figure 2.1). The virtually rising noise floor towards higher frequencies is thus more than compensated by the higher modes increased sensitivities given in table 1.1. A profound overview on the topic of electronic noise and practical advise is provided in references[29] and[30].

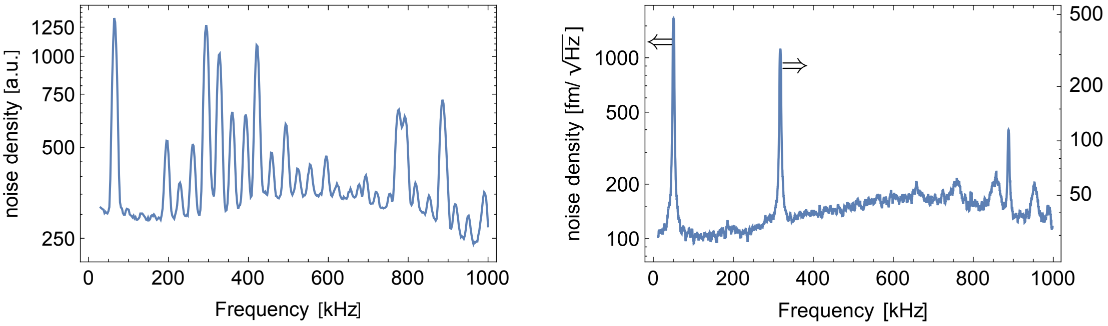

Figure 2.1: Thermal noise spectrum from 10kHz to 1MHz of a 50 kHz cantilever as measured with the hrMFM before (left-hand) and after (right-hand) changing the grounding concept. A noise floor of $100\mathrm{fm}/\sqrt{\mathrm{Hz}}$ is obtained. The thermally excited oscillations of the first three resonance modes of a cantilever with $k_1 \approx 0.7\,\mathrm{N/m}$ in air are visible in the right-hand plot.

### Replacement of the laser diode of the beam deflection system

The beam-deflection system of the hrMFM contained a laser diode. Because of the long coherence length of the laser diode light, reflections from the sample can interfere with the light reflected from the cantilever backside, generating tip-sample distance dependent intensity modulations. After replacing the laser diode with a super luminescent light emitting diode (SLED) *EXS8310-8411* supplied by *EXALOS*, which emits incohenrent light, this problem is solved. Further, a temperature stabilized mount for the light source is implemented. Figure 2.2 depicts the light intensity (left-hand) and the measured 2nd mode resonance frequency of the cantilever (right-hand) as a function of light source temperature. Both quantities show an, approximately linear dependence on the temperature of the SLED in a 20-25 °C temperature range. The second mode resonance frequency changes with about 0.8 Hz/°C. Similar results have been published recently by Augilar Sandoval et al.[31]. If the tip-sample distance is control relies on the measured second mode resonance frequency (see chapter 3), variations of room temperature and thus the light source of less than one Kelvin lead to an unacceptably large change of the tip-sample distance (as observed for the as-delivered hrMFM). The original current control electronics of the hrMFM is therefore replaced by the combination of a current controller *LDC201CU*, a temperature controller *TED200C* and temperature controlled mount *LDM*21 all manufactured by *Thorlabs*.

## 2.2 Tip preparation

In order to achieve high resolution as well as high sensitivity in MFM measurements a sophisticated preparation of the magnetic tip is required. For all results presented in this thesis, we used uncoated single cristalline cantilevers provided by *Team Nanotec* with a nominal stiffness of 0.7 N/m and an *Improved Super Cone (ISC)* tip.

The tip is made sensitive to magnetic fields by sputter-coating a typically 4–10 nm thick cobalt (Co) on a 2 nm titanium (Ti) seed layer on the side of the tip which is facing towards the cantilever support chip. The Co layer is protected against oxidation by 2 nm of Ti. The cantilever is aligned at an angle of about

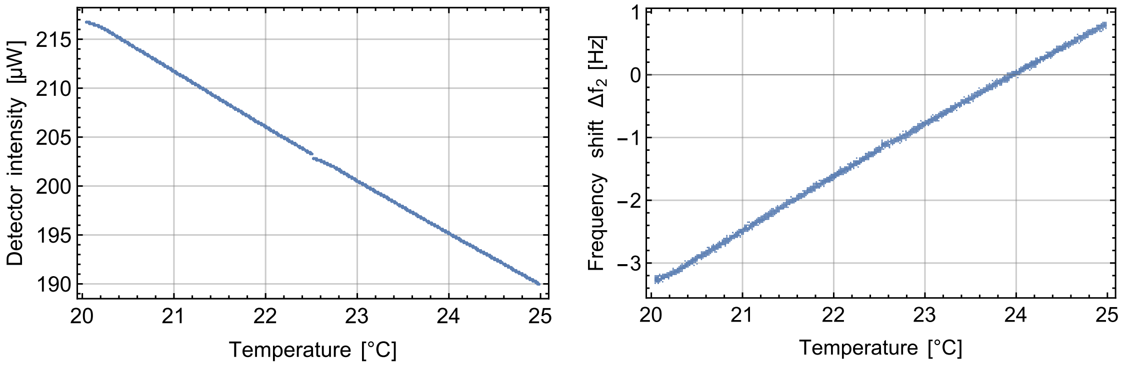

Figure 2.2: The temperature of the SLED has a strong influence on the resonance frequency of higher cantilever modes.
*Left:* Detector Intensity as a function of the SLED's temperature.
*Right:* Shift of the second mode resonance frequency as a function of the SLED's temperature.

30° towards the sputtering direction. With this alignment a magnetic coating of sufficient thickness is obtained at the side of the tip and on the top of the tip apex, but the layer thickness on the cantilever remains thin. We further find that the cantilever itself has a sufficient reflectivity such that a reflective coating of the cantilever backside is not required. With this procedure, a high quality factor of the cantilever of typically $Q_1 = 40'000$ is achieved in vacuum. The coating is performed in an *ATC Orion* UHV sputtering system supplied by *AJA*.

The Co layer thickness is adjusted to obtain a sufficient sensitivity for a particular MFM experiment and to avoid an influence of the tip field on the sample magnetization. Depending on the sample 10 nm lateral resolution for magnetic features can be obtained. All thickness values given above refer to normal incidence and flat substrates. For comparison we use probes with the company's *ML1* coating. Without reflective coating they exhibit similar quality factors in than the ones coated in our AJA system (35'000 – 40'000). On magnetically hard samples a lateral magnetic resolution of 10 nm can be obtained. However the magnetic stray field of *Team Nanotec's hr-MFM* tips is too strong for the measurement of magnetic samples with low coercivity.

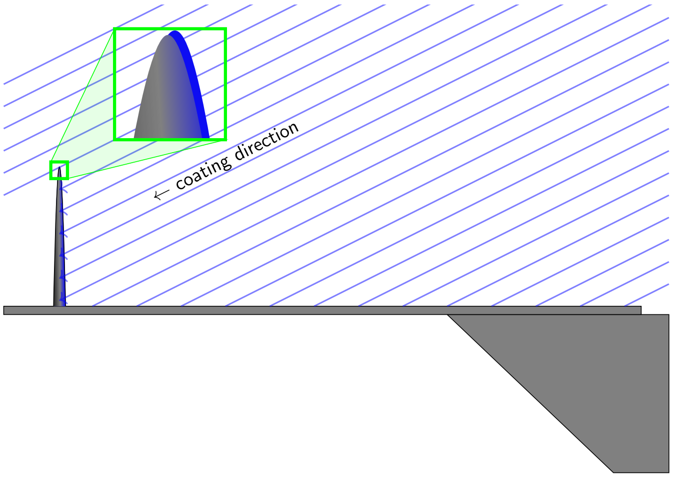

Figure 2.3: Schematic of the magnetic coating process of the MFM tips; the cantilever is aligned at an angle of 30° towards the sputter target and thus only the side of the tip facing the support chip is coated.

## 2.3 Sample demagnetization

In order to obtain a domain state, samples are often measured in a demagnetized state. For this demagnetization of the samples we apply an oscillatory B-field with an amplitude decaying from initially $0.8\,\mathrm{T}$ to $0\,\mathrm{T}$. As illustrated in figure 2.4 the amplitude of the oscillation linearly decreases to zero within the time period of 1000 oscillation cycles.

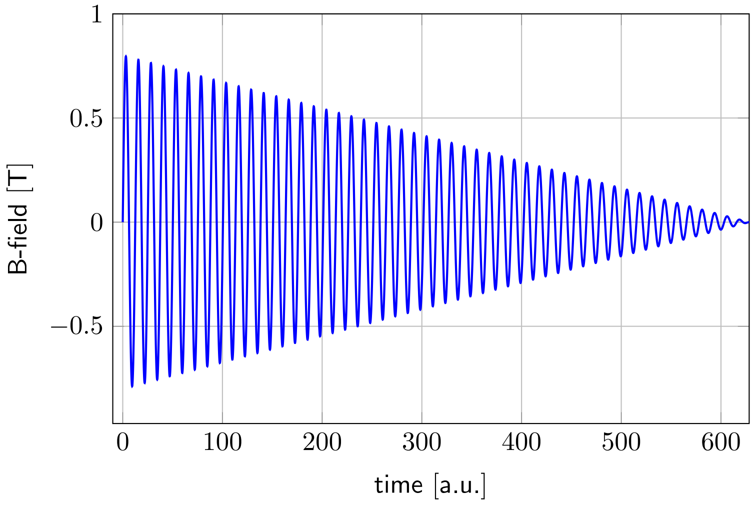

Figure 2.4: The plot illustrates the time dependent B-field during demagnetization process of the samples. The maximum B-field is 0.8 T and the envelope of the sinusoidal oscillation decreases linearly to zero in 1000 cycles. For clarity only 50 cycles are plotted.

# 3 Non-contact bimodal Magnetic Force Microscopy[1]

## Preface

This chapter is composed from the text and figures of the reference[1], published 2014 in Applied Physics Letters 104 by AIP Publishing. Authors of the paper are J. Schwenk, M. A. Marioni, S. Romer, N. R. Joshi and H. J. Hug.

## 3.1 Introduction

Most magnetic force microscopes (MFM) use a two-passage method, where each line is scanned in a intermittent contact mode to measure the topography of the sample and subsequently with the tip lifted off the surface to record the magnetic signal[6,7]. This measurement mode is robust and well applicable to samples with arbitrary topography, e.g. rough samples or patterned media. However, the intermittent contact mode is difficult to apply in vacuum required for high lateral resolution MFM as outlined in detail below. Recently, Li et al.[32] reported a single passage method that makes use of bimodal cantilever excitation introduced by Rodriguez and Garcia[33]. The cantilever was driven on its first mode at an amplitude of several tens of nanometers and simultaneously on its second mode at a much smaller amplitude. The first mode amplitude was kept constant by the feedback that controls the tip-sample distance, i.e. reflects the measured topography of the sample. The second mode amplitude and phase were used to record the magnetic signal. Note that for a scan of this kind to be carried out in a reasonable amount of time the oscillation amplitude must stabilize quickly at every point. Hence very high cantilever quality factors are impractical. Therefore work was performed in air, resulting in low quality factors of the cantilever, i.e. 120 and 500 on the first and second mode, respectively. Another interesting experimental approach suited for low quality factor cantilevers is based on narrow-band intermodulation atomic force microscopy[34].

In our work we developed a non-contact bimodal magnetic force microscopy technique which can take advantage of the higher sensitivities provided by high quality factor cantilevers. It is optimally suited for operation in vacuum or UHV for highest sensitivity and thus best spatial resolution.

Each spatial Fourier component of the magnetic stray fields decays exponentially with increasing distance $z$ from the surface of a magnetic sample, $H_z(\mathbf{k}, z) = H_z(\mathbf{k}, 0) \cdot \exp(-kz)$, where $H_z(\mathbf{k}, 0)$ is the stray field at the surface of the sample, and $\mathbf{k} = (k_x, k_y)$ with $k = 2\pi/\lambda$, where $\lambda$ is the spatial wavelength[4]. Given a sufficiently sharp tip with an appropiately thin magnetic coating, high resolution imaging thus requires small tip-sample distances, correspondingly small oscillation amplitudes, and a high sensitivity for small forces or force derivatives.

## 3.2 Experimental details

We used a cantilever from *Team Nanotec GmbH* with an ISC high aspect ratio tip coated with about 8 nm Co. Such a thin magnetic coating leads to a correspondingly small magnetic moment. This is advantageous if soft magnetic samples are measured, but requires an excellent measurement sensitivity to detect the small magnetic signals arising from smaller spatial wavelengths of the stray field. The thermodynamic limit for the minimally measurable force derivative on the n-th cantilever oscillation mode is given by[22]

$$\left.\frac{\partial}{\partial z} F_z\right|_{min} [\mathrm{N}/\sqrt{\mathrm{Hz}}] = \frac{1}{A_n}\sqrt{\frac{4k_B T k_n}{Q_n \omega_n}}. \tag{3.1}$$

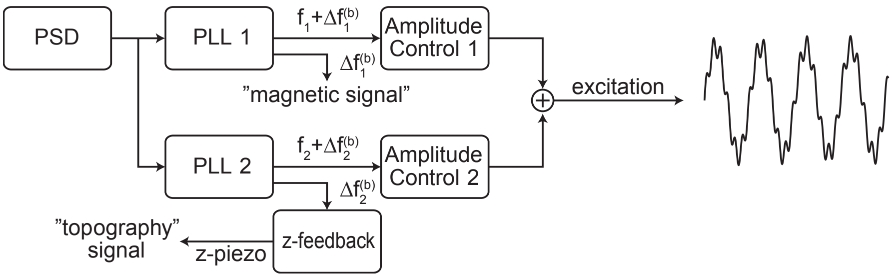

Figure 3.1: Schematic of the dual-PLL system required for bimodal oscillation of high quality factor cantilevers. PLL 1 tracks the first flexural oscillation mode resonance frequency $f_1$ of the cantilever. The output amplitude is adjusted by a PI feedback (Amplitude Control 1) to keep the (first mode) oscillation amplitude constant, e.g. at 12 nm. The shift of the first mode resonance frequency, $\Delta f_1^{(b)}$ predominantly reflects the longer-ranged magnetic part of the tip-sample interaction. PLL 2 tracks the second flexural oscillation mode resonance frequency $f_2$ of the cantilever. The PI feedback Amplitude Control 2 keeps the second mode amplitude constant, e.g. at 0.27 nm. At such a small amplitude the second mode resonance frequency shift $\Delta f_2^{(b)}$ predominantly arises from the van der Waals part of the tip-sample interaction, which depends on the tip-sample distance but not on the micromagnetic details of the sample. $\Delta f_2^{(b)}$ and thus the local tip-sample distance is kept constant by the z-feedback. Its output then reflects the topography of the sample.

The force constant $k_n$ and the resonance frequency $\omega_n$ of the n-th mode relate to those of the first mode as

$$k_n = k_1 \cdot \left[\frac{\alpha_n}{\alpha_1}\right]^4 \quad \text{and} \quad \omega_n = \omega_1 \cdot \left[\frac{\alpha_n}{\alpha_1}\right]^2 \tag{3.2}$$

with $\alpha_i = \{1.8750, 4.6941, 7.8548, 10.9955, ...\}^{22}$.

According to eqs. 3.1 and 3.2 the sensitivity of a higher mode $n$ is lower than for the first mode by $\alpha_n/\alpha_1 \cdot \sqrt{Q_1/Q_n}$. The first mode is hence better suited for the measurement of the small magnetic forces. In order to obtain higher quality factors our MFM (a modified *Nanoscan hrMFM*) with two phase-locked loops (Fig. 3.1) is operated under vacuum conditions. The first mode force constant of the cantilever, $k_1 = 0.996\,\mathrm{N/m}$ was calculated from the measured first mode resonance frequency, $f_1 = 53'059.9\,\mathrm{Hz}$, the length $l = 225\,\mu\mathrm{m}$ and the width $w = 35\,\mu\mathrm{m}$. The second mode force constant $k_2 = 39.1\,\mathrm{N/m}$ was obtained from Eq. 3.2, and the second mode resonance frequency was measured, $f_2 = 327'850\,\mathrm{Hz}$. In vacuum, the first and second mode quality factors were $Q_1 = 40'268$ and $Q_2 = 17'205$, respectively. Such high quality factors do not permit the excitation of the cantilever at a user-selected fixed frequency, but require PLLs to drive the first and second mode on their respective resonance frequencies (Fig. 3.1). The amplitude response of the deflection detector of our MFM was calibrated by a thermal noise analysis[35]. The z-feedback adjusts the tip-sample distance to keep the second mode frequency shift constant.

## 3.3 Measurement principle

As outlined by Giessibl et al.[36] the frequency shift of a cantilever of stiffness $k$ oscillating in a *single mode* with an amplitude $A$ in a force field derivative $\frac{\partial}{\partial z}F_z(z) = k_{ts}(z)$ becomes

$$\Delta f(z_{ltp}) = \frac{f_0}{2k}\frac{2}{\pi A^2}\int_{-A}^{A} k_{ts}(z_{ltp} + A - q) \cdot \sqrt{A^2 - q^2}dq, \qquad (3.3)$$

where $z_{ltp}$ is the tip-sample distance at the lower turning point, $f_0$ is the resonance frequency of the cantilever far away from the surface, and $k_{ts}$ is the local stiffness of the tip-sample interaction. In the limit of small amplitudes the frequency shift becomes proportional to the stiffness of the tip-sample interaction force,

$$\Delta f(z) = -\frac{f_0}{2k} \cdot k_{ts}(z). \qquad (3.4)$$

This approximation is valid as long as $k_{ts}$ is approximately constant over the z-range spanned by the oscillating tip. At small tip-sample distances the z-derivative of the van der Waals force is usually much stronger than that of the magnetic force. In that case, a frequency shift measured with a cantilever oscillating with a small amplitude at a small tip-sample distance is dominated by the non-magnetic van der Waals force. At considerably larger amplitudes the small amplitude approximation no longer holds and Eq. 3.3 must be used to calculate the frequency shift. In essence, Eq. 3.3 averages $k_{ts}(z)$ over time. The weaker but longer-ranged magnetic stiffness curve dominates that of the stronger but shorter-ranged van der Waals stiffness curve. The long range magnetic force then becomes the dominant contribution to the measured frequency shift. Note that these observations hold independently of the cantilever oscillation mode. So, for the same oscillation amplitude, the frequency shifts of the n-th mode simply scale to those of the first mode as $\Delta f_n = \Delta f_1 \cdot \alpha_1^2/\alpha_n^2$.

In bimodal operation conditions with large $A_1/A_2$-ratios, the frequency shift versus distance curve $\Delta f_2^{(b)}(z_{ltp})$ has a distance dependence closely resembling what would be measured without the first mode oscillation amplitude $(\Delta f_2(z_{ltp}))$. However, the frequency shift values are smaller at all distances[37]. The second mode bimodal frequency shift $\Delta f_2^{(b)}(z_{ltp})$ is thus also dominated by the short-range van der Waals force. Consequently, if $\Delta f_2^{(b)}$ is kept constant by the (fast) z-feedback, the output of the latter corresponds to the topography of the sample. The bimodal frequency shift of the first mode, $\Delta f_1^{(b)}$, is not affected by the presence of the small-amplitude second mode oscillation, because the cantilever oscillation modes are not harmonic[32,37]. Hence $\Delta f_1^{(b)}$ reflects the long range magnetic force.

## 3.4 Measurements

Figure 3.2 summarizes MFM results obtained with different ratios of the first to second mode amplitudes in bimodal operation on a multilayer structure of $\mathrm{Pt_{5nm}/[Co_{0.4nm}/Pt_{0.7nm}]_{\times 15}Pt_{1nm}/SiO_2^{ox}/Si}$ with perpendicular magnetic anisotropy. The second mode frequency shift $\Delta f_2^{(b)}$ was kept constant at $-6.8\,\mathrm{Hz}$ for all data shown here. An excellent separation of the magnetic and topographic signal is obtained for an $A_1/A_2$-ratio of 44 (Fig. 3.2(a), (b) and (c) ). The first bimodal frequency shift $\Delta f_1^{(b)}$ data (Fig. 3.2(a) shows the up/down domain structure typical for such a sample, while the output of the z-feedback (Fig. 3.2(b) operating on the second bimodal frequency shift $\Delta f_2^{(b)}$ reflects the topography of the sample. The instrumental drift of the sample's z-position becomes apparent as the image scanned from the bottom to the top and from the left to the right appears darker at the left and brighter at the right. After subtracting the "drift-plane", the topography image, Fig. 3.2(c), reveals the granular structure of the polycrystalline sample with grain sizes around 20 nm and height variations of ±0.65 nm. The magnetic

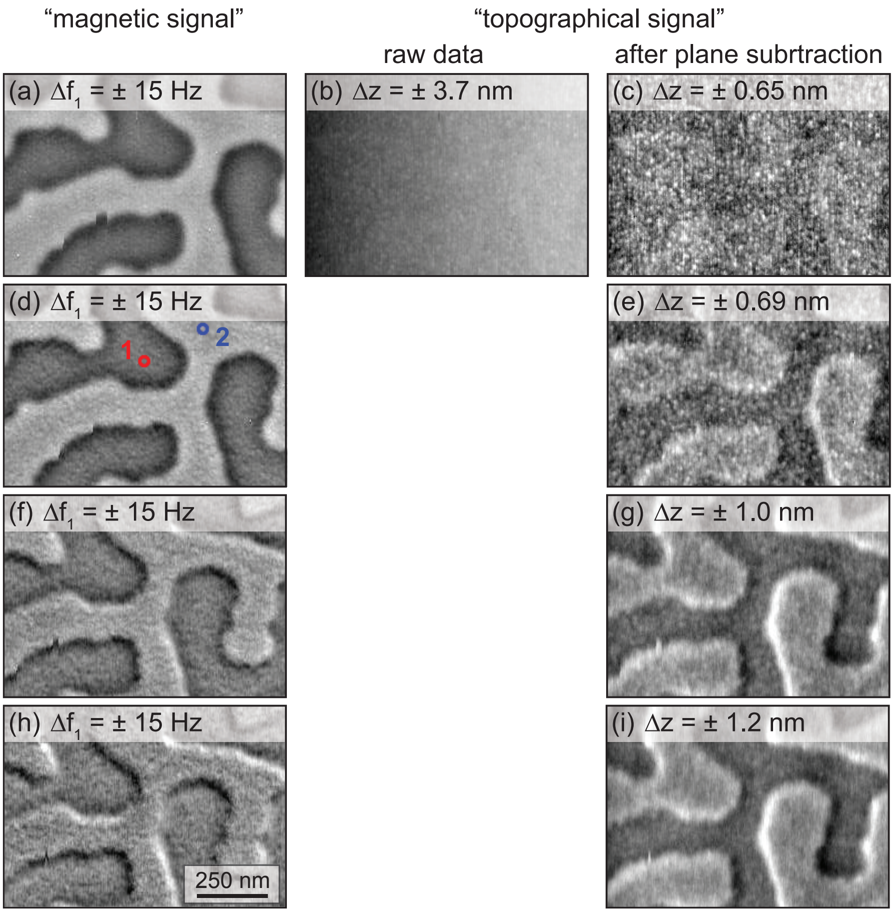

Figure 3.2: Images (a) to (c) were measured with an $A_1 = 12\,\text{nm}$. (a) magnetic image (first mode frequency shift). (b) topography image revealing the drift of the tip-sample distance (the image was scanned from bottom to top and left to right) and the grain structure. The latter becomes better visible in image (c) where the drift plane has been subtracted. Magnetic contrast and topography images for $A_1$ equal to 6 nm, 3 nm, and 1.5 nm are shown in panels (d) and (e), (f) and (g), and (h) and (i), respectively. The amplitude of the second mode was kept $A_2 = 0.27\,\text{nm}$ for all measurements. Note that the $\Delta f$ or $\Delta z$ values given in the images represent the displayed grey scales, and not the actual extrema of the image contrast. Thus corresponding images can be directly compared. The red and blue circles in panel (d) mark the acquisition locations of the frequency-distance curves shown in Fig. 3.3.

domains are faintly visible, however, (a contrast of about 0.1 nm) indicating that the separation of magnetic and van der Waals forces is not perfect.

Reducing the $A_1/A_2$-ratio from the initial 44 down to 22 in fig. 3.2(d),(e), 11 in fig. 3.2(f),(g), and 5.6 in fig. 3.2(h),(i), the magnetic contrast in the $\Delta f_1^b$-signal decreases, while it increases in the z-feedback output images. To understand this, note that the bimodal frequency shift $\Delta f_2^{(b)}$ is smaller than the unimodal frequency shift $\Delta f_2$ because in bimodal operation the $\Delta f_2^{(b)}$ is averaged over the tip-sample distance range spanned by the first mode oscillation amplitude $A_1$. With smaller amplitude $A_1$ this averaging of the second mode frequency shift occurs over a smaller z-range. In that case $\Delta f_2^{(b)}$ is larger, closer to the $\Delta f_2$ that would be obtained in unimodal operation. For the data shown in Fig. 3.2, the z-feedback setpoint was kept constant at -6.8 Hz for all selected amplitudes $A_1$. Consequently the z-feedback will increase the tip-sample distance if the first mode amplitude $A_1$ is reduced. At larger tip-sample distances the contribution of the longer-ranged magnetic forces to the frequency shift is more prominent, and the magnetic domain contrast becomes more apparent (Fig. 3.2(e),(g),(i) ) in the z-feedback output data. But since the z-feedback will partially have corrected for the spatially dependent magnetic forces, the magnetic contrast visible in the $\Delta f_1^{(b)}$-images (Fig. 3.2(d),(f),(h) ) is reduced.

We also acquired frequency shift versus distance curves simultaneously for the first and second mode, in the middle of a black and of a white domain (Fig. 3.2(d), points 1 and 2). We used oscillation amplitudes $A_1 = 6\,\mathrm{nm}$ and $A_2 = 0.27\,\mathrm{nm}$. At $z_{ltp} = 70\,\mathrm{nm}$, the contrast between the $\Delta f_1^{(b)}$ values obtained on the white (wd) and black domain (bd) corresponds to 5.9 Hz (blue-red arrow in Fig. 3.3(a). 70 nm away from the sample, the change of the force z-derivative over the tip's oscillation trajectory with the chosen oscillation amplitudes can then be neglected. Therefore the small amplitude approximation, i.e. Eq. 3.4 holds and $\Delta f_2^{(b)}(\mathrm{wd}) - \Delta f_2^{(b)}(\mathrm{bd}) \approx [\Delta f_1^{(b)}(\mathrm{wd}) - \Delta f_1^{(b)}(\mathrm{bd})] \cdot (\alpha_1/\alpha_2)^2 = 0.94\,\mathrm{Hz}$ agreeing well with the experimental value of 0.89 Hz (black arrows in Fig. 3.3(a). Because the second mode amplitude is small ($A_2 = 0.27\,\mathrm{nm}$), the second mode frequency shift, $\Delta f_2^{(b)}$ is dominated by the van der Waals force at small tip-sample distances. Hence the tip-sample distance required to correct between a magnetically attractive and -repulsive signal is extremely small. Assuming that the magnetic forces at these two points have

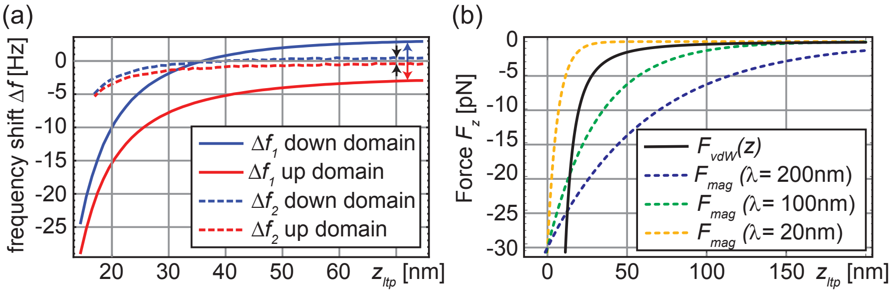

Figure 3.3: (a) First and second mode frequency distance curves measured with $A_1 = 6\,\mathrm{nm}$ and $A_2 = 0.27\,\mathrm{nm}$ at the locations marked with a red and blue circle in Fig. 3.2. (b) van der Waals force as a function of distance extracted from the first mode frequency shift curves shown in (a). Magnetic force as a function of distance for different spatial wavelengths. Note that at much larger tip-sample distance (not shown here) all $\Delta f$-curves will approach zero and all magnetic contrast vanishes.

equal magnitudes but opposite signs, the average of the two $\Delta f_1^{(b)}$-curves is solely caused by the van der Waals interaction. Using the matrix inversion method described by Welker et al.[21], the distance dependence of the van der Waals force $F_{vdW}(z_{ltp})$ (depicted in Fig. 3.3(b) ) can be extracted from the average frequency shift $\Delta f_{1,vdW}^{(b)}(z_{ltp})$. A model counterpart for this experimental van der Waals force is $F_{vdw}(z) = -c/(z - z_{offs.})^2$ with $c = 3.87 \cdot 10^{-27}\,\mathrm{Nm}^2$ (Fig. 3.3(b), solid black line). The constant $z_{offs.}$ is required because the zero-point of the z-scale in Fig. 3.3(a) is a priori unknown and an absolute zero-point can be defined to obtain $z_{offs.} = 0$. For comparison we also plot exponentially decaying magnetic forces $F_{mag}(z) = F_0 \cdot \exp(-kz)$ for spatial wavelengths $\lambda = 2\pi/k = 200,\ 100,$ and $20\,\mathrm{nm}$. The constant $F_0$ has been adjusted so that the 200 nm plot reproduces the experimentally determined contrast $\Delta f_1^{(b)}(wd) - \Delta f_1^{(b)}(bd) = 5.9\,\mathrm{Hz}$ at a tip-sample distance of 70 nm. Notice that the magnetic force arising from magnetization patterns with 20 nm spatial wavelength has a decay length similar to that of the van der Waals force. High-resolution MFM based on bimodal techniques is still possible, however, if the van der Waals force is much larger than the magnetic force arising from magnetic field features of small spatial wavelengths, i.e. if $\Delta f_{2,mag}^{(b)}(\Delta z) \ll \Delta f_{2,vdW}^{(b)}(\Delta z)$. Under this condition, a change of the magnetic force would be compensated by a negligible change of the tip-sample distance. Therefore the z-feedback image still reflects the topography and the $\Delta f_1^{(b)}$ image shows the magnetic image.

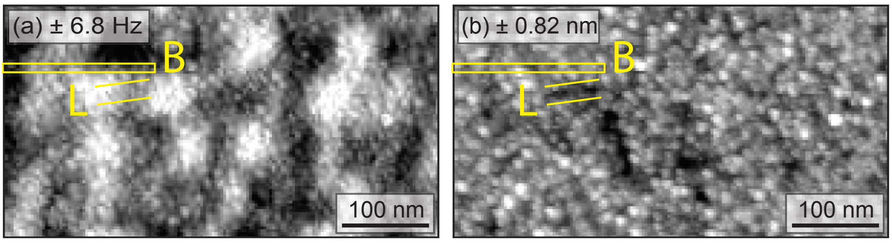

Figure 3.4: (a) high resolution magnetic image of a modern hard-disc recorded with $A_1 = 12\,\text{nm}$. (b) topography measured simultaneously with the magnetic signal with $A_2 = 0.27\,\text{nm}$. The grain structure is nicely visible in both images. The 10 nm high yellow box serves as a guide for the eye to judge the lateral resolution of the MFM image.

For high-resolution imaging (Fig. 3.4) the tip-sample distance must be kept small. The latter can be estimated from the frequency distance curve (Fig. 3.3(a) and the z-feedback set-point $\Delta f_2^{(b)} = -6.8\,\text{Hz}$ that was used for the data shown in Fig. 3.4. A lower turning point tip-sample distance of 7.6 nm is found. Note, however, that the proper function of the z-feedback requires a low noise $\Delta f_2^{(b)}$-signal at a reasonable measurement bandwidth. Using Eqs. 3.1 and 3.4 we find a $\Delta f_2$-noise of 0.66 Hz in a 100 Hz bandwidth for the high quality factor $Q_2 = 17'205$ obtained in vacuum for $A_2 = 0.27\,\text{nm}$. This noise must be compared with the second mode frequency shift obtained under bimodal operation. Hence, for typical quality factors obtained in air, a stable operation of the z-feedback on $\Delta f_2^{(b)}$, at a reasonable measurement bandwidth becomes challenging. This limits the application of bimodal MFM as proposed here to vacuum operation and reasonably small scan-ranges.

## 3.5 Conclusion

To summarize, we have presented a non-contact bimodal magnetic force microscopy technique capable of obtaining highest resolution and sensitivity for magnetic stray fields under vacuum conditions. However (as is also the case for conventional, lift-mode operation) the topography will be partly visible in the first mode frequency shift and may easily be mistaken for small magnetic features. This is because magnetic forces will vary as the tip follows local topographical features. For example, the grain structure visible inside the white bits in the magnetic image Fig. 3.4(a) is not caused by variations of the local magnetic structure, but arises from local changes of the *average* tip-sample distance. However in Fig. 3.4 in some locations (see for example the yellow box B with a height of 10 nm) the magnetic contrast changes from bright to dark from one grain to the next, although adjacent grains have the same topographical height. Such a contrast change must be of magnetic origin. Further, in some locations (see the parallel lines L) topographical features are visible that do not appear in the magnetic image. This indicates that a lateral resolution on the length scale of the grains, i.e. smaller than 10 nm could be obtained.

# 4 MFM with capacitive tip-sample distance control[2]

## Preface

This chapter is composed from the text and figures of the reference[2], published 2015 in Applied Physics Letters 107 by AIP Publishing. Authors of the paper are J. Schwenk, X. Zhao, M. Bacani, M. Marioni, S. Romer and H. J. Hug.

## 4.1 Introduction

Magnetic Force Microscopy is a versatile technique to image local magnetic fields with high spatial resolution[4]. It is achieved by scanning an ultrasharp, high-aspect ratio magnetic tip along the surface of the sample at small tip-sample distances under vacuum conditions. The latter is required for a high Q-factor of the cantilever, which in turn allows obtaining high sensitivity to small magnetic forces[1]. Usually a dual passage method is used, where each measurement line is scanned twice[6]. A first scan is carried out in the intermittent contact mode and reveals the topography. A subsequent scan takes place without tip-sample contact at a user selected lift height, following the topography data recorded in the first scan. However, the use of the intermittent contact mode in vacuum remains challenging[1].

Recently single passage measurement methods have been reported that use bimodal cantilever excitation suitable for operation in air[32] and in vacuum[1]. They rely on the ability to separate magnetic from non-magnetic (van der Waals or electrostatic) forces on the basis of their different decay lengths. But magnetic fields of small magnetic structures can have the same decay length as van der Waals forces, making the separation of magnetic and topography-induced forces difficult in these situations. Moreover, scanning at constant average height, as is often convenient for quantitative data analysis[38,39], or operation at larger tip-sample distances becomes challenging, because the situation arises where the (longer-ranged) magnetic forces dominate the (shorter-ranged) topographical forces. The latter can then no longer be used for tip-sample distance control. Additional problems arise if measurements are performed at different temperatures or external magnetic fields. Both change the resonance frequency of the free cantilever, requiring a re-adjustment of the frequency shift set-point used for recording the topography. Although such reset is possible, it is often impractical, e.g. when the magnetization of the magnetic coating on the cantilever beam settles slowly over time leading to a corresponding creep of the free resonance frequency.

## 4.2 Measurement principle

Here we propose a single passage measurement technique that overcomes these limitations. Figure 4.1 depicts its schematic setup which is implemented using a *Zurich Instruments HF2PLL* Lock-in amplifier with our modified *Nanoscan hr-MFM* (see section 2.1) microscope. As in our previous work[1] a first phase-locked loop (PLL) is used to drive mechanically the cantilever on its first flexural resonance $f_1$, typically with an oscillation amplitude $A_1 = 10\,\mathrm{nm}$ (zero-to-peak), chosen to optimize the ratio between the measured magnetic force induced frequency shift and the frequency noise caused by thermal fluctuations[40,1]. Unlike our previous work[1] the second cantilever oscillation mode at $f_2 = 6.27 \cdot f_1$[22] is *not* driven mechanically but by applying an oscillatory tip-sample bias. In general, a bias of the form $U(t) = U_{dc} + U_{ac}\cos(2\pi f_{ac} t)$ generates an electrostatic force given by

$$\begin{aligned} F_E(z,t) &= \frac{1}{2}\frac{\partial C(z)}{\partial z} \cdot \left[\, U_{dc}^2 + 2U_{dc}U_{ac}\cos(2\pi f_{ac}t) \right. \\ &+ \left. U_{ac}^2\cos^2(2\pi f_{ac}t)\right], \end{aligned} \tag{4.1}$$

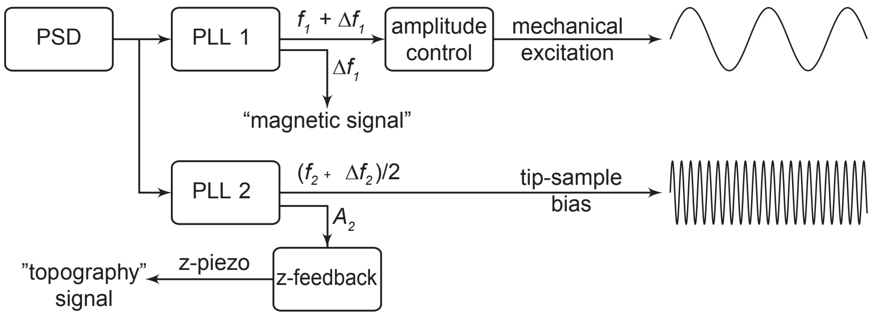

Figure 4.1: Schematic of the dual-PLL system required for bimodal oscillation of high quality factor cantilevers. The first PLL mechanically drives the cantilever on its first mode, and tracks shifts of its resonance frequency. The second PLL excites the cantilever via an oscillatory electric field at half the resonance frequency of its second mode. The $z$-feedback then keeps the obtained second mode oscillation amplitude constant to map the sample topography. The required $z$-travel then reflects the topography of the sample.

where $C(z)$ is the distance dependent tip-sample capacity, $U_{dc} = U_{dc}^{(K)} + U_{dc}^{(a)}$ is the sum of the contact and applied potential, and $U_{ac}$ is the amplitude of the potential modulation. We see from Eq. (4.1) that $F_E$ has components at frequency $f_{ac}$ and $2f_{ac}$, the latter being:

$$F_{E,2f_{ac}}(z) = \frac{1}{4}\frac{\partial C(z)}{\partial z} \cdot U_{ac}^2 \,. \tag{4.2}$$

In particular, a cantilever oscillation will be induced at $2f_{ac}$ that is proportional to $\partial C/\partial z$ but independent of $U_{dc}$ (and thus also insensitive to contact potentials). That is significant because $\partial C/\partial z$ carries information of the tip-sample distance, so that the amplitude at $2f_{ac}$ can be a measure thereof. A spatial dependence of the contact potential $U_{dc}^{(K)}$ would lead to a corresponding variation of the first (and second) mode frequency shift, unless the Kelvin potential is compensated through a suitable implementation of a Kelvin feedback loop.

By setting $f_{ac} = {}^1\!/_2 \cdot f_2$, i.e. half the second mode resonance frequency, resonance amplification ensures a conveniently large amplitude $A_2$, but a second PLL is needed to track $2f_{ac}$ as shown in Fig. 4.1. The latter requirement arises because magnetic forces acting on the tip and changes of the tip-sample distances, generate frequency shifts that can easily be larger than the width of the resonance peak and thus would significantly change the force-to-amplitude transfer function.

With the above setup we can obtain tip-sample distance dependent $A_2(z)$ curves, a representative example of which is given in Fig. 4.2(a), red line. Note that the first mode resonance frequency $\Delta f_1(z)$ can be measured simultaneously with the measurement of $A_2(z)$ – cf. Fig. 4.2(a), blue line. The monotonicity of $A_2(z)$ shows that it is suitable for controlling the tip-sample distance, i.e. modifying the value of $z$ by $\Delta z$ until $A_2(z)$ equals a predefined setpoint, provided the dielectric response of the sample remains constant within the scan area. Further, the quality factor $Q_2$ must remain constant. The latter could change if for example magnetic dissipation occurred. That would however also affect the first mode quality factor $Q_1$, which is not the case for our measurements.

Conveniently the slope of $A_2(z)$ increases with decreasing $z$, whereby the signal-to-noise ratio of the measured $A_2(z)$ is improved. This facilitates a faster control of the tip-sample distance when it is of the same order or smaller than the height variation of topographical features. Measuring with a $z$-feedback that rapidly adapts to the local conditions implies that $A_2(z)$ is (in an ideal case) constant, and that the map of the corresponding $\Delta z$ is a measure of the topography (*constant local height* imaging). Conversely, if the $z$-feedback is disabled, $A_2(z)$ should a priori vary with position in accordance with the topography. Note however, that by the unavoidable drift of the tip-sample distance the latter will change not only locally, but on average. Such drift, but not local variations of the tip-sample distance, will be corrected if the $A_2(z)$-based control is retained but made sufficiently slow. With a slow $z$-feedback mode a type of *constant average height* imaging mode is obtained, wherein $A_2(z)$ is a measure of topography. Importantly, very small to almost arbitrarily large average distances from the sample surface can be maintained, on account of the large range where $\frac{\partial C(z)}{\partial z}$ varies. This represents a major advantage to the aforementioned bimodal technique[1]. The second mode amplitude $A_2$ as well as the first mode frequency shift $\Delta f_1$ are plotted in figure 4.2 (c) as a function of the bias voltage $U_{\mathrm{dc}}$. As argued above and expected from equation 4.1 the $A_2$ signal is not influenced by the variation of the tip sample bias. The frequency shift $\Delta f_1$ on the other hand, exhibits the typical parabolic behaviour.

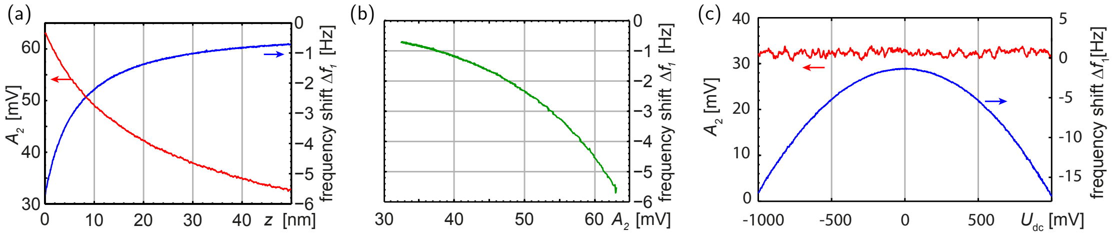

Figure 4.2: (a) Second mode amplitude $A_2(z)$ (red line), and first mode frequency shift $\Delta f_1(z)$ (blue line) as a function of tip sample distance. (b) The measured $\Delta f_1$-signal is re-plotted as a function of $A_2$. (c) second mode amplitude $A_2$ (red line) and frequency shift (blue line) $\Delta f_1$ as a function of tip sample bias potential $U_{\mathrm{dc}}$

## 4.3 Experimental example

To investigate the characteristics of this control mode in greater practical detail we work with a $\mathrm{Ta}_{5\mathrm{nm}}/\mathrm{Pt}_{5\mathrm{nm}}/[\mathrm{Co}_{0.4\mathrm{nm}}/\mathrm{Pt}_{0.7\mathrm{nm}}]_{\times 4}/\mathrm{Pt}_{3.5\mathrm{nm}}$ multilayer deposited onto a hexagonal array of domes in an anodic alumina template with 100 nm period, similar to Ref.[41]. This sample provides small magnetic features, but also large topographical ones which typically constitute a major difficulty for high-resolution magnetic force microscopy. In prior work[42] the topography of such a sample was measured in air, with the intermittent contact mode. The typical bump-to-bump height variation was found to be around 5 nm, but at defects much larger height variations of up to ±8 nm – cf. Fig. 4.3(a) – were measured.

A Team-Nanotec cantilever without coating, with a length of 225 $\mu$m, a width of 35 $\mu$m, and a nominal stiffness of 0.7 N/m was used. Its high aspect ratio tip was made sensitive to magnetic stray fields by sputter coating one tip side with 2 nm Ti and 4 nm Co, and subsequently magnetizing it to have a north pole at the tip end. The contact potential of 592 mV was compensated (i.e. $U_{dc} = 0$ ). An oscillatory potential $U_{ac} = 500\,\mathrm{mV}$ was applied resulting in the $A_2(z)$ curve depicted in red in Fig. 4.2(a) for a range of $z$.

Figure 4.3(a) and (b) show two simultaneously recorded channels of a first scan, taken in zero field, in which $A_2$ was kept constant with a fast feedback loop that varied $z$. It is an example of *constant local height* imaging. The left panel is the map of ±8 nm $\Delta z$-travel required to keep $A_2$ constant during the scan, and is a measure of the topography $\Delta z_m(x, y)$. For instance, it can be used to align images acquired in different fields. The corresponding Fig. 4.3(b) shows the first mode frequency shift $\Delta f_1(x, y, z_m(x, y))$. It contains a pattern of spots congruent with Fig. 4.3(a), with an additional contrast pattern that is usually associated with the magnetic up and down domains (cf. Ref[42]). The yellow/blue circles in Figs. 4.3(b) and (c) indicate domes with an up/down magnetization. Magnetic contrast with high spatial resolution can also be obtained between the domes, but is generally difficult to assess whether such an area can switch its magnetization independently from that of the adjacent domes. In most cases an area between two domes changes its contrast from bright to dark if both adjacent domes switch from up to down. This could be caused by the magnetic exchange coupling of the film on the domes with the film at the location of the intermediate area, but could also be an artifact arising from a limited spatial resolution of the MFM. However, at least at a few positions – highlighted in the blue insets in Figs. 4.3(b), (c) and (d) – the magnetization of the domes switch from up to down while part of areas between the two adjacent domes remains up (white) in a field of -153 mT, but switch to down in a field of -406 mT.

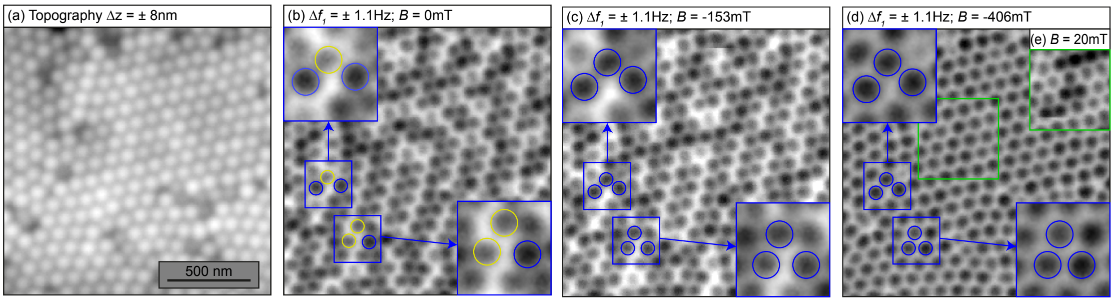

Figure 4.3: Data obtained with $A_2$ kept constant, i.e. using a fast $z$-feedback. (a) Signal from the topography of the sample, i.e. the ±8 nm $z$-travel required to keep $A_2$ constant during scanning. (b) $\Delta f_1(x, y)$ MFM data recorded simultaneously with (a) in zero field. The yellow/blue circles highlight dots with an up/down magnetization. (c) MFM image taken at -153 mT. An area between the dots with an up magnetization is visible between the three domes inside the blue frames. (d) MFM data acquired in a field of -406 mT that saturates the magnetic layer. (e) MFM measurement at +20 mT of the area framed in green in (d).

A salient feature of the above $\Delta f_1(x, y, z_m(x, y))$ images is the presence of dark spots at the centers of the domes, irrespective of the underlying magnetization orientation. In order to exclude that this contrast is of magnetic origin the area highlighted by the green frame in Fig. 4.3 was also measured in a field of +20 mT. At such a field most of the film retains the down-state obtained at -406 mT field, as known from prior work[42], but the magnetization of the tip has flipped. The latter can be seen from the dark contrast arising from the very few areas of the film with a magnetization direction changed from the down- to the up-state (see Fig. 4.3(e)). The dark spots (domes) however remain the most prominent features in the $\Delta f_1$ image, although the tip magnetization is now antiparallel to the majority of the sample areas. If the contrast was of magnetic origin, the domes should now appear as white circles which is clearly not the case. Hence, apart from a small modification of the grey-level of the contrast at the location of the domes, the dark spots visible in all $\Delta f_1$ images are not of magnetic origin, but arise from a spatial variation of the van der Waals force, as already pointed our earlier work[42].

However, in the present work $A_2$ was kept constant. One might thus expect that the local tip-sample distance, and thus also the van der Waals interaction remains constant. Then the domes should not be visible. The data taken in saturation (Fig. 4.3(d)), however, shows that this is not the case. The reason for this discrepancy can be traced back to the different interaction length of two involved tip-sample forces: electrostatic ($U_{ac} \neq 0$) and attractive van der Waals ones, and thus of the respective interaction volumes. The difference is confirmed by the departure from linearity of $\Delta f_1(A_2)$ (Fig. 4.2(b)), taking into account that the magnetic part of the interaction does not alter this fact. Therefore, the van der Waals contribution to $\Delta f_1$ will not remain constant when the tip traces lines of constant $A_2$, and the $z$-travel $\Delta z_m(x, y)$ required to keep $A_2$ constant will differ (slightly) from the true topography of the sample. Consequently, the domes will remain visible even if the image is acquired in a saturating field of -406 mT – cf. Fig. 4.3(d).

A more practical limitation of the *constant local height method* is that because of the small size of the $A_2$ the signal-to-noise ratio (SNR) available for $z$-control is limited. As a consequence the $z$-position noise and thus also the $\Delta f_1$ noise in the image increases with the $z$-feedback speed, a fact that ultimately limits the sensitivity for small magnetic forces. Samples generating only weak stray fields are thus best measured at constant *average* height, i.e. with slow proportional and integral parameters of the $z$-feedback. They should be sufficiently fast to correct drift of the tip-sample distance but slow enough that localized topographical features encountered during the scan do not trigger a $z$-correction. Note that appart from allowing to scan faster this method facilitates the quantitative interpretation of the MFM data[38].

Figure 4.4 displays one such *constant average height* measurement of the same area shown in Fig. 4.3. The data were acquired in zero field, immediately after the constant $A_2$-scan in zero field was completed. The magnetic state of the sample thus is the same as shown in Fig. 4.3(b). The variations of $A_2$ (Fig. 4.4(a)) using this measurement mode arise when local topography is (mostly) not compensated by the feedback. These images of $A_2(x, y)$, taken at constant average height, can be translated into a frequency shift using the $\Delta f_1^{vdW}(A_2)$ dependence plotted in Fig. 4.2(b), which was derived from the measurements (Fig. 4.2(a)). The result of this computation is shown in Fig. 4.4(c). It can now be subtracted from the 'raw' $\Delta f_1(x, y)$ data (Fig. 4.4(b)) to enhance the relative weight of magnetic information in it. Figure 4.4(d) displays the result, which qualitatively and quantitatively matches that acquired at constant local $A_2$ (Fig. 4.3(b)). It shows a substantial

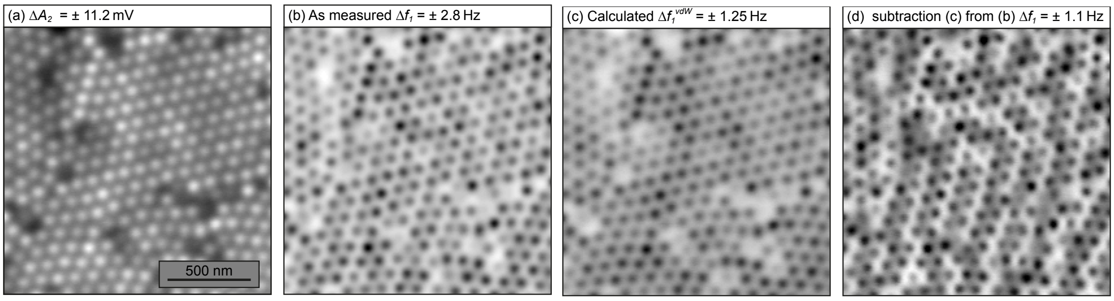

Figure 4.4: (a) $A_2(x, y)$ data arising from topography-induced variations of the tip-sample distance. (b) Simultaneously measured $\Delta f_1(x, y)$ frequency shift data recorded at constant *average* tip-sample distance, i.e. with a slow $z$-feedback. (c) Van der Waals force induced variations of the frequency shift $\Delta f_1^{vdW}$ calculated from the $\Delta f_1(A_2)$-curve depicted in Fig. 4.2(c). (d) Result of subtracting the data in (c) from that of (b), showing a magnetic interaction force-dominated image, which resembles the MFM image measured with a fast $z$-feedback shown in Fig. 4.3(b).

magnetic contrast with a weak background arising from the incomplete compensation of local van der Waals force variations. Clearly, an ideally local treatment of van der Waals and electrostatic tip-sample interactions is an approximation that deteriorates when the sample topography is comparable to the tip that images it. Future implementations of this techniques could rely on an explicit deconvolution, utilizing separate calibration measurements, to more perfectly compensate the topography-induced effects.

The frequency shift data acquired with a fast z-feedback with B-fields spanning from 0 mT to 400 mT are depicted in figure 4.5. The series is also recorded with slow feedback parameters. For comparison with figure4.5, figure 4.6 shows the difference between the measured $\Delta f_1$-signal and the van der Waals force induced frequency shift $\Delta f_1^{vdW}$ (compare also to figure 4.4). As in the previous figures 4.3 and 4.4 all images in both measurement methods are represented in a contrast scale of $\Delta f_1 = \pm 1.1\,\mathrm{Hz}$ for white to black. The measurements with fast and slow feedback parameters were following each other for each $B$-field value. The alignment of the data is based on the topography channel in the case of fast feedback parameters and on the $A_2$ channel for the data taken under slow feedback conditions.

## 4.4 Concluding remarks

At this point it is convenient to note that the technique for distance control presented here could also prove useful for large area non-contact measurements of the Kelvin potential. The $z$-feedback that keeps $\Delta f_1$ (the frequency shift arising from van der Waals or interatomic forces) constant represents the topography only if the Kelvin potential is locally compensated. Usually this means that two feedbacks (the Kelvin- and the distance feedback) are arranged in series, rendering the selection of appropriate feedback parameters challenging and reducing the overall feedback speed. From equation Eq. 4.1 follows that the $A_2$ signal is independent from the dc-potential (applied and Kelvin potential). Hence, a distance feedback using the $A_2$ signal will not be affected by the (slow) Kelvin feedback.

More fundamentally, a distance feedback relying on van der Waals (or interatomic) forces requires the use of small tip-sample distances, an inherent difficulty

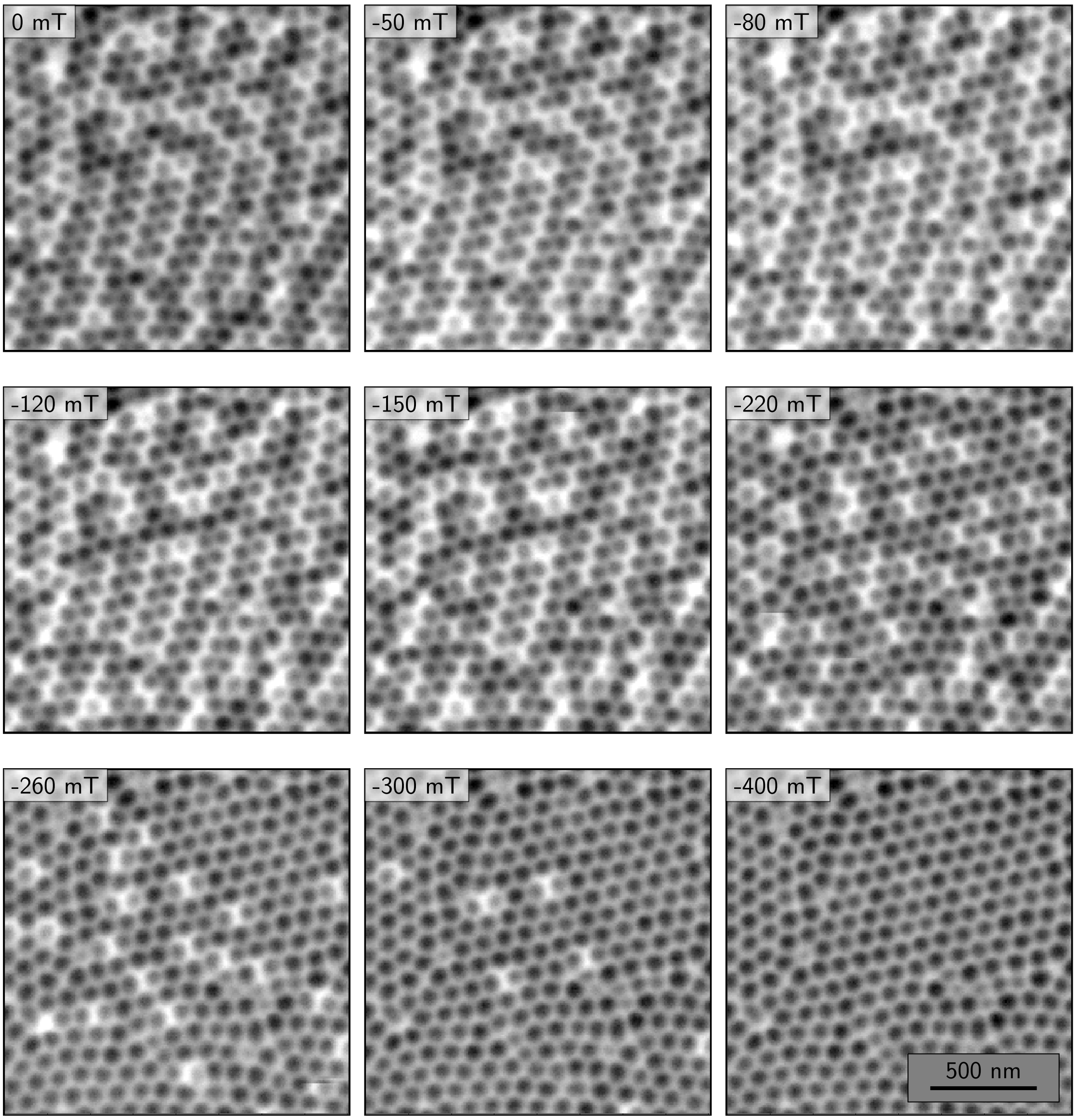

Figure 4.5: The complete field series measured with fast distance feedback in a field range from $B = 0\,\mathrm{mT}$ to $B = 400\,\mathrm{mT}$. The white to black contrast scale is $\Delta f_1 = \pm 1.1\,\mathrm{Hz}$ for all images.

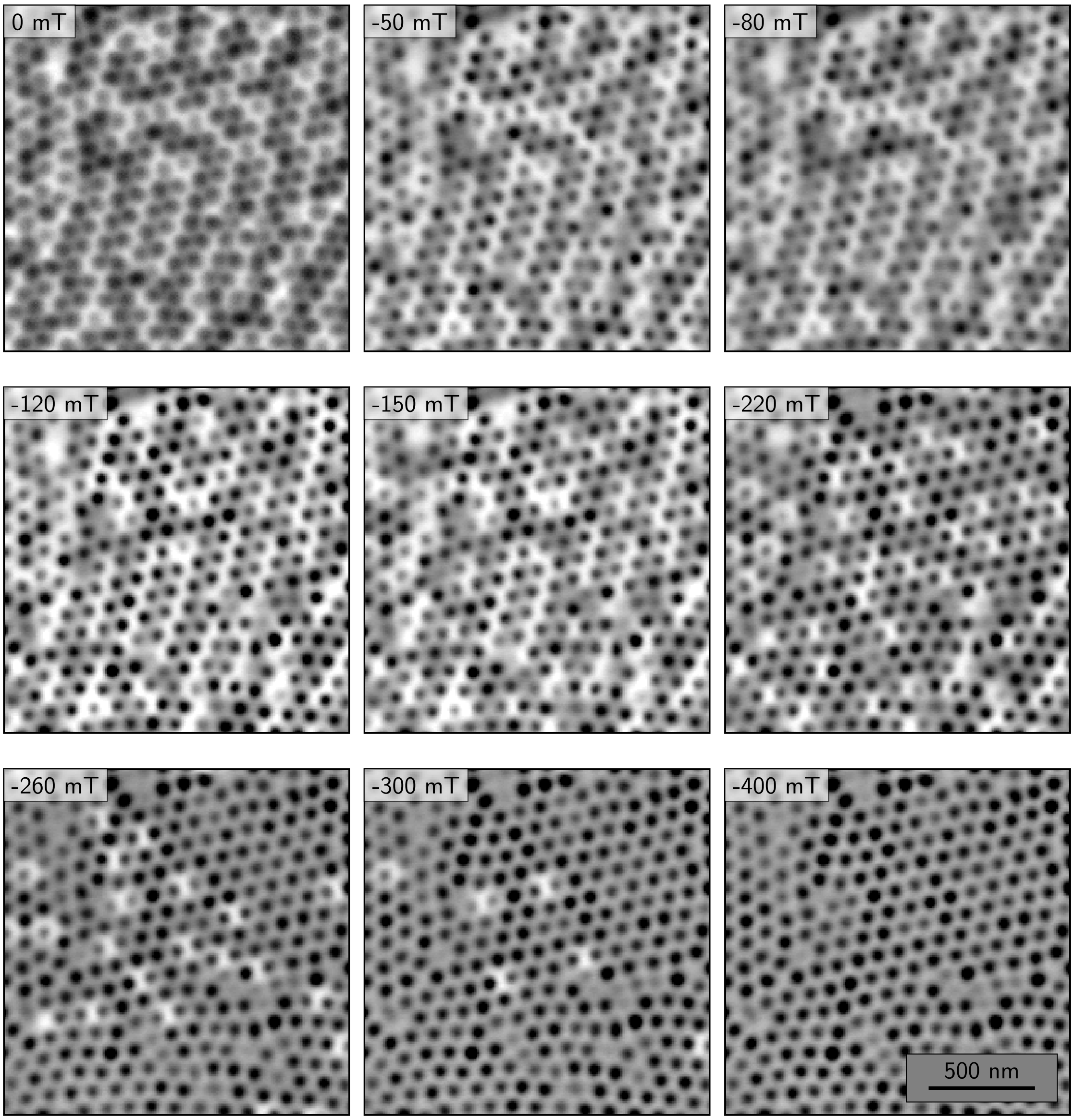

Figure 4.6: The complete field series measured with slow distance feedback in a field range from $B = 0\,\text{mT}$ to $B = 400\,\text{mT}$. The white to black contrast scale is $\Delta f_1 = \pm 1.1\,\text{Hz}$ for all images.

in large area-scans of samples with substantial topography.

In conclusion, the capacitively controlled methods just discussed provide the experimenter with a robust technique for approaching, measuring and studying magnetic structures in the presence of non-negligible topography. It can be seen that any Scanning Force Microscopy technique where $C(z)$ can be measured will benefit from the control of the tip-sample distance independently from non-capacitive tip-sample interaction forces of interest.

**Acknowledgments:** We thank L. Piraux, S. K. Srivastava, V. A. Antohe, M. Hehn, and T. Hauet for the preparation of the sample.

# 5 Magnetic skyrmions in thin film materials

Magnetic skyrmions are quasi-particles that are formed by spin textures with a certain topology and were proposed by Bogdanov and Yablonskiĭ[43] in 1989. This topology provides an exceptional stability for the skyrmions[44] since it is not possible to annihilate the structure by a continuous transformation of their spin texture[45]. Responsible for the formation of magnetic skyrmions is the DM interaction between neighboring magnetic spins in the material, which is discussed further in section 5.1. This topological stability of the skyrmions, and the possibility of current-induced manipulation suggest an application of magnetic skyrmions in magneto-electronic and data-storage devices[46,47].

Magnetic skyrmions where observed first in crystalline materials as in bulk MnSi by neutron diffraction by Mühlbauer et al.[48] and in thin films of $Fe_{0.5}Co_{0.5}Si$ by Yu et al. using Lorentz Transmission Electron Microscopy (TEM)[49]. For applications, thin film stacks of magnetic multilayer materials, exhibiting an interfacial DM interaction, are the most promising class of materials. Typical industrially applied deposition tools can be used for fabrication of these films, and their magnetic properties can be tuned via their layer stacking, materials and layer thicknesses. Such multilayer systems are further discussed in section 5.2. Studying sputtered multilayer systems with interfacial DM interaction has thus a high technological relevance.

For such studies the MFM is expected to play an important role. Higher spatial resolution is possible by spin-polarized Scanning Tunneling Microscopy (STM)[50], but only clean single crystalline surfaces can be studied and so far experiments have only been performed at low temperatures. Lorentz TEM[49] and X-ray Magnetic Circular Dichroism (XMCD) Scanning Transmission X-ray Microscopy (STXM)[51] require electron or x-ray transparent samples, respectively, such that thin film samples on thicker substrates can not be studied. MFM does not suffer from these limitations.

## 5.1 Dzyaloshinskii-Moriya interaction

The Dzyaloshinskii-Moriya (DM) interaction favors a perpendicular alignment of neighboring atomic spins $\mathbf{S}_\mathrm{i}$ and $\mathbf{S}_\mathrm{j}$[52]. In addition to other magnetic energy contributions a DM coupling energy can be defined as

$$E_\mathrm{DM} = \sum_{\mathrm{i,j}} \tilde{\mathbf{D}}_\mathrm{i,j} \cdot (\mathbf{S}_\mathrm{i} \times \mathbf{S}_\mathrm{j}). \tag{5.1}$$

The vector $\tilde{\mathbf{D}}_\mathrm{i,j}$ describes the strength as well as the preferred relative orientation of neighboring spins $\mathbf{S}_\mathrm{i}$ and $\mathbf{S}_\mathrm{j}$. For thin isotropic films an interfacial DM interaction with an isotropic constant $\tilde{D}$ is described by

$$\tilde{\mathbf{D}}_\mathrm{i,j} = \tilde{D} \frac{\mathbf{r}_\mathrm{i} - \mathbf{r}_\mathrm{j}}{|\mathbf{r}_\mathrm{i} - \mathbf{r}_\mathrm{j}|} \times \hat{\mathbf{z}} \tag{5.2}$$

with the coordinate vectors $\mathbf{r}_\mathrm{i}$, $\mathbf{r}_\mathrm{j}$ for the sites i,j and the unit vector of the film normal $\hat{\mathbf{z}}$ and. A continuous description with the reduced magnetization vector $\mathbf{m} = \mathbf{M}/|\mathbf{M}|$ is obtained for the energy[52,43]

$$E_\mathrm{DM} = d \cdot \int D \left[ \left( m_\mathrm{x} \frac{\partial m_\mathrm{z}}{\partial x} - m_\mathrm{z} \frac{\partial m_\mathrm{x}}{\partial x} \right) + \left( m_\mathrm{y} \frac{\partial m_\mathrm{z}}{\partial y} - m_\mathrm{z} \frac{\partial m_\mathrm{y}}{\partial y} \right) \right] d\mathbf{r} \tag{5.3}$$

with an effective continuous DM interaction D and for a thin film which is homogeneous along its thickness direction $z$ and has a thickness $d$. As a consequence of the DM interaction one selected sense of rotation of the magnetization vector $\mathbf{M}$ in a system with uni-axial anisotropy becomes favored over the other one.

The energy term $E_\mathrm{DM}$ competes with the usual symmetric exchange energy in ferromagnets

$$E_\mathrm{ex} = d \cdot \int A \left[ \left( \frac{\partial \mathbf{m}}{\partial x} \right)^2 + \left( \frac{\partial \mathbf{m}}{\partial y} \right)^2 \right] d\mathbf{r} \tag{5.4}$$

with the exchange constant $A$ and the anisotropy energy

$$E_{\text{an}} = d \cdot \int -K(\mathbf{m} \cdot \hat{\mathbf{z}})d\mathbf{r}, \tag{5.5}$$

where $K$ is the uniaxial magnetic anisotropy constant.

### 5.1.1 Domain walls in samples with DM interaction

As pointed out by Rohart and Thiaville[52] the DM interaction has no influence on the width of a one dimensional domain wall as long as the domain wall energy (see equation 5.8) remains positive. The DMI can however change the domain wall type from a Bloch wall with arbitrary sense of rotation to a chiral Néel wall where one sense of rotation is preferred.

The angle between the magnetization vector and the $z$-axis as a function of the position $x$ is hence

$$\theta(x) = 2 \cdot \arctan\left[\exp(\pm\frac{x - x_0}{\sqrt{A/K}})\right]. \tag{5.6}$$

The sign of the argument in the exponent is given by he sign of $D$ and determines the rotational sense of the domain wall i.e. its chirality. The characteristic width of the domain wall $\delta_{\text{dw}}$ is given by the exchange stiffness $A$ and the anisotropy constant $K$ with

$$\delta_{\text{dw}} = \pi\sqrt{A/K} \tag{5.7}$$

The areal energy density of a domain wall is[53,52]

$$\sigma_{\text{dw}} = 4\sqrt{AK} \mp \pi D. \tag{5.8}$$

## 5.2 Interfacial DM interaction

In thin magnetic films an interfacial DM interaction can be induced by the interaction at the interface between the layers of the magnetic material and an high spin-orbit coupling material[54,52].

A DM interaction occurs at interfaces between transition-metals and heavy elements such as iridium (Ir)/nickel (Ni)[55], Ir/Co[56,8], platinum (Pt)/Ni[55] , or Pt/Co[56,8]. In a multilayer system where the top and bottom interfaces are different, the DM interaction of the top interface is not compensated by that of the bottom interface. In this case the system exhibits an overall DM interaction. In the present study, Co is used as a ferromagnetic material, and the DM interaction is generated by Pt/Co or Ir/Co interfaces. The interfacial DM interactions at the Pt/Co interface given in previous studies vary between the theoretically predicted value of $D_{\mathrm{Pt/Co}} = +2.59\,\mathrm{mJ/m^2}$ given by Yang *et al.*[57] and $D_{\mathrm{Pt/Co}} = +2.05 \pm 0.3\,\mathrm{mJ/m^2}$ determined experimentally by Boulle *et al.*[58]. The positive sign of the interaction corresponds to a counter clockwise rotation of the spins across the Néel type domain walls. For the Ir/Co interface values range from $D_{\mathrm{Ir/Co}} = -0.32\,\mathrm{mJ/m^2}$ in ref.[57] and an experimental estimate of $D_{\mathrm{Ir/Co}} = +0.53 \pm 0.12\,\mathrm{mJ/m^2}$ by Chen *et al.*[56]. For both interfaces the $D$-values are given for the Co-layer on the top. The overall DM interaction for a Pt/Co/Ir structure can thus be estimated by $D \approx D_{\mathrm{Pt/Co}} - D_{\mathrm{Ir/Co}}$ and is expected to be in the range of $D \approx 2.91\,\mathrm{mJ/m^2}$ and $D \approx 1.52\,\mathrm{mJ/m^2}$.

## 5.3 Sample preparation

Two different multilayer samples were fabricated by sputter deposition in an UHV AJA Orion sputtering system. Both samples are grown on silicon (100) substrates with a native oxide layer. Argon is used as a sputter gas with a pressure of 0.2 Pa during the deposition of all metal layers. One sample with asymmetric interfaces (ASI) is prepared with a layer structure of $\mathrm{Pt_{10nm}\,Co_{0.6nm}Pt_{1nm}[Ir_{1nm}Co_{0.6nm}Pt_{1nm}]_{\times 5}}$, covered with 3 nm of Pt and similar to the samples fabricated by Moreau-Luchaire et al[8]. A second sample with symmetric interfaces (SI) and the layer structure of $\mathrm{Pt_{10nm}[Co_{0.6nm}Pt_{1nm}]_{\times 5}Pt_{3nm}}$ serves as a reference sample without DM interaction. The latter is also used to determine the $TF$ of the MFM tip. Table 5.1 summarizes the layer thicknesses of the samples. The surface roughness as well as the density of particles on the surfaces of these samples are sufficiently low to enable MFM measurements at constant average tip sample distances around 10 nm. Illustrations of the layer structure together with MFM images of the domains in their

|  |  |  |  |
|---|---|---|---|
| Platinum: | $d_{\mathrm{Pt}}$ | = | 1 nm |
| Iridium: | $d_{\mathrm{Ir}}$ | = | 1 nm |
| Cobalt: | $d_{\mathrm{Co}}$ | = | 0.6 nm |
| Pt top layer: | $d_{\mathrm{top}}$ | = | 4 nm |

Table 5.1: Summary of the layer thicknesses in the samples SI and ASI.

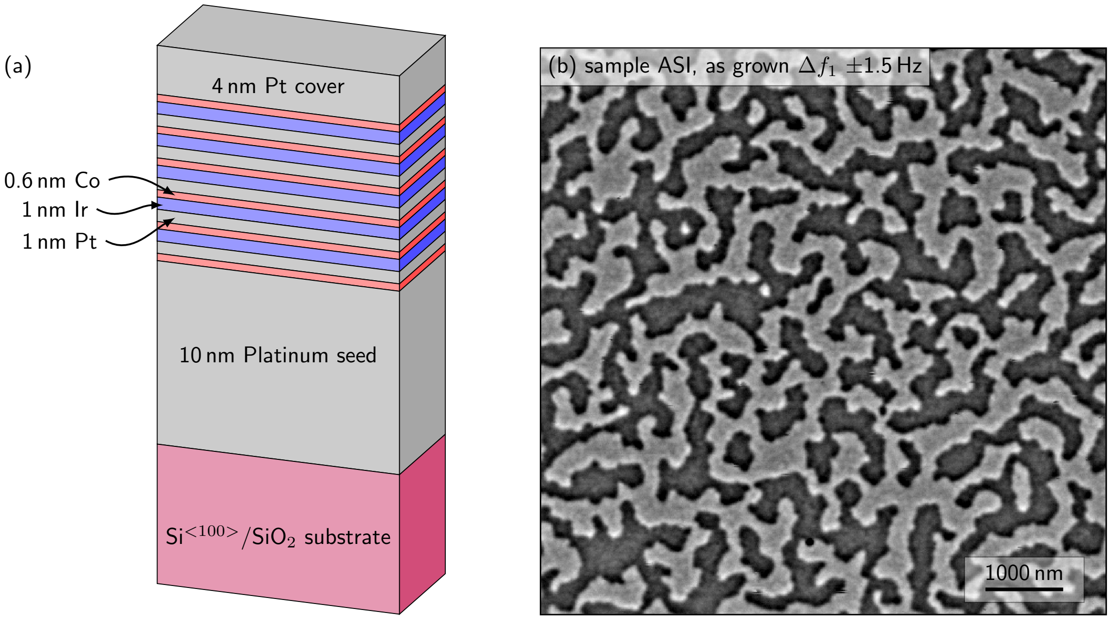

Figure 5.1: The layer structure of the sample ASI is illustrated in panel (a). Panel (b) depicts the $\Delta f_1$ data of a 5$\mu$m×5$\mu$m MFM-scan on sample in the as grown state.

as-grown state are shown in figure 5.1 for the sample ASI and in figure 5.2 for the sample SI. Both samples exhibit a perpendicular magnetic anisotropy which is quantified by vibrating sample magnetometry (VSM) measurements presented in the following section 5.4. The difference of the observed domain sizes in figures 5.1(b) and 5.2(b) arises from an interfacial DM interaction (see section 5.5).

## 5.4 Macroscopic magnetic characterization: VSM

In order to determine the macroscopic magnetic parameters of the samples SI and ASI we acquired magnetization loops of both samples with VSM. The loops

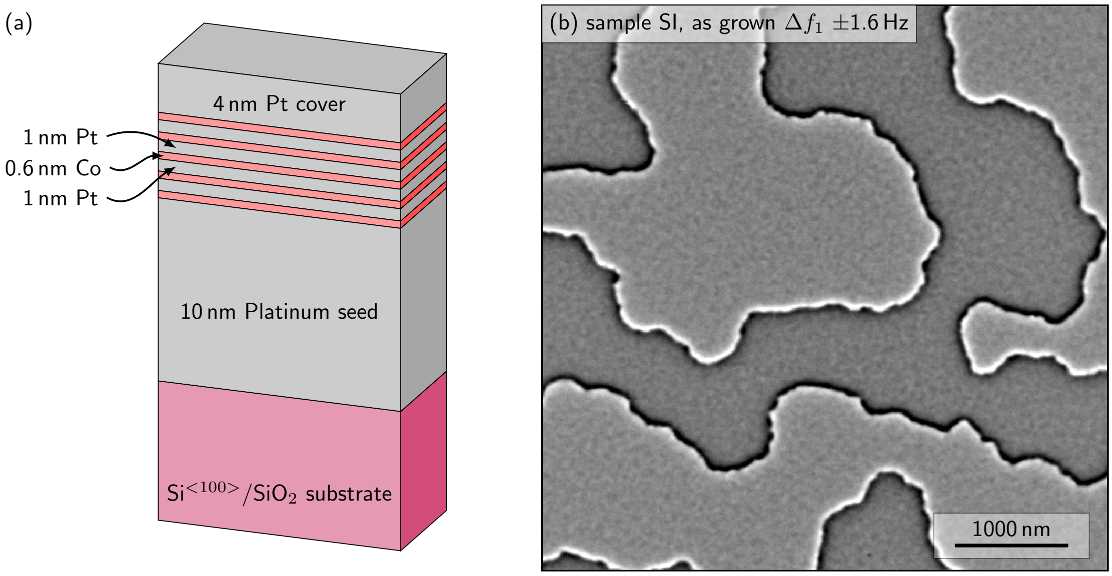

Figure 5.2: The layer structure of the sample SI is illustrated in panel (a). Panel (b) depicts the $\Delta f_1$ data of a $5\mu$m$\times 5\mu$m MFM-scan on sample in the as grown state.

recorded in perpendicular and in-plane geometry are plotted in figure 5.3 for the sample ASI and in figure 5.4 for sample SI. The values for the saturation magnetization $M_\mathrm{s}$ are determined under the assumption that the magnetic moments are restricted to the volume of the cobalt layers. The total thickness of Co is $5d_\mathrm{Co} = 3\,\mathrm{nm}$ for the sample SI and $6d_\mathrm{Co} = 3.6\,\mathrm{nm}$ for the sample ASI. The value for the exchange stiffness of $A = 16\,\mathrm{pJ/m}$ given in the tables of figures 5.3 and 5.4 is not measured but taken from Rohart and Thiaville[52].

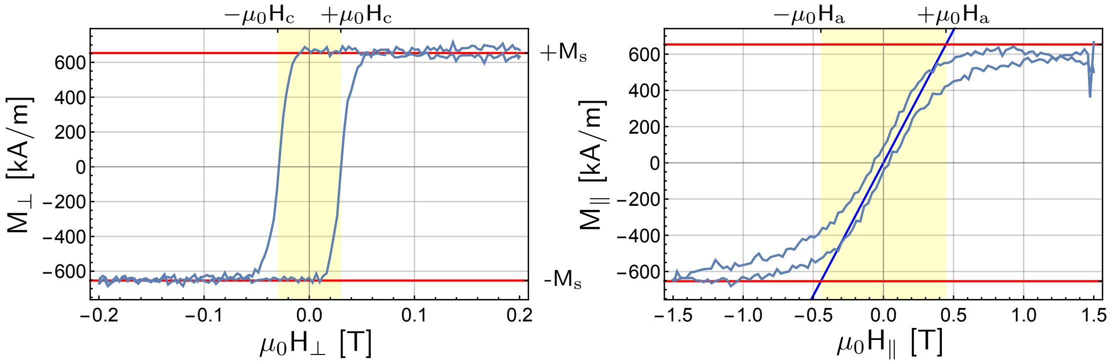

| | | | | | |
|---|---|---|---|---|---|
| $A$ | $=$ | $16\,\mathrm{pJ/m}^{52}$ | $K_{\mathrm{eff}}$ | $=$ | $\frac{1}{2}\mu_0 H_{\mathrm{a}} M_{\mathrm{s}} = 0.146\,\mathrm{MJ/m}^3$ |
| $M_{\mathrm{s}}$ | $=$ | $653.6\,\mathrm{kA/m}$ | $K_{\mathrm{ms}}$ | $=$ | $\frac{1}{2}\mu_0 M_{\mathrm{s}}^2 = 0.268\,\mathrm{MJ/m}^3$ |
| $\mu_0 H_{\mathrm{a}}$ | $=$ | $446.1\,\mathrm{mT}$ | $K_{\mathrm{u}}$ | $=$ | $K_{\mathrm{eff}} + K_{\mathrm{ms}}{=}0.414\,\mathrm{MJ/m}^3$ |

Figure 5.3: Magnetization curves with the field applied perpendicular perpendicular (left) and in-plane geometry (right) for sample ASI, measured with vibrating sample magnetometry. The table summarizes the magnetic properties obtained from the analysis of the loops.

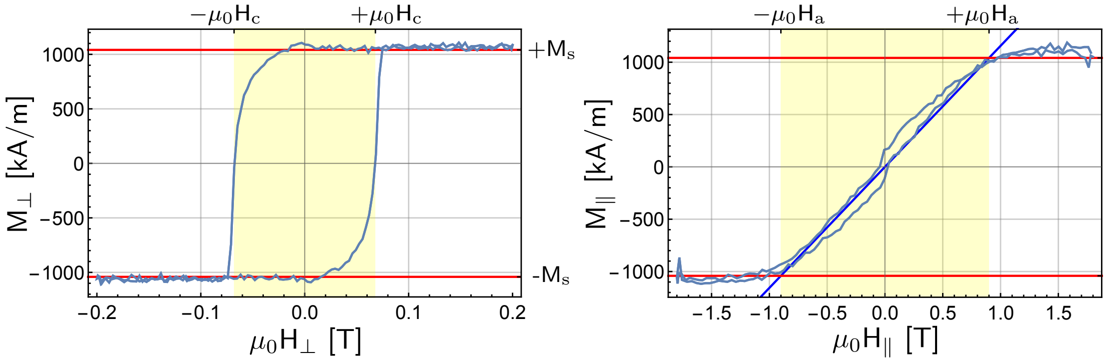

| | | | | | |
|---|---|---|---|---|---|
| $A$ | $=$ | $16\,\mathrm{pJ/m}^{52}$ | $K_{\mathrm{eff}}$ | $=$ | $\frac{1}{2}\mu_0 H_{\mathrm{a}} M_{\mathrm{s}} = 0.469\,\mathrm{MJ/m}^3$ |
| $M_{\mathrm{s}}$ | $=$ | $1041\,\mathrm{kA/m}$ | $K_{\mathrm{ms}}$ | $=$ | $\frac{1}{2}\mu_0 M_{\mathrm{s}}^2 = 0.681\,\mathrm{MJ/m}^3$ |
| $\mu_0 H_{\mathrm{a}}$ | $=$ | $900.4\,\mathrm{mT}$ | $K_{\mathrm{u}}$ | $=$ | $K_{\mathrm{eff}} + K_{\mathrm{ms}}{=}1.150\,\mathrm{MJ/m}^3$ |

Figure 5.4: Magnetization curves with the field applied perpendicular (left) and in-plane geometry (right) for sample SI, measured with vibrating sample magnetometry. The table summarizes the magnetic properties obtained from the analysis of the loops.

## 5.5 DM interaction and equilibrium domain size

The equilibrium domain size of a sample is determined by the minimum of the total magnetic energy. The latter is the sum of the magnetostatic energy and the domain wall energy that depends on the DM interaction (see equation 5.8). The total magnetic energy density of a sample with domains is

$$e_{\mathrm{tot}} = \frac{l_{\mathrm{dw}}}{A_{\mathrm{sample}}} \sigma_{\mathrm{dw}} + e_{\mathrm{ms}}, \tag{5.9}$$

with the magnetostatic energy density

$$e_{\mathrm{ms}} = -1/2 \mu_0 M_{\mathrm{s}} H_{\mathrm{d}}. \tag{5.10}$$

The quantity $\sigma_{\mathrm{dw}}$ is the energy per unit length of a domain wall given by equation 5.8, and $l_{\mathrm{dw}}$ describes the total length of all domain walls in an area $A_{\mathrm{sample}}$. The equilibrium domain size increases with higher values of $\sigma_{\mathrm{dw}}$, whereas a higher contribution of the magnetostatic energy density $e_{\mathrm{MS}}$ leads to a smaller equilibrium domain size.

### Measurements

Experimentally determined domain patterns for the sample ASI are depicted on the right hand side of figures 5.5 and 5.6. The patterns are obtained from MFM data measured on the sample as grown (fig. 5.5(a), right side) and after demagnetizing the samples with three different procedures:

- with an oscillatory B-field applied perpendicular to the sample surface (fig. 5.5(b) ),
- with an oscillatory B-field parallel to the sample surface (fig. 5.6(a) ),
- at a total magnetization of $M \approx 0$ obtained at the coercive field after saturation (fig. 5.6(b) ).

Details of the demagnetization process are described in section 2.3.

At equilibrium, the domain width is given by[59]

$$L_{\mathrm{eq}} = \frac{\pi}{2\sqrt{e}} d \cdot \exp\left[\frac{\pi\sigma_{\mathrm{dw}}}{\mu_0 M_{\mathrm{s}}^2 d}\right], \tag{5.11}$$

where $d$ is the thickness of the sample, $M_{\mathrm{s}}$ its saturation magnetization and $\sigma_{\mathrm{dw}}$ the energy density per unit area of the domain walls. With $\sigma_{\mathrm{dw}} = 4\sqrt{AK_{\mathrm{u}}} - \pi D$ (eq. 5.8) the DM interaction can be determined from equation 5.11 as

$$D = \frac{4}{\pi}\sqrt{AK_{\mathrm{u}}} - \mu_0 M_{\mathrm{s}}^2 \frac{d}{\pi^2} \ln\left(\frac{2\sqrt{e}}{\pi d} L_{\mathrm{eq}}\right). \tag{5.12}$$

The measured domain pattern which is most reminiscent of a stripe domain pattern is that obtained after demagnetization with an in-plane field. For an average horizontal domain size of $L_{\mathrm{eq}} = (246 \pm 40)\,\mathrm{nm}$ and a sample thickness of $5d_{\mathrm{Co}} = 3.0\,\mathrm{nm}$ for the Co layers with asymmetric interfaces, equation 5.12 yields an interfacial DM interaction of D= $(2.55 \pm 0.03)\,\mathrm{mJ/m^2}$. However, none of the observed domain patterns in figures 5.5 and 5.6 is reminescent of a stripe domain pattern.Moreover equation 5.11 is valid for a sample that is homogeneously magnetized throughout its thickness $d$. This is not the case for the sample here where the magnetic moments are confined in the Co layers separated by the Pt and Ir layers that generate the interfacial DM interaction.

The description of the total magnetic energy leading to equation 5.11 is thus not justified.

In order to overcome these problems we here develop a novel method that does not rely on a simple model domain structure, but uses the measured one, and numerically calculates the magnetostatic energy of multilayer film systems: The total magnetic energy density per unit film area is calculated as the sum of magnetostatic areal energy density and domain wall areal density (cf. eq. 5.9) for a chosen values of D for several assumed image sizes Λ in a range from 3.6 µm to 8.8 µm using the experimental domain pattern measured over a $5\,\mu\mathrm{m} \times 5\,\mu\mathrm{m}$ area (Figs. 5.5 and 5.6). From this, a set of curves describing the dependence of the total magnetic energy density per unit film area on the assumed image size Λ is obtained. Since the shape of the domain wall is independent from the DM interaction $D$[52] the domain wall width of $\delta_{\mathrm{dw}} = \pi\sqrt{A/K_{\mathrm{eff}}} = 32.8\,\mathrm{nm}$ is valid for all values of $D$.

In order to obtain the total energy density of the sample the contributions of the domain walls and magnetostatics have to be considered specifically for the multilayer system studied here. For the sample ASI the energy density contribution of the domain walls in equation 5.9 is

$$\begin{aligned} e_{\mathrm{dw}} &= \frac{1}{A_{\mathrm{sample}} \cdot 6d_{\mathrm{Co}}} \left( \underbrace{d_{Co} \cdot l_{\mathrm{dw}} \sigma_{\mathrm{dw}}^{\mathrm{s}}}_{\text{layer 1}} + \underbrace{5d_{\mathrm{Co}} \cdot l_{\mathrm{dw}} \sigma_{\mathrm{dw}}^{\mathrm{as}}}_{\text{layers 2-6}} \right) \\ &= \frac{l_{dw}}{6A_{\mathrm{sample}}} \left(5\sigma_{\mathrm{dw}}^{\mathrm{as}} + \sigma_{\mathrm{dw}}^{\mathrm{s}}\right), \end{aligned} \tag{5.13}$$

where $d_{\mathrm{Co}} = 0.6\,\mathrm{nm}$ is the thickness of the Co layers, $l_{dw}$ is the total length of the domain wall in the sample area $A_{\mathrm{sample}}$. The areal energy density of the domain walls is $\sigma_{dw}^{\mathrm{s}} = \sqrt{AK_{\mathrm{u}}}$ for the walls in the Co layer with symmetric interfaces and $\sigma_{dw}^{\mathrm{as}} = \sqrt{AK_{\mathrm{u}}} - \pi D$ in the five Co layers with asymmetric interfaces. Note that the magnetostatic energy contribution to the wall energy is already contained in the calculation of the total magnetostatic energy of the sample. The magnetostatic energy density of the sample ASI includes the magnetic energy density of the layers and the density of the inter-layer coupling energy. The coupling energy density for a selected layer of the stack is given by the interaction of its magnetic moments with the stray fields emanating from all other layers. The average magnetostatic energy density is

$$\begin{aligned} e_{\mathrm{ms}} &= -\frac{1}{A_{\mathrm{sample}} \cdot 6d_{\mathrm{Co}}} \frac{1}{2}\mu_0 \\ &\quad \cdot \int_{A_{\mathrm{sample}}} \left( 6d_{\mathrm{Co}} M_{\mathrm{s}} H_{\mathrm{d}} + \sum_{n=1}^{5} n \cdot d_{\mathrm{Co}} M_{\mathrm{z}}(\mathbf{r}) \cdot H_{\mathrm{z}}(\mathbf{r}, d_{\mathrm{n}}^{\mathrm{il}} + \frac{1}{2} d_{\mathrm{Co}}) \right) d\mathbf{r} \qquad (5.14) \\ &= \frac{1}{6A_{\mathrm{sample}}} \frac{1}{2}\mu_0 \int_{A_{\mathrm{sample}}} \left( 6M_{\mathrm{s}} H_{\mathrm{d}} + \sum_{n=1}^{5} n \cdot M_{\mathrm{z}}(\mathbf{r}) \cdot H_{\mathrm{z}}(\mathbf{r}, d_{\mathrm{n}}^{\mathrm{il}} + \frac{1}{2} d_{\mathrm{Co}}) \right) d\mathbf{r}, \end{aligned}$$

where the minus sign arises from the fact that the interaction between layers lowers the total magnetostatic energy density of the system. The $d_\mathrm{n}^\mathrm{il}$ are the inter-layer distances:

$$\begin{aligned}
d_1^\mathrm{il} &= & 5d_\mathrm{Pt} + 5d_\mathrm{Ir} + 4d_\mathrm{Co} &= & 12.4\,\mathrm{nm} \\
d_2^\mathrm{il} &= & 4d_\mathrm{Pt} + 4d_\mathrm{Ir} + 3d_\mathrm{Co} &= & 9.8\,\mathrm{nm} \\
d_3^\mathrm{il} &= & 3d_\mathrm{Pt} + 3d_\mathrm{Ir} + 2d_\mathrm{Co} &= & 7.2\,\mathrm{nm} \\
d_4^\mathrm{il} &= & 2d_\mathrm{Pt} + 2d_\mathrm{Ir} + d_\mathrm{Co} &= & 4.6\,\mathrm{nm} \\
d_5^\mathrm{il} &= & d_\mathrm{Pt} + d_\mathrm{Ir} &= & 2.0\,\mathrm{nm}
\end{aligned}$$

The additional distance of $\frac{1}{2}d_\mathrm{Co}$ in equation 5.15 is required to obtain the stray fields in the middle of the Co layers. Plots of the total energy density $e_\mathrm{tot}$ as a function of the virtual image size $\Lambda$, and for different values of $D$ and different states of the sample ASI are shown in figures 5.5 and 5.6.

All of these curves show one minimum. Its position $\Lambda_\mathrm{min}$ depends strongly on the choice of $D$. The DM interaction of the sample ASI, then is the $D$-value that generates an energy minimum located at the measured image size of $5\,\mu$m. The deviation of D-values from domain patterns obtained after different demagnetization processes (figures 5.5 and 5.6) is small. We find an average value of:

$$D_\mathrm{avg} = (2.04 \pm 0.04)\,\mathrm{mJ/m^2}.$$

This DM interaction is not sufficient to give rise to a negative domain wall energy since $D_\mathrm{avg} < D_\mathrm{crit} := \frac{4}{\pi}\sqrt{AK_\mathrm{u}} = 3.28\,\mathrm{mJ/m^2}$.

(a) as grown, D=2.09 mJ/m$^2$

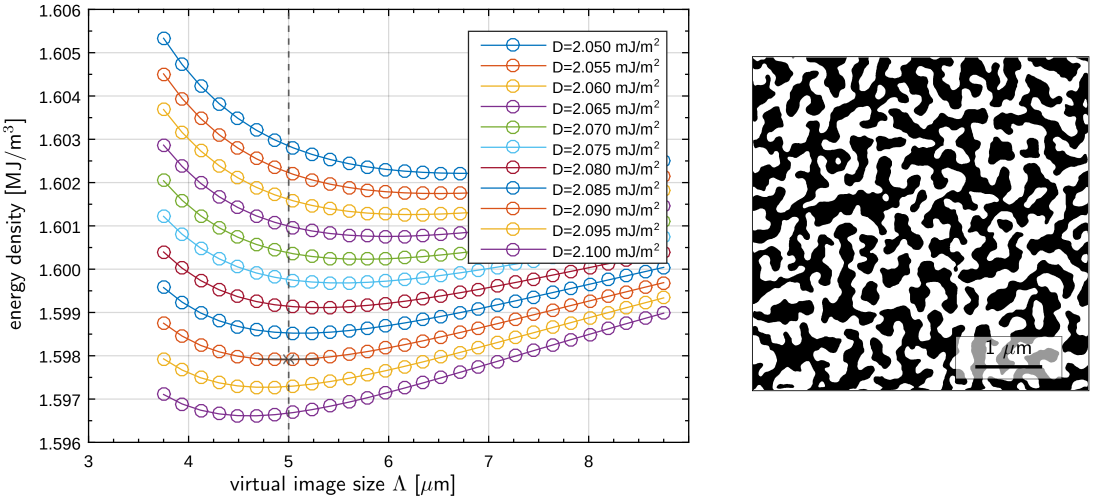

(b) sample demagnetized perpendicular, D=2.00 mJ/m$^2$

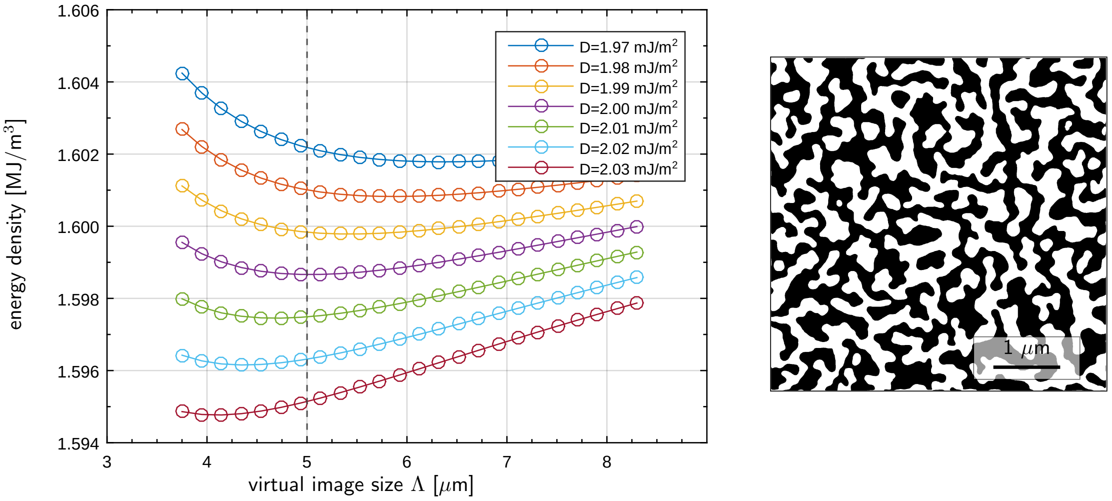

Figure 5.5: The plots on the left show the magnetic energy density of the sample as a function of the assumed image size $\Lambda$. (a): Energy density and domain pattern of sample ASI in the as grown state; (b): after demagnetization with a perpendicular field.

(a) sample demagnetized in-plane, D=2.005 mJ/m$^2$

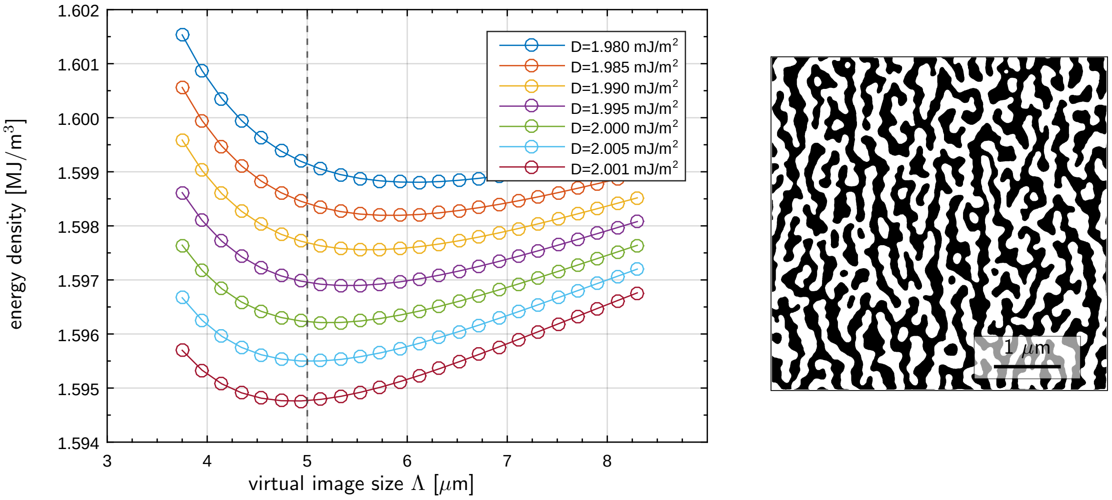

(b) sample at coercive field, D≈2.065 mJ/m$^2$

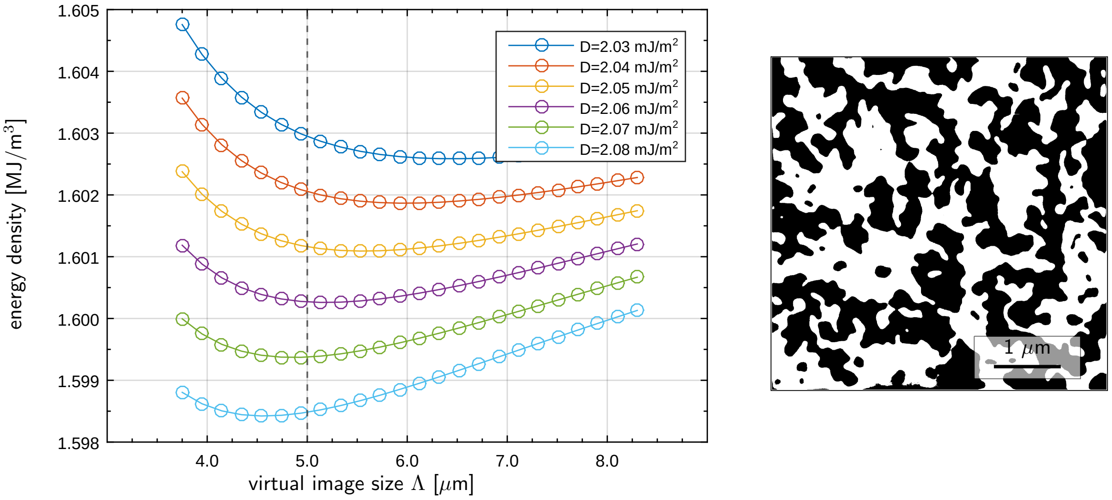

Figure 5.6: The plots on the left show the magnetic energy density of the sample as a function of the assumed image size $\Lambda$. (a): Energy density and domain pattern of sample ASI after demagnetization with an in-plane field; (b): at the coercive field after saturation.

## 5.6 Quantitative MFM Measurements

All MFM measurements presented in this chapter were carried out with the modified hr-MFM described in section 2.1 using a first mode oscillation amplitude $A_1$ of 5 nm. The capacitive distance feedback method introduced in chapter 4 with slow feedback parameters was used to keep an average tip sample distance $d_{\mathrm{ts}}$ of 12 nm. During a measurement series the sensitivity of the deflection sensor can be effected by drift of the beam deflection system or the quality factor of the second resonace mode may change. Then the measured second mode amplitude $A_2$ and thus the tip-sample distance will change. To avoid changes of the tip-sample distance the $A_2$-setpoint that is required to keep $d_{\mathrm{ts}}$=12 nm was determined from $\Delta f_1$- and $A_2$ versus tip-sample distance curves, acquired between the acquisition of successive $\Delta f_1$ images.

### 5.6.1 Tip transfer function $TF$

In order to determine the $TF$, a thin film sample with perpendicular anisotropy, sharp domain walls and a domains size similar to the sample of interest for a later quantitative analysis is required. Sharp domain walls are necessary to have magnetization structures with a short spatial wavelength, while a domain size similar to that of the sample of interest are needed to determine the MFM tip's response at the relevant spatial wavelengths.

The domain wall width of the sample SI can be determined from the measured effective anisotropy $K_{\mathrm{eff}}$ and the exchange stiffness $A$=16 pJ/m taken from the literature[52] as $\delta_{\mathrm{dw}} = \pi\sqrt{A/K_{\mathrm{eff}}}) = 18\,\mathrm{nm}$. A section of the magnetization pattern $M_{\mathrm{z}}(\mathbf{r})$ through a domain with a domain wall width for the sample SI of $\delta_{\mathrm{dw}} = 18\,\mathrm{nm}$ is depicted in figure 5.7(a). The stray field gradient above the sample is the superposition of the stray field gradients of the five individual cobalt layers as illustrated in figure 5.7(b).

The domain size of the as-grown sample is several microns (c.f. figure 5.2), and the calculated equilibrium domain size is around 1 mm – hence orders of magnitude larger than the film thickness. The dependence of the total magnetic energy density on the domains size is very flat, such that the equilibrium domain

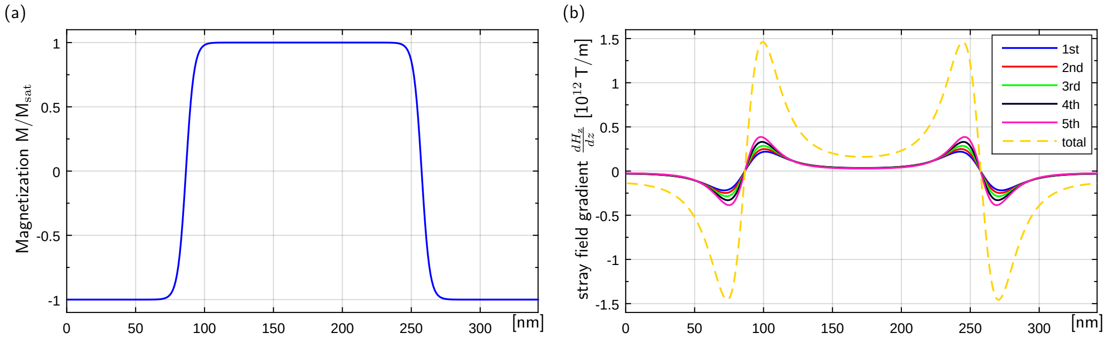

Figure 5.7: (a): Profile of the magnetization pattern $M_{\mathrm{z}}(\mathbf{r})$ across a domain calculated for the sample SI; (b): Section of the stray field gradients $\frac{dH_{\mathrm{z}}}{dz}$ of the five individual Co layers of the sample SI and the total stray field gradient (superposition); the gradients are calculated at a distance of 12 nm above the sample surface.

size ($\approx$ 1 mm) can not be obtained by demagnetizing the sample: We find that different demagnetization processes lead to very different domain sizes, varying from microns to a few hundred of nanometers. The latter is obtained if an in-plane oscillatory field is used for demagnetization as depicted in figure 5.8(a). The obtained domain size is a few hundred nanometers and hence of the same order of magnitude than that of the sample ASI.

## Background subtraction

The MFM image of the sample SI (figure 5.9(a) ) shows the expected up/down domain contrast and an additional granular background pattern. The latter is not measurement noise, because the same pattern is observed in successive measurements and it is also present in MFM data acquired in the saturated state (figure 5.9(b) ). Such a background contrast can either arise from a locally varying van der Waals interaction or a local variation of the magnetic moment of the Co layers. The latter can be caused by a corresponding variation of the film thickness. A contrast induced by van der Waals interaction is independent from the sample's magnetization and can thus be removed from measured MFM data by a subtraction of the data measured with the sample in its saturated state. Note that a saturated magnetic thin film with a homogeneous magnetization does not generate a stray field, such that a remaining contrast arises from a local variation

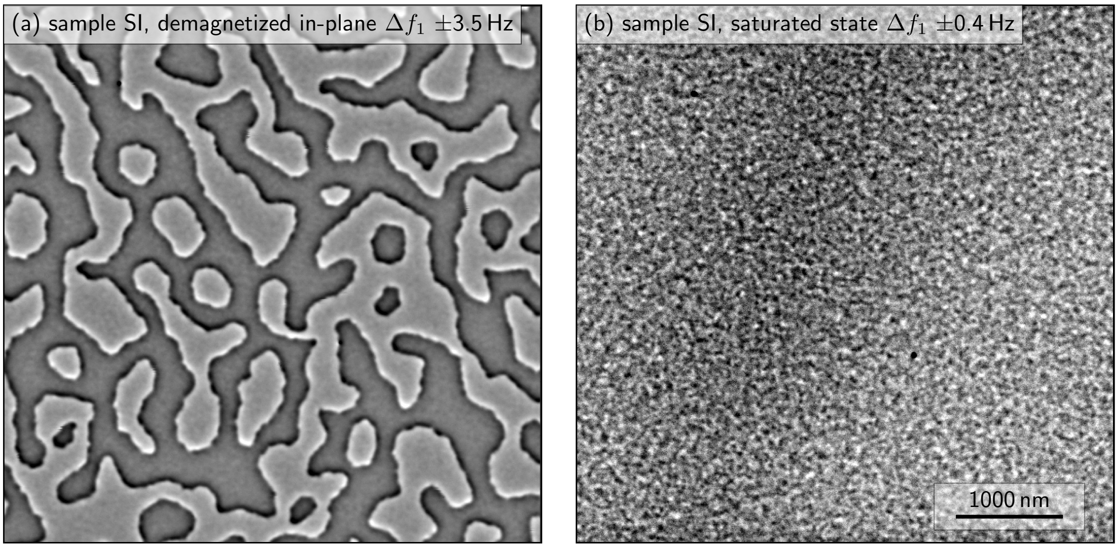

Figure 5.8: The depicted $\Delta f_1$ data is used to determine the $TF$ for the presented quantitative MFM measurements. Panel (a) shows the $\Delta f_1$ data acquired on the sample SI in the in-plane demagnetized state, and panel (b) the $\Delta f_1$ data for the sample SI in its saturated state.

of the van der Waals force. The result of this subtraction $\Delta f_1 - \Delta f_1^{\mathrm{sat}}$ is depicted in figure 5.9(c). The granular background contrast indeed disappears inside the black domains, but becomes doubled inside the white domains. For the sum of the data $\Delta f_1 + \Delta f_1^{\mathrm{sat}}$ in figure 5.9(e) the granular contrast is doubled in the area of the black and annihilated in the area of the white domains. Consequently, the granular contrast does not arise from a spatial variation of the van der Waals force but must be of magnetic origin because it depends on the direction of the (local) domain magnetization. The contrast in $\Delta f_1^{\mathrm{sat}}$ thus arises from an in-homogeneous magnetic moment distribution inside the sample.

For the tip calibration procedure, it is necessary to remove this granular background contrast from the measured frequency shift image. If this was not done, the granular background pattern would be convoluted into the tip-transfer function extracted from the measured $\Delta f_1$ pattern and a stray-field derivative pattern obtained from an estimated magnetization pattern with a homogenuous up/down magnetization of $\pm M_{\mathrm{sat}}$ determined from magnetometry (see section 1.3). Figure 5.9(f) depicts the multiplication of the frequency shift data in saturation $\Delta f_1^{\mathrm{sat}}$ with the negative normalized magnetization pattern $-M_{\mathrm{z}}(\mathbf{r})/M_{\mathrm{sat}}$. Subtracting this result from $\Delta f_1$ yields the $\Delta f_1^{\mathrm{subtr}}$-pattern without the background depicted in figure 5.9(g) which is used for the determination of the $TF$.

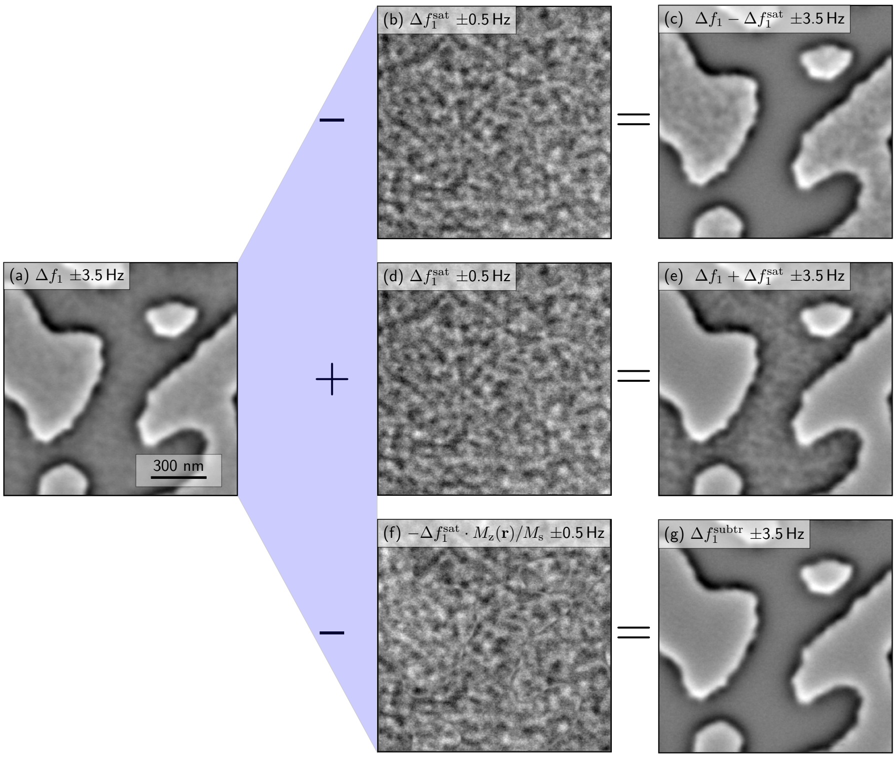

Figure 5.9: (a): measured frequency shift $\Delta f_1$ acquired on the demagnetized sample. The contrast is dominated by the up/down domain contrast, but a weak granular background is also visible. (b): Frequency shift $\Delta f_1$ measured on the saturated sample; (c): Difference of (a) and (b), the background granularity disappears only in the areas of the black domains; (d): same as panel (b) (e): Sum of (a) and (d), the background granularity disappears only in the area of the white domains; (f): background contrast (from panel (b) ) with the negative normalized magnetization pattern $-M_z(\mathbf{r})/M_{\mathrm{sat}}$; (g): Difference of (a) and (f), no granularity is visible.

### Tikhonov Parameter

The determination of the $TF$ from the measured frequency shift data $\Delta f_1$ [1] and the simulated effective stray field gradient of the calibration sample following the methods described in section 1.3 as

$$TF(\mathbf{k}) := \Delta \hat{f}^{\text{subtr}}_{1,\text{meas}}(\mathbf{k}) \cdot \left( \frac{d\hat{H}^{\text{A}_1}_{\text{n}}(\mathbf{k}, z)}{dn}\bigg|_{\text{eff}} \right)^{-1} \tag{5.15}$$

is an ill-posed problem and requires a regularization[60]. Here the Tikhonov method[61,62,60] is used. The problem in equation 5.16 becomes

$$TF(\mathbf{k}) \approx \Delta \hat{f}^{\text{subtr}}_{1,\text{meas}}(\mathbf{k}) \cdot \left( \frac{d\hat{H}^{\text{A}_1}_{\text{n}}(\mathbf{k}, z)}{dn}\bigg|_{\text{eff}} + \delta \cdot \frac{\frac{d\hat{H}^{\text{A}_1}_{\text{n}}(\mathbf{k},z)}{dn}\Big|_{\text{eff}}}{\left|\frac{d\hat{H}^{\text{A}_1}_{\text{n}}(\mathbf{k},z)}{dn}\Big|_{\text{eff}}\right|^2} \right)^{-1} . \tag{5.16}$$

Because the measured frequency shift signal decays rapidly with higher spatial frequencies of the magnetization pattern, the noise limit of the measurement determines the smallest spatial wavelength, for which the $TF$ can be determined. The Tikhonov parameter $\delta$ limits the minimum size of the factor in brackets of equation 5.16 and therefore defines a cutoff at small wavelengths. The dependence of the (circularly averaged) $TF$ on the Tikhonov parameter $\delta$ is illustrated in figure 5.10. Higher values of $\delta$ lead to a smoother tip transfer function, but to reduced $TF$ amplitudes at higher spatial frequencies $k$. Smaller values of $\delta$ increase the value of $TF$ at all frequencies but also generate more noise, particularly at high spacial frequencies $k$, i.e. smaller wavelengths. A good approach to find the best Tikhonov parameter is to study the dependence of the size of the transfer function on the Tikhonov parameter at smaller spatial wavelengths close to the minimally measurable wavelength $\lambda_{\text{min}}$. The best choice for the Tikhonov parameter $\delta$ is the highest value that does not have a significant influence on $TF$ in the range of $\lambda > \lambda_{min}$. In this way numerical noise is suppressed and the resulting $TF$ describes the MFM contrast formation correctly for $\lambda > \lambda_{\text{min}}$. For the data presented here, we found that an optimal $TF$ with $\lambda_{\text{min}}$=30 nm is obtained with a

---

[1] Note that properties without hat are in direct space, i.e. $\Delta f_1(x, y)$, while hat properties, like $\Delta\hat{f}(\mathbf{k})$ are in Fourier space.

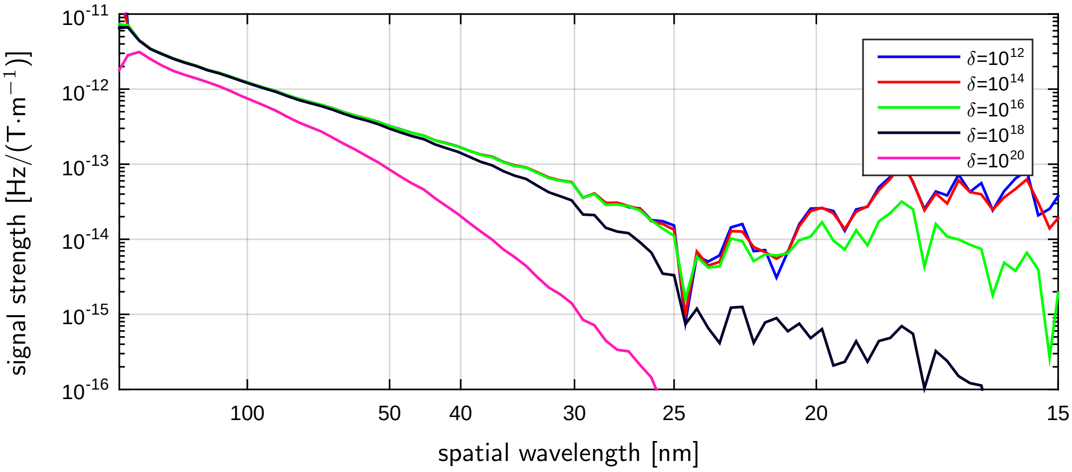

Figure 5.10: The plots illustrate the k-dependence of the tip transfer function for different Tikhonov parameters $\delta$. The average of all pixels with $k = \sqrt{k_\mathrm{x}^2 + k_\mathrm{y}^2}$ i.e., the circular average in Fourier space is plotted.

Tikhonov parameter of $\delta = 10^{16}$.

### Averaging process

We obtain an improved estimate for the $TF$ by averaging the $TF$s determined from 2601 different 1.25 $\mu$m × 1.25 $\mu$m subimages extracted from of the 5 $\mu$m × 5 $\mu$m data depicted in figure 5.8. The size of these subimages is chosen to match that of the $\Delta f_1$ data presented in section 5.8 which have a size of 1250 nm × 1250 nm and a resolution of 256×256 pixels. The background subtraction in figure 5.9 is illustrated for one of these subimages. An additional circular averaging of the $TF$ in Fourier space over all pixels with $k = \sqrt{k_\mathrm{x}^2 + k_\mathrm{y}^2}$ reduces artifacts in the simulated frequency shift data.

## 5.7 Sample ASI – an overview

### 5.7.1 Magnetization behavior

In a first measurement series the nature of the magnetization process of the sample ASI was studied. The decanted and aligned frequency shift data $\Delta f_1/LCF$ are depicted in figure 5.11. Note that the magnetization of the tip flipped when we ramped up the external B-field from 15 mT to 20 mT. Images obtained after the tip magnetization has flipped, are shown with an inverted contrast in figure 5.11. This is to keep the same appearance of the up/down domain pattern before and after the flipping of the tip's magnetization. At $B = -250\,\mathrm{mT}$ the sample is saturated. At an external B-field of $B = -1\,\mathrm{mT}$ several small circular domains are visible with a magnetization antiparallel to the external B-field. At $B = +5\,\mathrm{mT}$ the small white domain in the center of the image expands but retains its strong circular curvature at the bottom (see arrow). Two further circular domains appear, indicated by the yellow circles in figure 5.11. With increasing B-field more circular small domains appear and existing ones expand to larger domains. Generally the domains exhibit a strong wall curvature and at many locations expanding domains do not join, but stay separated by narrow domains with negative (black) magnetization. When the white domains coalesce at $B = +42\,\mathrm{mT}$ several circular black domains persist inside the large white ones. Those small reversal domains are still present at higher B-fields before the sample is saturated at $B > 97\,\mathrm{mT}$.

The observed small circular domains occur only in the sample ASI and not in the sample SI. Furthermore such small bubble domains with a diameter smaller than 100 nm are not stable in a sample without DM interaction. We hence conclude that these small bubble domains must be skyrmions stabilized by the DM interaction arising from the asymmetric interfaces of the sample.

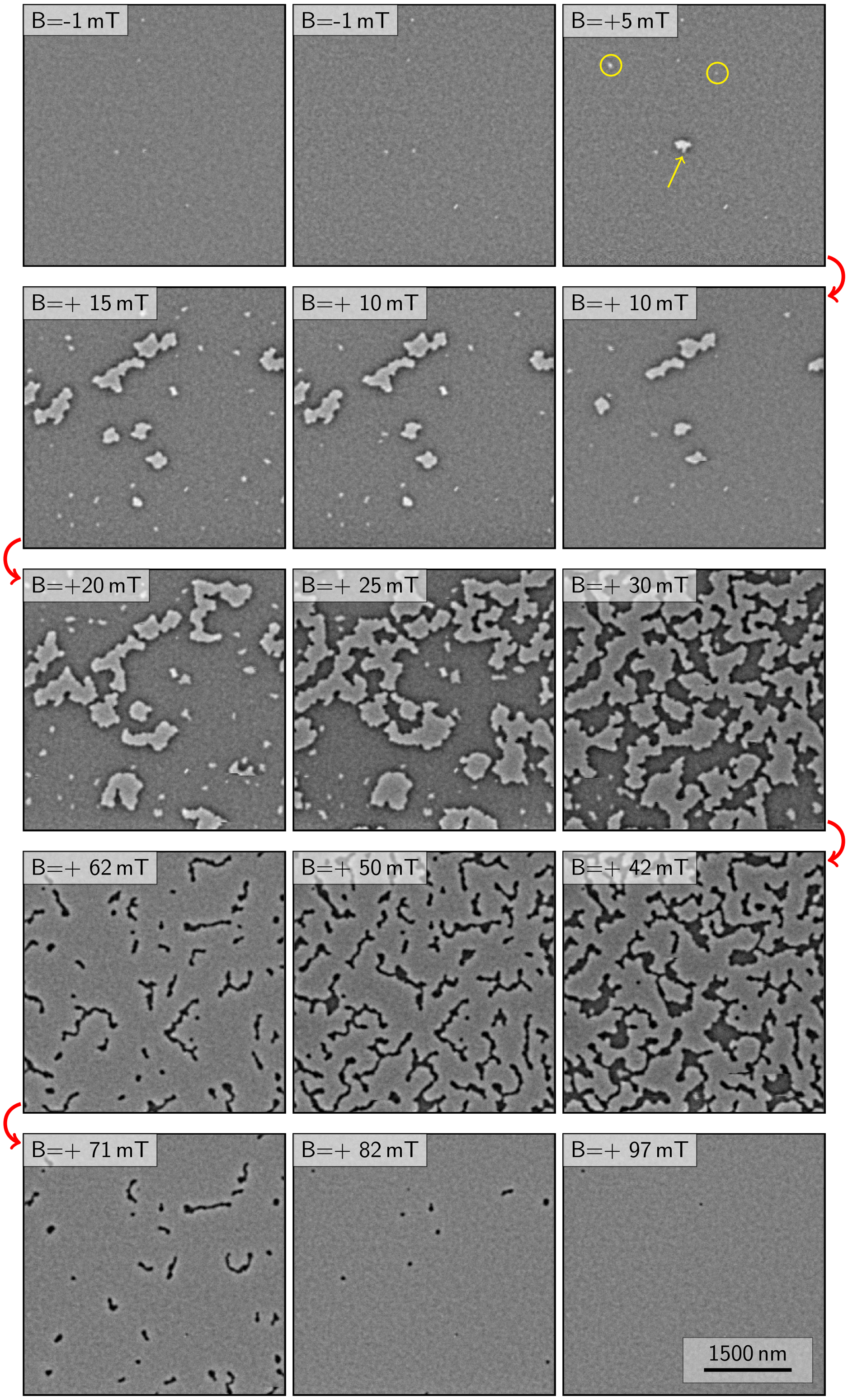

Figure 5.11: Processed frequency shift data $\Delta f_1$ for a B-field series measured on the sample ASI is depicted with a white to black contrast of ±2.5 Hz. The applied processing removed effects of the canted oscillation of the cantilever. Panels with identical B-field values show the data of subsequent measurements.

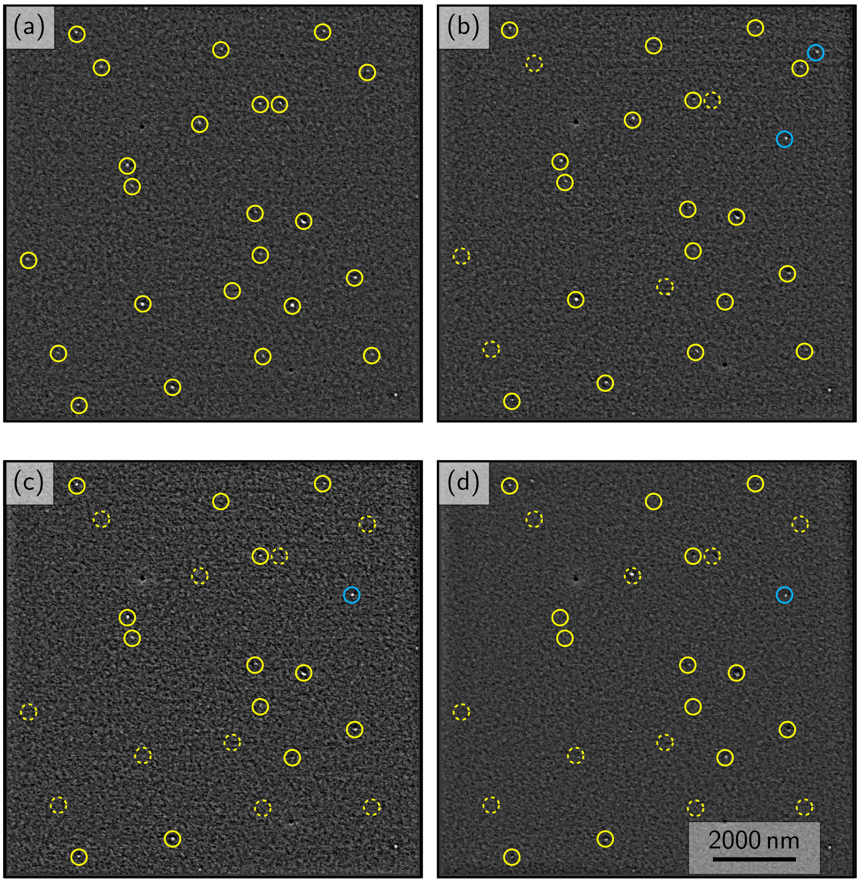

Figure 5.12: Processed $\Delta f_1/LCF$ of the overview scans acquired at $B = -1.1\,\mathrm{mT}$ after repeated negative saturation of the sample. The applied processing removed effects of the canted oscillation of the cantilever. The white to black contrast scale is $\pm 1.4\,\mathrm{Hz}$ for all panels.

## 5.8 Measurements of individual skyrmions

In order to study individual skyrmions, overview scans with an $11\,\mu\mathrm{m}\times 11\,\mu\mathrm{m}$ area were acquired in an external field of $B = -1.1\,\mathrm{mT}$ after a negative saturation of the sample to determine locations where skyrmions appear (cf. fig. 5.12). Afterwards, selected areas were scanned with a pixel resolution of 4.9 nm per pixel. The frequency shift data $\Delta f_1$ of the overview scans are depicted in figure 5.13. The observed skyrmions are marked by the yellow circles in figure 5.13(a). Only a few skyrmions exist in the $11\,\mu\mathrm{m}\times 11\,\mu\mathrm{m}$ area and that they often re-appear at the same location after repeated saturation processes. From this we conclude that the physical properties at these locations must be substantially different from those averaged over the whole film area.

The frequency shift $\Delta f_1$ data of the high resolution MFM scans acquired in different fields are shown in figure 5.13. Data acquired at one location are ordered as a column in figure 5.13. Panels (a), (e) and (i) show the $\Delta f_1$ data obtained at $B = -1.1\,\mathrm{mT}$ after negative saturation of the sample. For this identical initial conditions the maximum $\Delta f_1$ contrast and width of the skyrmions vary considerably. The maximum frequency shift signal in the center of the skyrmions is 1.36 Hz for the upper and 1.03 Hz for the lower skyrmion of group A, whereas it is 2.72 Hz for the skyrmion of group B. Further, the field dependence of the skyrmions for fields applied antiparallel to their core magnetization also shows substantial differences. The lower skyrmion of group A vanishes during the scan in figure 5.13(b) when it is exposed to the stray field of the tip and an externally applied B-field of -2.1 mT. The upper skyrmion of group A remains unchanged in an external B-field of -2.9 mT (fig. 5.13(c) ). Both skyrmions of this group are no longer visible in the scan at $B = -3.5\,\mathrm{mT}$ in fig. 5.13(d). The skyrmion of group B exhibits a much higher stability. Its shape and maximum frequency shift signal in fig. 5.13(f) remain unchanged at an external B-field of -22.2 mT. When ramping down the field to $B = -1.1\,\mathrm{mT}$ it develops an elliptical shape, indicated by the arrow in in fig. 5.13(g). This skyrmion is annihilated in an external field of -26.7 mT. The left skyrmion of group C already vanishes in a B-field of -2.1 mT (see white arrows in panels (i) and (j)). The right skyrmion has a slight elliptical shape at -1.1 mT that develops towards a circular shape at higher negative fields, and disappears above $B = -18.3\,\mathrm{mT}$. Panel (d), (h) and (l) of figure 5.13 show the saturated states.

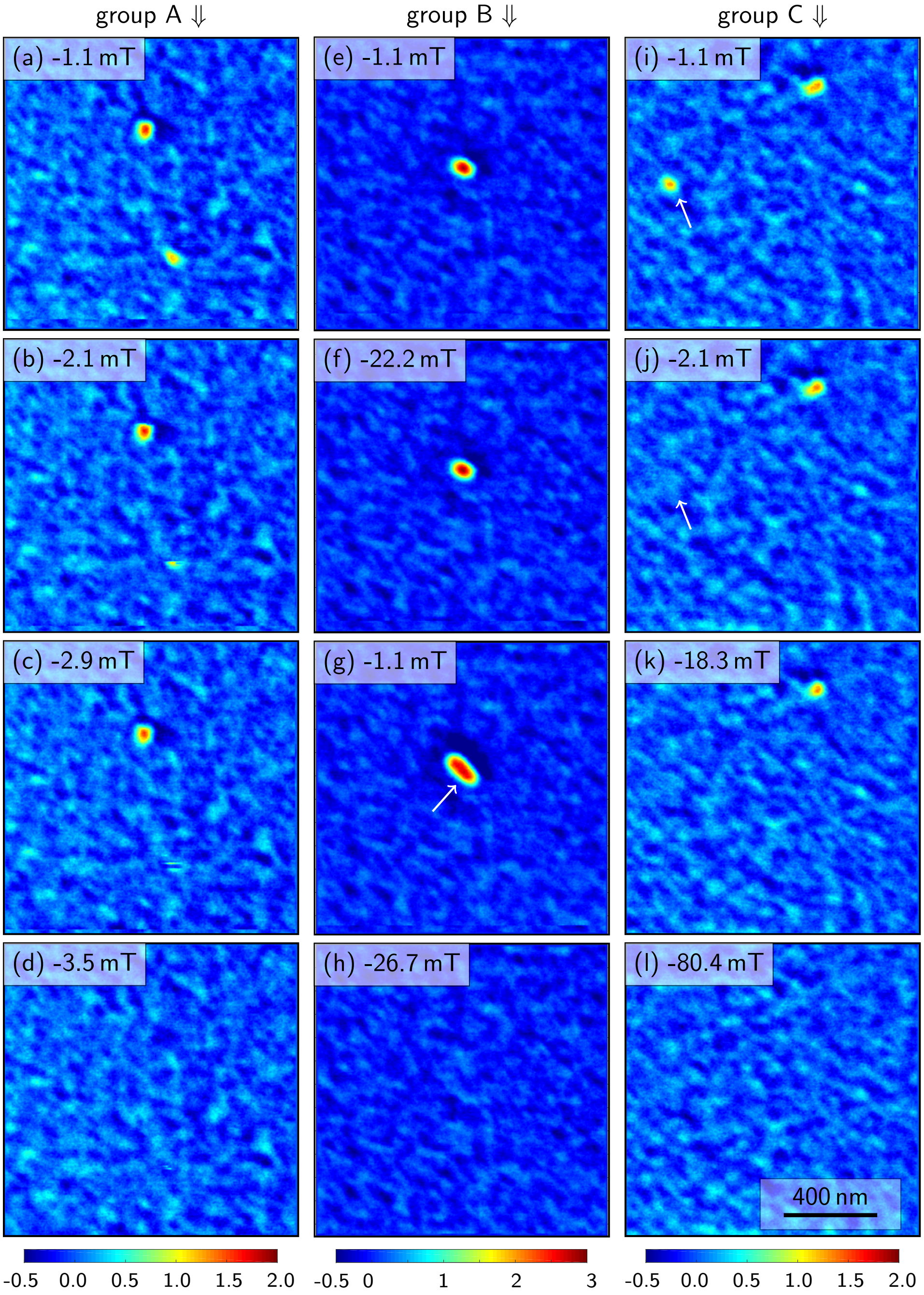

Figure 5.13: High resolution frequency shift data $\Delta f_1$ acquired in different B-fields, and at different locations is illustrated. The color scale in Hz for each group (column) is given at the bottom of the figure.

## 5.9 Quantitative reconstruction of the background

The background signal visible in figure 5.13(d), (h) and (l) arises from a spatial variation of the magnetic moment in the Co layers. This section describes how to reconstruct the variation of the magnetic moment averaged over all six Co layers from the measured $\Delta f_1$ signal. The individual Cobalt layers in the sample ASI are located at the distances $z_0(n)$ from the surface of the sample with $z_0(n) = (n-1)(d_{\mathrm{Co}} + d_{\mathrm{Ir}} + d_{\mathrm{Pt}}) + d_{\mathrm{top}}$ i.e.:

$$\begin{aligned} z_0(1) &= 4\,\mathrm{nm}, \\ z_0(2) &= 6.6\,\mathrm{nm}, \\ z_0(3) &= 9.2\,\mathrm{nm}, \\ z_0(4) &= 11.5\,\mathrm{nm}, \\ z_0(5) &= 13.8\,\mathrm{nm}, \\ z_0(6) &= 16.1\,\mathrm{nm}, \end{aligned}$$

for $d_{\mathrm{Co}} = 0.6\,\mathrm{nm}$, $d_{\mathrm{Ir}} = 1\,\mathrm{nm}$, $d_{\mathrm{Pt}} = 1\,\mathrm{nm}$ and $d_{\mathrm{top}} = 4\,\mathrm{nm}$. For the calculation of the average magnetization variation pattern $\hat{M}_{\mathrm{z}}^{\mathrm{avg}}(\mathbf{k})$, a combined wavelength dependent distance loss factor can be defined as

$$\alpha(\mathbf{k}) = \sum_{n=1}^{6} e^{-k(d_{\mathrm{ts}} + A_1 + z_0(n))}, \tag{5.17}$$

where $d_{\mathrm{ts}} = 12\,\mathrm{nm}$ is the tip-sample distance, and $A_1 = 5\,\mathrm{nm}$ the oscillation amplitude of the cantilever. In Fourier space such a pattern $\hat{M}_{\mathrm{z}}^{\mathrm{avg}}(\mathbf{k})$ is linked to the effective stray field derivative at the distance $d_{\mathrm{ts}} + A_1 = 17\,\mathrm{nm}$ from the sample surface by (see section 1.3)

$$\left.\frac{d\hat{H}_{\mathrm{n}}^{\mathrm{A}_1}(\mathbf{k})}{dn}\right|_{\mathrm{eff}} = \frac{1}{A_1} LCF(\mathbf{k},\eta) I_1(\tilde{z}) \cdot \alpha(\mathbf{k}) \cdot \left(1 - e^{-kd_{\mathrm{Co}}}\right) \hat{M}_{\mathrm{z}}^{\mathrm{avg}}(\mathbf{k}). \tag{5.18}$$

Thus the magnetization pattern $M_{\mathrm{z}}^{\mathrm{avg}}$ can be recovered from the measurements with

$$\hat{M}_{\mathrm{z}}^{\mathrm{avg}}(\mathbf{k}) = \frac{\Delta\hat{f}_{1,\mathrm{meas}}(\mathbf{k})}{TF(\mathbf{k}) \cdot \alpha(\mathbf{k}) \cdot (1 - e^{-kd_{\mathrm{Co}}})} \left(\frac{1}{A_1} LCF(\mathbf{k},\eta) I_1(\tilde{z})\right)^{-1}. \tag{5.19}$$

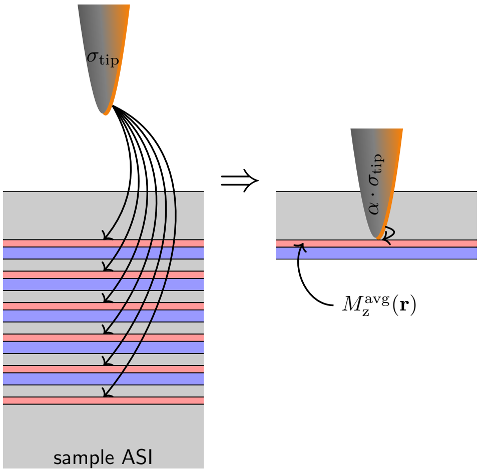

Figure 5.14: Illustration of the interaction of the tip equivalent surface charge $\sigma_{\text{tip}}$ with the individual magnetic layers of the sample ASI and the definition of $M_{\text{z}}^{\text{avg}}$ with the combined distance loss factor $\alpha(\mathbf{k})$

The denominator in equation 5.19 is small for high spacial frequencies $k$. Therefore some regularization procedure must be used. Here this is done by adding a $k$-dependent window function $WF(\mathbf{k})$ to the denominator which limits the amplification at smaller wavelengths with $k > k_{\text{limit}}$. Equation 5.19 then becomes

$$\hat{M}_{\text{z}}^{\text{avg}}(\mathbf{k}) = \frac{\Delta\hat{f}_{1,\text{meas}}(\mathbf{k})}{TF(\mathbf{k}) \cdot \alpha(\mathbf{k}) \cdot (1 - e^{-kd_{\text{Co}}}) + WF(\mathbf{k})} \left(\frac{1}{A_1} LCF(\mathbf{k}, \eta) I_1(\tilde{z})\right)^{-1}, \tag{5.20}$$

with

$$WF(\mathbf{k}) := \exp\left[-\left(\frac{k_{\text{limit}}}{k}\right)^{\nu}\right], \tag{5.21}$$

where $1/k_{\text{limit}}$ is the cutoff wavelength and $\nu$ the steepness of the exponential filter function. The window function takes values between $WF(|\mathbf{k}| \ll k) = 0$ and $WF(|\mathbf{k}| \gg k) = 1$. A steep transition is i.e., obtained for $\nu = 36$. $M_{\text{z}}^{\text{avg}}(\mathbf{k})$ is then recovered only for wavelengths larger than $1/k_{\text{limit}}$. The denominators of equations 5.19 and 5.20 are plotted in figure 5.15 together with the original tip transfer function $TF(\mathbf{k})$.

With equation 5.20 an average magnetization pattern $\hat{M}_{\text{z}}^{\text{avg}}(\mathbf{k})$ can be calculated from the measured frequency shift pattern $\Delta f_{1,\text{meas}}(\mathbf{k})$ for wavelengths $\lambda > 1/k_{\text{limit}} = 50\,\text{nm}$. Hence only magnetization variations with a wavelength larger

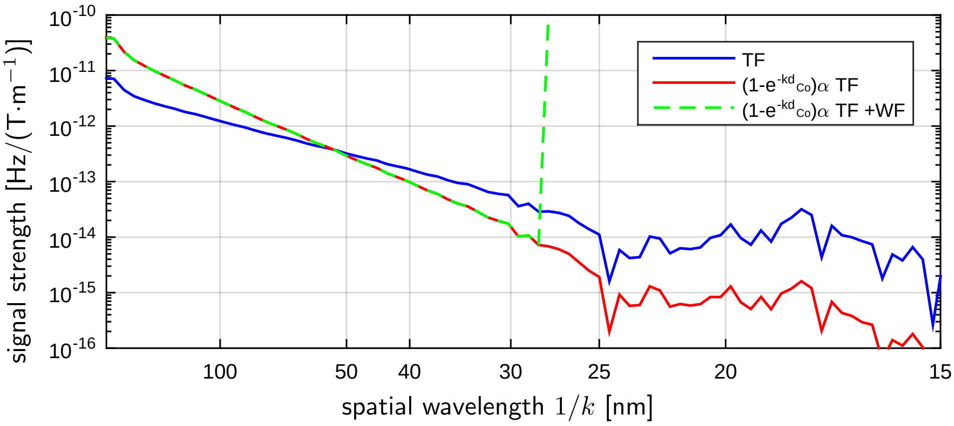

Figure 5.15: The signal strength of the magnetic imaging process is plotted as a function of the spacial wavelength $1/k$. The plot shows the initial transfer function of the tip $TF(\mathbf{k})$ (blue curve), the transfer function multiplied with distance- and thickness-loss factors $(1-e^{-kd_{\text{Co}}})\alpha(\mathbf{k})TF(\mathbf{k})$ for the sample ASI (red curve) and the denominator of equation 5.20 $TF(\mathbf{k})\cdot\alpha(\mathbf{k})\cdot\left(1-e^{-kd_{\text{Co}}}\right)+WF(\mathbf{k})$ with $1/k_{\text{limit}}=26\,\text{nm}$ (dashed, green curve).

than 50 nm can be obtained. Panel 5.16(a) depicts the background magnetization pattern $M_{\mathrm{z}}(\mathbf{r})$ for group A based on the frequency shift data in figure 5.13(d). Panels (d) and (g) show the same for the groups B and C, based on the data in figure 5.13(h) and 5.13(l), respectively. The simulated frequency shift patterns $\Delta f_1^{\mathrm{sim}}$ in figure 5.16(b), (f) and (h) illustrate the expected MFM signals for the respective magnetization patterns $\Delta M_{\mathrm{z}}(\mathbf{r})$. The panels (c), (f) and (i) in the last row of figure 5.16 depict the differences between measured and simulated frequency shifts. From these differences we draw two conclusions: Firstly, $\Delta f_1^{meas} - \Delta f_1^{\mathrm{sim}}$ remain an order of magnitude smaller than the measured frequency shift patterns, which indicates that the determined magnetization patterns are valid estimates. Secondly for all three groups noise and mazelike artifacts are visible in $\Delta f_1^{meas} - \Delta f_1^{\mathrm{sim}}$ which suggest that the signal to noise ratio of the measured frequency shift data is not sufficient to recover $\Delta M_{\mathrm{z}}(\mathbf{r})$ for spacial frequencies with $|\mathbf{k}| > 1/50\,\mathrm{nm}$.

For the recovered variation of the magnetic moment areal density we find a standard deviation of $66\,\mathrm{kA/m} \cdot d_{\mathrm{Co}}$ which corresponds to 10% of $M_{\mathrm{s}} \cdot d_{\mathrm{Co}}$. The peak-to-peak variation in the magnetic moment areal density is approximately $\pm\frac{1}{3} M_{\mathrm{s}} \cdot d_{Co}$. This can be attributed to a variation of the Co layer thickness of 0.2 nm, corresponding to 1.2 atomic layers in each Co layer. Ab initio calculations performed by Yang et al.[57] predict a change of the DM interaction from $2.54\,\mathrm{mJ/m^2}$ for 3 monolayers ($\approx 0.6\,\mathrm{nm}$) to $3.71\,\mathrm{mJ/m^2}$ for 2 monolayers ($\approx 0.4\,\mathrm{nm}$) of Co on Pt.

The variation of the local DMI determined from the MFM measurements of individual skyrmions ($3.19\,\mathrm{mJ/m^2} <= \mathrm{D} <= 3.49\,\mathrm{mJ/m^2}$), described in the following section 5.10, thus is in range of values theoretically predicted for the Co layer thickness variations determined experimentally.

## 5.10 Calculation of the skyrmion magnetization profiles and MFM signals

In section 5.5 the measured domain size was used to determine the average DM interaction in the sample ASI. The obtained value for $D$ is too small to support a skyrmion phase. Nevertheless, a few skyrmions re-appearing at specific loca-

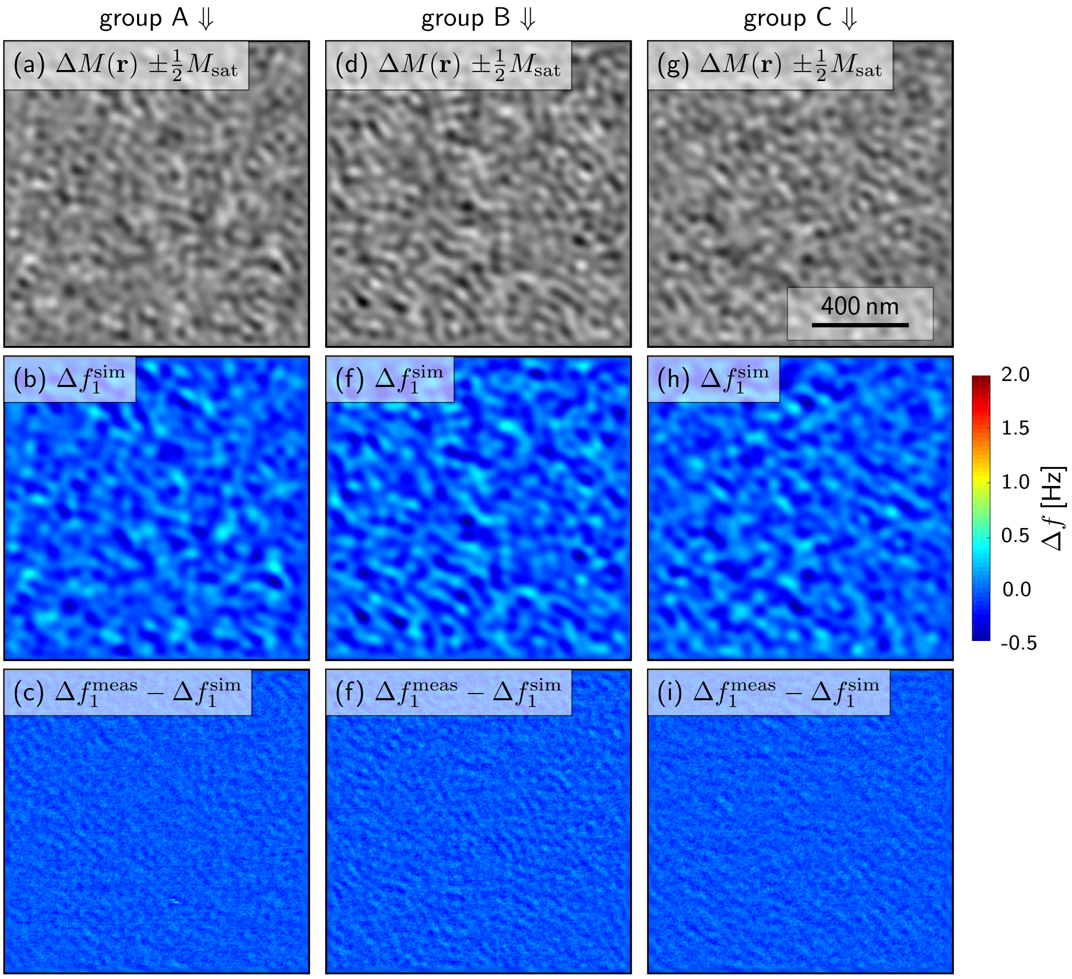

Figure 5.16: Reconstruction of the background magnetization variation of the sample ASI using equation 5.20 with $1/k_{\rm limit} = 50\,$nm. Panels (a), (d) and (g) depict the reconstructed magnetization pattern $\Delta M_{\rm z}(\mathbf{r})$ for the area of the skyrmion groups A, B and C with a white to black contrast scale of $\pm\frac{1}{2}M_{\rm s} = 327\,$kA/m. Panels (b), (f) and (h) illustrate the simulated MFM signal based on the reconstructed magnetization patterns in (a), (d) and (g), respectively. Panels (c), (f) and (i) illustrate the difference between the measured data in saturation (see fig. 5.13) and the simulated frequency shifts from panels (b), (f) and (h). All frequency shift data is displayed with the color scale given on the right.

tions were imaged by MFM (figure 5.12). This and the different contrast of the skyrmions in figure 5.13 indicates that these locations of the films may have a local DM interaction that is substantially different from that determined from the domain size. This section describes the process for obtaining local $D$-values. This is achieved by matching model calculations of the MFM contrast generated by a skyrmion to measured MFM data.

The spin texture of a skyrmion is determined by the energy density

$$W = A\sum_i \left(\frac{\partial \mathbf{m}}{\partial x_i}\right)^2 - Km_\mathrm{z}^2 - \mu_0 \mathbf{M}\cdot\mathbf{H}_\mathrm{ext} - \frac{1}{2}\mu_0\mathbf{M}\cdot\mathbf{H}_\mathrm{d} + w_\mathrm{D}, \tag{5.22}$$

where $A$ is the exchange stiffness, $\mathbf{m} = \mathbf{M}/M_\mathrm{s}$ the normalized magnetisation, K the uniaxial anisotropy, $\mathbf{H}_\mathrm{ext}$ an externally applied field and $\mathbf{H}_\mathrm{d}$ the demagnetizing field. The energy density $w_\mathrm{D}$ is the contribution of the DM interaction. For the case of an interfacially induced DM interaction $w_\mathrm{D}$ is[52]

$$w_\mathrm{D} = -D\left[\left(m_\mathrm{x}\frac{\partial m_\mathrm{z}}{\partial x} - m_\mathrm{z}\frac{\partial m_\mathrm{x}}{\partial x}\right) + \left(m_\mathrm{y}\frac{\partial m_\mathrm{z}}{\partial y} - m_\mathrm{z}\frac{\partial m_\mathrm{y}}{\partial y}\right)\right]. \tag{5.23}$$

With the reduced coordinates defined by Bogdanov and Hubert[63]:

$$\begin{aligned} w &:= \frac{W}{\mu_0 H_\mathrm{D} M_s} \quad \text{and: } H_\mathrm{D} := \frac{D^2}{AK} \\ \tilde{x}_\mathrm{i} &:= x_\mathrm{i}\frac{A}{D} \\ \mathbf{h} &:= \mathbf{H}/H_\mathrm{D} \end{aligned}$$

a reduced energy density $w$ can be defined as:

$$w = \sum_i \left(\frac{\partial \mathbf{m}}{\partial \tilde{x}_\mathrm{i}}\right)^2 - \tilde{\beta} m_\mathrm{z}^2 - \mathbf{m}\cdot\mathbf{h}_\mathrm{ext} - \frac{1}{2}\mathbf{m}\cdot\mathbf{h}_\mathrm{d} + \frac{w_\mathrm{D}}{D}, \tag{5.24}$$

where

$$\tilde{\beta} = \beta(1 + \frac{1}{Q}) \tag{5.25}$$

with $\beta = AK/D^2$, $Q = K/K_d$, and $K_d = \frac{1}{2}\mu_0 M_\mathrm{s}^2$. Using variational energy minimization Bogdanov and Hubert[63] obtained the Euler equation

$$\frac{d^2\theta}{d\rho^2} + \frac{1}{\rho}\frac{d\theta}{d\rho} - \left(\frac{1}{\rho^2} + \tilde{\beta}\right)\sin(\theta)\cos(\theta) + \frac{\sin^2(\theta)}{\rho} - \frac{1}{2}h\sin(\theta) = 0, \tag{5.26}$$

where the normalized magnetization $\mathbf{m}(\tilde{\mathbf{r}})$ is described in spherical coordinates as

$$\mathbf{m} = (\sin(\theta)\cos(\psi), \sin(\theta)\sin(\psi), cos(\theta))$$

and the coordinate vector in cylindrical coordinates as

$$\tilde{\mathbf{r}} = (\rho\cos(\varphi), \rho\cos(\varphi), \tilde{z})\,.$$

The Euler equation 5.26 with boundary conditions $\theta(0) = \pi$ and $\theta(\infty) = 0$ defines the skyrmion spin texture. Note that equation 5.26 is a two-dimensional description of the skyrmion profile, i.e. equation 5.26 describes skyrmions that are uniform along the z-direction. For calculations of the spin texture, it is typically assumed that the demagnetization field is locally defined as $\mathbf{h}_\mathrm{d} = -\mathbf{m}$. In reality the demagnetization field deviates from this approximation, and depends on the thickness of the sample and the explicit local magnetization structure. Hence, to describe the skyrmions in the sample ASI with the two dimensional equations 5.22 and 5.26, the magnetostatic energy term $\frac{1}{2}\mathbf{m}\cdot\mathbf{h}_\mathrm{d}$ and also $\tilde{\beta}$ (equation 5.25) need to be adapted. For this we use a scaled magnetization $M_s \to \alpha M_\mathrm{s}$ with $\alpha < 1$ to match a total magnetostatic energy density calculated as $\frac{1}{2}\alpha\cdot\mathbf{m}\cdot\mathbf{h}_\mathrm{d}$ (eq. 5.23) to a magnetostatic energy density calculated numerically for the layered structure of the sample ASI. The energy density can be obtained similar to equation 5.15 as

$$\begin{aligned} e_\mathrm{ms} \;=\; & -\frac{1}{d_\mathrm{Co}A_\mathrm{sample}}\frac{1}{2}\mu_0 \qquad (5.27)\\ & \cdot\int_{d_\mathrm{Co}}\int_{A_\mathrm{sample}}\left(M_\mathrm{s}H_\mathrm{d}(\mathbf{r},z) + \frac{1}{5}\sum_{n=1}^{4} n\cdot M_\mathrm{sk}(\mathbf{r})\cdot H_\mathrm{z}(\mathbf{r}, d_\mathrm{n}^\mathrm{il} + z)\right)d\mathbf{r}dz, \end{aligned}$$

with the interlayer distances $d_\mathrm{n}^\mathrm{il}$ described in section 5.5 for the skyrmion present in the 5 Co layers with DM interaction. The demagnetization field $H_\mathrm{d}(\mathbf{r}, z)$ and

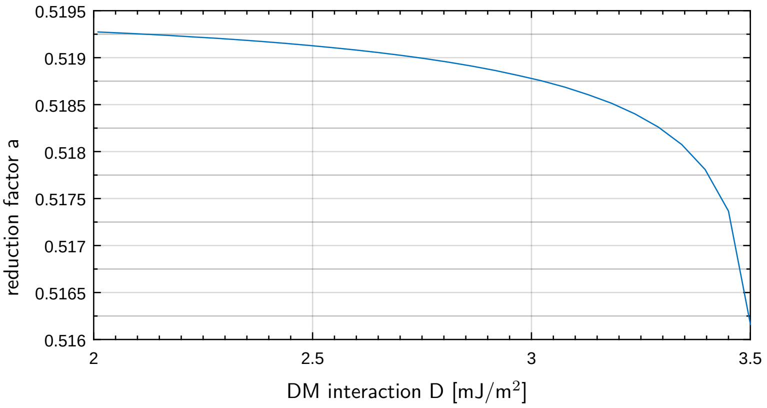

Figure 5.17: Scaling factor $a$ for $M$ in equation 5.22 as a function of the DM interaction $D$.

the stray field $H_\mathrm{z}(\mathbf{r}, d_\mathrm{n}^\mathrm{il} + z)$ are again numerically calculated. The magnetization pattern

$$M_\mathrm{sk}(\mathbf{r}) = M_\mathrm{s} \cdot \cos\left(\theta(\mathbf{r})\right) \tag{5.28}$$

is obtained by solving the Euler equation 5.26 using the scaled magnetization $\alpha M_\mathrm{s}$. The reduction factor $\alpha$ must be chosen such that the magnetostatic energy density

$$e_\mathrm{ms} = \frac{1}{2}\mu_0(\alpha M_\mathrm{s})^2 \tag{5.29}$$

calculated in the local approximation matches that calculated numerically with the expression 5.28 for the layer structure of the sample. Because the skyrmion profile is a priori unknown, an initial scaling factor $\alpha = 0.52$ is used to calculate the magnetostatic energy as given in equation 5.28 and to find an improved alpha with equation 5.29. This process is repeated until self-consistency is reached, which is the case after two calculation cycles. Figure 5.17 shows the dependence of $\alpha$ on the DM interaction $D$[2].

Using the scaled magnetization with the factor alpha given in figure 5.17 the skyrmion spin texture can be calculated by solving equation 5.22 numerically.

---

[2] It is noteworthy that the stray field of skyrmions arises from magnetic surface charges, but also from magnetic volume charges from the skyrmion Néel type wall profiles. In this thesis the contributions of the latter have been neglected. For this reason the obtained D values, and skyrmion profiles differ from those of an upcoming publication[64].

Solutions for different DM interactions are plotted in figure 5.18. Note that the skyrmion magnetization profiles are different from those of conventional bubble domains. The latter have a constant magnetization at and near the center of the domain, which is not the case for skyrmions. Their magnetization reaches a perpendicular orientation only at the center and immediately rotates away from the vertical direction with increasing distance from the center. Higher DM interaction values lead to wider skyrmions, because the wall energy becomes smaller, but the vertical component of the magnetization still drops off away from the center.

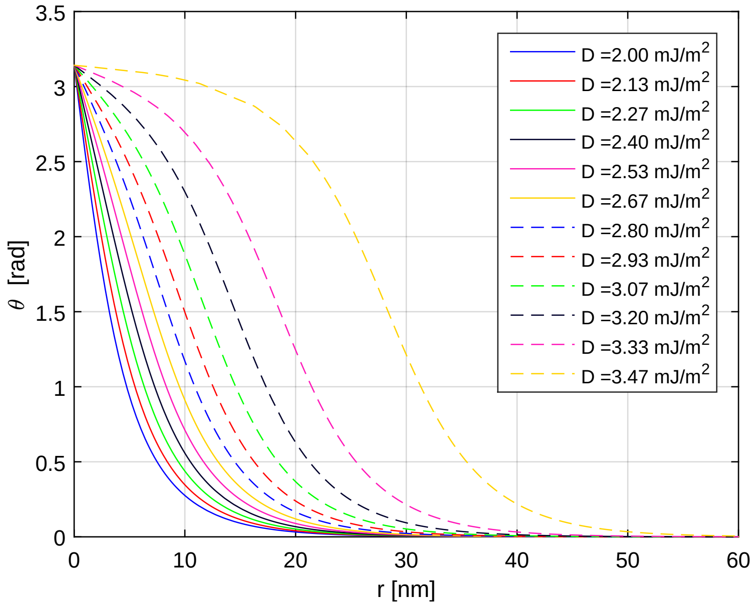

Figure 5.18: Angle $\theta$ of the magnetic moments of a skyrmion as a function of the radial position r with different DM interaction $D$.

From the skyrmion magnetization structure the corresponding stray field and MFM contrast can be calculated using the quantitative MFM methods described in section 1.3. Figure 5.19 shows the cross sections along the $x$-direction of MFM for skyrmions with different $D$-values. A skyrmion with a DM interaction of $D = 2.00\,\mathrm{mJ/m^2}$ which is close to $D_{\mathrm{avg}} = 2.04\,\mathrm{mJ/m^2}$ obtained from the domain size analysis, generates an MFM contrast of only 0.2 Hz. This is much smaller than the typical contrast observed at the center of the skyrmions (ranging from 1 Hz to 2.6 Hz) shown in figure 5.13, and also smaller than the background signal arising from the variation of the Co layer thickness (see section 5.9). In order to exclude the existance of skymrions with such low $D$ values, the background contrast obtained in a field of 1mT is compared to that obtained in fields of 30 mT and 80 mT. No difference of the background images is found. Consequently, skyrmions with a $D \approx 2.00\,\mathrm{mJ/m^2}$ do not exist. For larger $D$-values, skyrmions with a larger diameter and hence a stronger MFM contrast are found. The comparison of the MFM contrast obtained at the skyrmion center for different $D$-values (figure 5.19) with the experimentally observed contrast in figure 5.20 reveals that the local D values at the locations of the skyrmions must be between $D = 3.06\,\mathrm{mJ/m^2}$ and $D = 3.48\,\mathrm{mJ/m^2}$, i.e. considerably larger than the average $D$-value of the film.

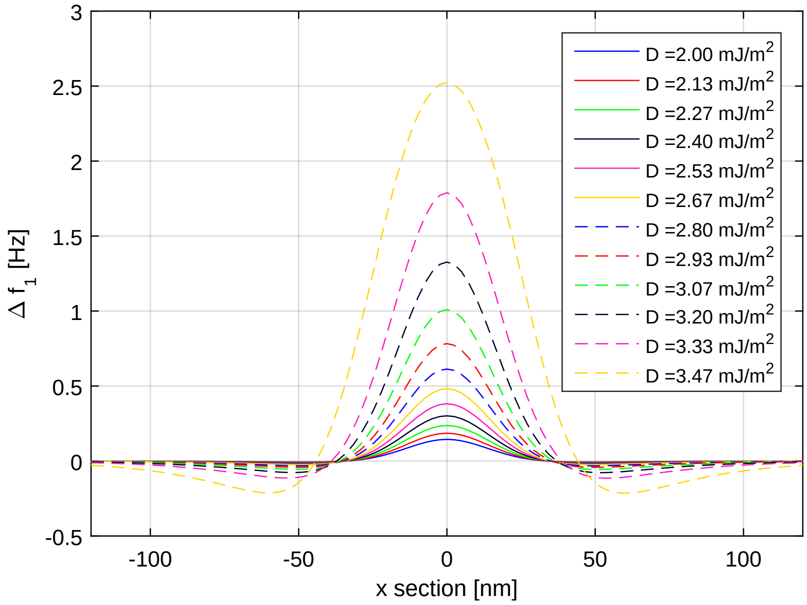

Figure 5.19: Section along the x-direction of simulated frequency shift data $\Delta f_1$ for skyrmions with different DM interaction in the sample ASI.

A comparison of the simulated and measured frequency shift data for the skyrmions of the groups A and B is shown in figure 5.20. In order to compare the experimental and the model data directly, it is useful to subtract the background variation obtained in saturation (fig: 5.20(b) ) from the data showing the skyrmions in fig. 5.20(a). The resulting $\Delta f_1^{\mathrm{subtr}}$-data are shown in figure 5.20(c). Figure 5.20(d) shows the simulated $\Delta f_1$ data for DM interactions of $D = 3.19\,\mathrm{mJ/m^2}$ and $D = 3.06\,\mathrm{mJ/m^2}$ for the upper and lower skyrmion of group A and $D = 3.48\,\mathrm{mJ/m^2}$ for the skyrmion of group B.

The $D$-values are adjusted to match the observed experimental contrast at the center of the skyrmion. Consequently, the calculated cross-section will match those obtained from the experimental data at the center of the skyrmion (figure 5.21), but not necessarily away from center. Indeed the simulated skyrmion profiles are generally narrower than the experimental ones. This becomes particularly apparent by the difference images shown in figure 5.20(d) and can be explained by the additional influence of magnetic volume charges as mentioned above in footnote 2, page 90. For the upper skyrmion of group A which has a circular shape, the difference image shows a ring-like structure confirming that the radius of the simulated skyrmion is smaller than that obtained from the experimental data. For the skyrmions that have an elliptical shape (lower one of group A and that of group B) the model profile matches well the experimental profile taken along the short axis of the ellipsis (see sections in figure 5.21(c),(d) and 5.21(e), (f) ). This explains the two lobes visible in center and right image of figure 5.20(e). Note that a more conventional approach would be to minimize the least square deviation between the simulated and measured $\Delta f_1$ pattern of the skyrmion. A better match of the simulated and measured skyrmion profiles would then be obtained, but the simulated center contrast would become too large. The least square method is not used because the it would average between the long and short radius in the case of elliptically shaped skyrmions such that neither the short nor the long elliptical axis would be well matched.

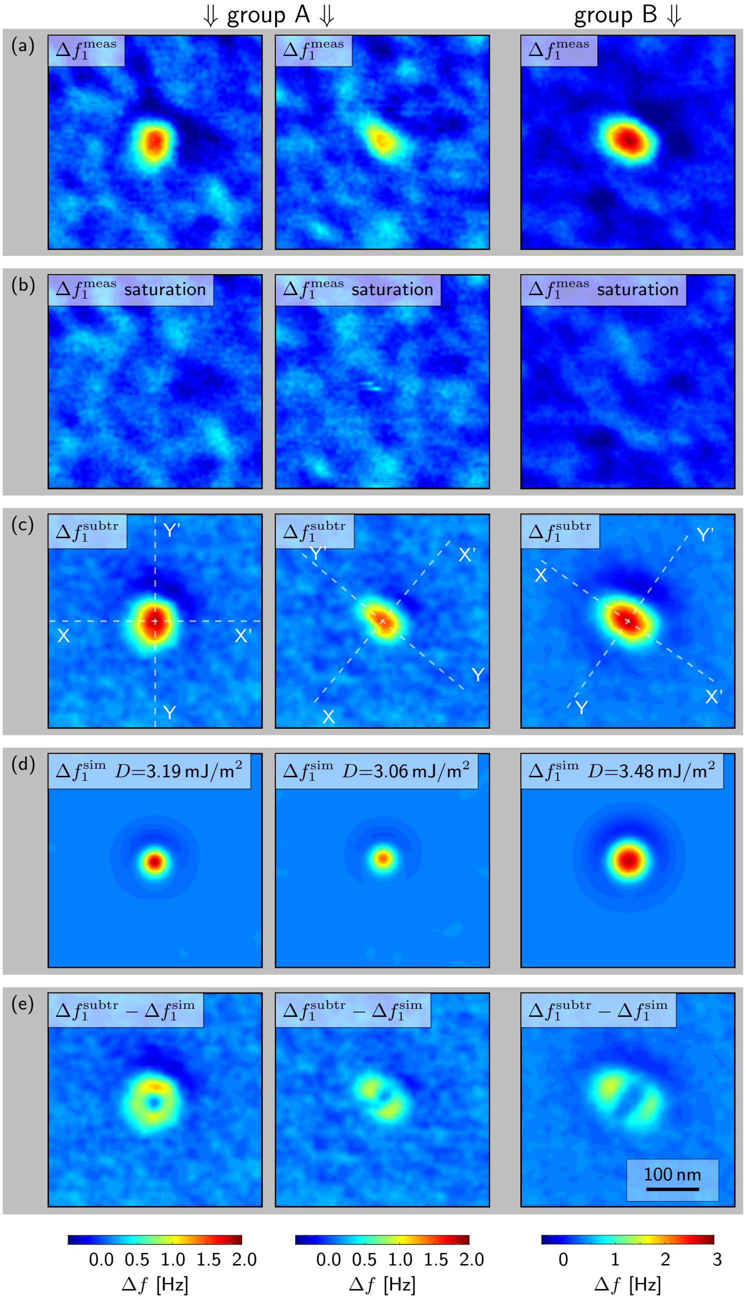

Figure 5.20: Comparison of the measured ($\Delta f_1^{\mathrm{meas}}$) and simulated frequency shift ($\Delta f_1^{\mathrm{sim}}$) for the upper and lower skyrmions of group A and the skyrmion of group B. (a): measured frequency shift $\Delta f_1$ for the upper (left image) and lower (center image) skyrmion of group A and the skyrmion of group B (right image). (b): frequency shift measured in saturation for the same sample areas as (a). (c): background subtracted data $\Delta f_1^{\mathrm{subtr}}$ i.e. the differences of (a) and (b). (d): frequency shift $\Delta f_1^{\mathrm{sim}}$ for the individual skyrmions simulated with $D = 3.19,\ 3.06,$ and $3.48$ mJ/m$^2$ for the upper/lower skyrmion of group A and for the skyrmion of group B, respectively. (e): difference between the background subtracted measurement data in (c) and the simulations in (d).

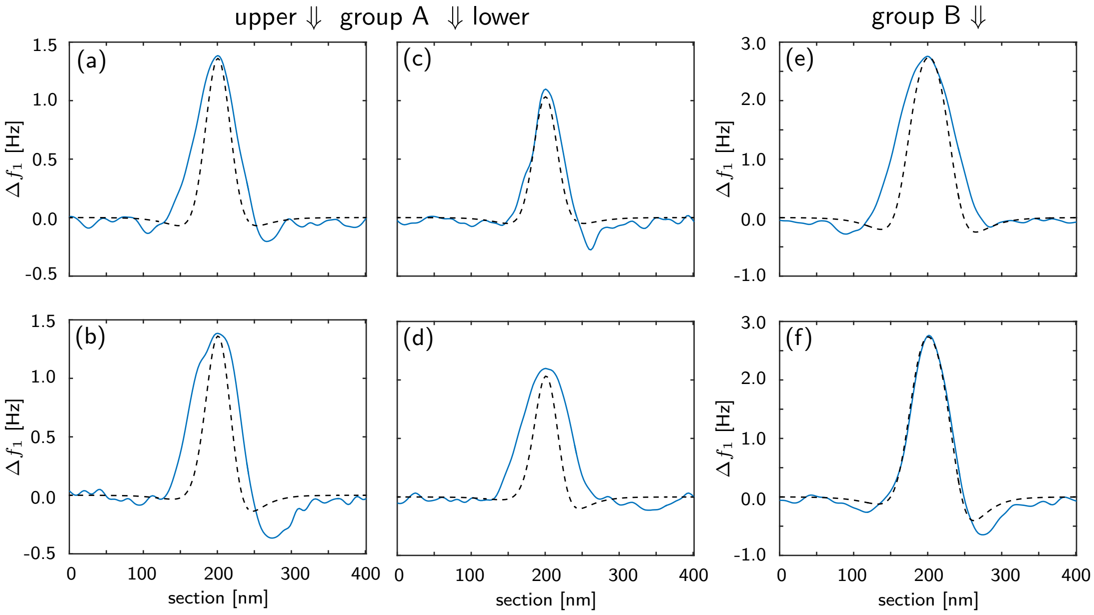

Figure 5.21: Comparison of measurement (blue lines) and simulation (dashed lines) at the locations indicated in figure 5.20(c). The data for the upper skyrmion of group A is shown in the panels (a) and (b), for the lower one in panels (c) and (d). The data for the skyrmion of group B is shown in panels (e) and (f). Panels (a), (c) and (e) show the sections X-X', panels (b), (d) and (f) the sections Y-Y'.

## 5.11 Conclusions

High sensitivity MFM performed in vacuum with capacitive tip sample distance control (chapter 4) was used to study the evolution of the micromagnetic state and to image skyrmions with a so far unmatched SNR that also surpasses that of XMCD Photoemission Electron Microscopy (PEEM) measurements of skyrmions performed by Moreau-Luchaire et al.[8]. A novel method for the determination of the average DM interaction from the near-equilibrium domain structure of the sample ASI was developed. The average value of $D = 2.04$ mJ/m$^2$ is higher than the $D = 1.6 \pm 0.2$ mJ/m$^2$ found by Moreau-Luchaire et al. . To date it remains unclear whether this higher values arise from a better interface quality of the sample ASI that consists of only five repeats of Pt/Co/Ir compared to the ten repeats used in Ref.[8], or results from the improved analysis method developed here.

MFM images of skyrmions performed after repeated saturation processes revealed that the skyrmions re-nucleate at a few specific locations of the film indicating that these may have distinct physical properties. High-resolution images of these skyrmions revealed that their MFM contrast varies substantially between 1.1 Hz and 2.8 Hz, and that some skyrmions have an elliptical shape. Local $D$-values could be obtained from fitting model calculations to the measured data. These $D$-values varied between $D = 3.06$ mJ/m$^2$ and $D = 3.48$ mJ/m$^2$ and are thus considerably larger than the $D_{\text{avg}} = 2.04$mJ/m$^2$ determined from an analysis of the equilibrium domain size.

Apart from the skyrmions, a background contrast that remains constant in all applied fields was observed. Using quantitative MFM methods (section 1.3) the spatial variation of the areal magnetic moment density could be determined. The latter corresponds to a simultaneous standard deviation of all Co layers equivalent to approximately 0.3 monolayers (ML), while the minimum-maximum span is about ±1.2 ML. According to ab-initio calculations by Yang et al.[57] performed for Co/Pt interfaces, the DM interaction varies between 2.59 mJ/m$^2$ and 3.72mJ/m$^2$ for 3 and 2 ML of Co on 3 ML of Pt. The span of local $D$-values determined from the presented MFM data is thus contained in the $D$-span from Ref.[57]. From this we conclude that in our films, skyrmions appear solely at location with higher

$D$-values presumably arising from locally thinner $Co$ layers. Consequently these skyrmions are well pinned, because they can only exist at film locations providing sufficiently high DM interaction. This explains that to date the current densities required to manipulate skyrmions in multilayer systems with interfacial DM interaction were found to be orders of magnitude higher than those found in single crystalline materials.

# 6 Summary and Outlook

Two novel methods for controlling the tip-sample distance for MFM based on bimodal cantilever excitation modes were developed. With these, the topography and magnetic stray field emanating from the surface of a sample can be simultaneously measured in a single passage. Moreover these modes are compatible with operation in vacuum and prevent the use of typical lift-mode operation relying on intermittent contact mode for mapping the topography of the sample.

The first method discussed in chapter 3 makes use of different decay lengths of magnetic and van der Waals forces acting between tip and sample. A stable MFM operation at tip sample distances of only a few nanometers becomes possible resulting in highest lateral magnetic resolution that can be better than 10 nm. However, this method is limited to small tip sample distances where the van der Waals forces become sufficiently large. This limitation is overcome by the second distance control method presented in chapter 4. It uses the tip sample capacity as a proxy for the sample's topography and allows MFM measurements performed with the tip tracing the local topography of the sample or with a tip sample distance that is kept constant in average. Both operation modes are suitable for measurements in externally applied B-fields, as long as possible field induced changes of the quality factor are considered and the corresponding feedback setpoints are adjusted. The operation at constant average height is preferred, when a later quantitative analysis of the MFM data is considered. The theoretical background of quantiative MFM, and the tip calibration procedures used here are reviewed in section 1.3.

In chapter 5 these data analysis and measurement techniques have been applied to study multilayer ferromagnetic samples with perpendicular anisotropy and interfacially induced DM interaction fabricated with a commercial UHV sputter deposition system. A summary of the obtained results has been given in section 5.11.

# Outlook

## Capacitive distance feedback method

The capacitive distance feeback method presented in chapter 4 requires that the second mode quality factor remains constant at least during the acquisition of one image, and preferably over a longer period of time. The second mode quality factor can however be affected by dissipative tip sample interaction forces, or by dissipation of the cantilever motion occurring in large magnetic fields. As discussed in sections 4.2 and 5.6 a change of the second mode quality factor will result in a corresponding change of the tip sample distance.

A future development is to modulate the electrostatic tip sample force at lower frequencies and to use the amplitude of the second side band of the fundamental mode resonance for distance control. The side band amplitude is not affected by changes of the quality factor if the amplitude of the fundamental mode mode resonance is kept constant by the amplitude feedback of the PLL.

## Calibration sample for quantitative MFM

The calibration of the MFM tip is an essential step for the quantitative analysis of MFM data. In order to determine the $TF$ for high spacial frequencies a sample with sharp changes of the magnetization direction are required. In the Co/Pt multilayer sample which has been used for the calibration in this thesis, the width of the domain walls is determined by the anisotropy and exchange constants of the continuous Co layers. Sharper transitions could be obtained in films with decoupled magnetic grains. This can be achieved by the co-deposition of Chromium together with the Co, and a subsequent annealing of the sample. The annealing process drives the Cromium to the boundaries of the Co grains such that the inter-granular exchange coupling is broken.

In addition, a further improvement of the surface roughness is required to acquire MFM images at tip-sample distances considerably below 10 nm. New sputter deposition methods and epitaxially grown samples are envisoned to obtain lower surface roughness.

### Improved signal to noise ratio

To date, the process used to deposit magnetic material onto the tip, also coats the Si cantilever. Although the latter layer is significantlly thinner than that on the tip (section 2.2), the quality factor of the cantilever is lowered from about 150’000 to 200’000 down to about 50’000. The next cantilever substrate holder will include a shadow mask and a positioning unit to prevent the coating of the cantilever.

### Improved multilayer materials with interfacial DM interaction

As discussed in section 5.11 the variation of the thickness of the ferromagnetic layers in multilayers with interfacial DM interaction gives rise to substantial spatial variations of the latter. This leads to pinning of the skyrmions such that large current densities are required for the manipulation of the skyrmions.

Future developments aim at the development of multilayers with atomically controlled thicknesses of the ferromagnetic layers and the design of interfaces providing strong homogeneous DM interaction.

# List of Figures

# Bibliography

[1] J. Schwenk, M. Marioni, S. Romer, N. R. Joshi, and H. J. Hug. Non-contact bimodal magnetic force microscopy. *Applied Physics Letters*, 104(11):112412, March 2014.

[2] J. Schwenk, X. Zhao, M. Bacani, M. A. Marioni, S. Romer, and H. J. Hug. Bimodal magnetic force microscopy with capacitive tip-sample distance control. *Applied Physics Letters*, 107(13):132407, September 2015.

[3] Nicolas Pilet. *The relation between magnetic hysteresis and the micromagnetic state explored by quantitative magnetic force microscopy.* PhD thesis, University of Basel, 2006.

[4] Ernst Meyer, Hans Josef Hug, and Roland Bennewitz. *Scanning Probe Microscopy.* Advanced Texts in Physics. Springer Berlin Heidelberg, Berlin, Heidelberg, 2004.

[5] P. Kappenberger, S. Martin, Y. Pellmont, H. J. Hug, J. B. Kortright, O. Hellwig, and Eric E. Fullerton. Direct Imaging and Determination of the Uncompensated Spin Density in Exchange-Biased CoO/(CoPt) Multilayers. *Physical Review Letters*, 91(26), December 2003.

[6] Sumio Hosaka, Atsushi Kikukawa, Yukio Honda, Hajime Koyanagi, and Shinji Tanaka. Simultaneous Observation of 3-Dimensional Magnetic Stray Field and Surface Structure Using New Force Microscope. *Japanese Journal of Applied Physics*, 31(Part 2, No. 7A):L904–L907, July 1992.

[7] R. Giles, J. P. Cleveland, S. Manne, P. K. Hansma, B. Drake, P. Maivald, C. Boles, J. Gurley, and V. Elings. Noncontact force microscopy in liquids. *Applied Physics Letters*, 63(5):617, 1993.

[8] C. Moreau-Luchaire, C. Moutafis, N. Reyren, J. Sampaio, C. A. F. Vaz, N. Van Horne, K. Bouzehouane, K. Garcia, C. Deranlot, P. Warnicke, P. Wohlhüter, J.-M. George, M. Weigand, J. Raabe, V. Cros, and A. Fert. Additive interfacial chiral interaction in multilayers for stabilization of small individual skyrmions at room temperature. *Nature Nanotechnology*, January 2016.

[9] Gerd Binnig, Calvin F. Quate, and Ch Gerber. Atomic force microscope. *Physical review letters*, 56(9):930, 1986.

[10] Gary M. McClelland, Ragnar Erlandsson, and Shirley Chiang. Atomic force microscopy: General principles and a new implementation. In *Review of progress in quantitative nondestructive evaluation*, pages 1307–1314. Springer, 1987.

[11] D. Rugar, H. J. Mamin, P. Guethner, S. E. Lambert, J. E. Stern, I. McFadyen, and T. Yogi. Magnetic force microscopy: General principles and application to longitudinal recording media. *Journal of Applied Physics*, 68(3):1169, 1990.

[12] Y. Martin, C. C. Williams, and H. K. Wickramasinghe. Atomic force microscope–force mapping and profiling on a sub 100-Å scale. *Journal of Applied Physics*, 61(10):4723, 1987.

[13] E. Volterra and E. C. Zachmanoglou. *Dynamics of Vibrations*. Charles E. Merrill Books, Columbus, 1965.

[14] U. Rabe, K. Janser, and W. Arnold. Vibrations of free and surface-coupled atomic force microscope cantilevers: Theory and experiment. *Review of Scientific Instruments*, 67(9):3281, 1996.

[15] Dieter Meschede. *Gerthsen Physik*. Springer-Lehrbuch. Springer Berlin Heidelberg, Berlin, Heidelberg, 2015.

[16] Charles A Clifford and Martin P Seah. The determination of atomic force microscope cantilever spring constants via dimensional methods for nanomechanical analysis. *Nanotechnology*, 16(9):1666–1680, September 2005.

[17] Arnold F. Holleman, Egon Wiberg, and Nils Wiberg. *Lehrbuch der anorganischen Chemie.* de Gruyter, Berlin, 102 edition, 2007.

[18] Matthew A. Hopcroft, William D. Nix, and Thomas W. Kenny. What is the Young's Modulus of Silicon? *Journal of Microelectromechanical Systems*, 19(2):229–238, April 2010.

[19] John Melcher, Shuiqing Hu, and Arvind Raman. Equivalent point-mass models of continuous atomic force microscope probes. *Applied Physics Letters*, 91(5):053101, 2007.

[20] Kevin Y. Yasumura, Timothy D. Stowe, Eugene M. Chow, Timothy Pfafman, Thomas W. Kenny, Barry C. Stipe, and Daniel Rugar. Quality factors in micron-and submicron-thick cantilevers. *Microelectromechanical Systems, Journal of*, 9(1):117–125, 2000.

[21] Joachim Welker, Esther Illek, and Franz J Giessibl. Analysis of force-deconvolution methods in frequency-modulation atomic force microscopy. *Beilstein Journal of Nanotechnology*, 3:238–248, March 2012.

[22] H.-J. Butt and Manfred Jaschke. Calculation of thermal noise in atomic force microscopy. *Nanotechnology*, 6(1):1, 1995.

[23] Franz J. Giessibl. Advances in atomic force microscopy. *Reviews of modern physics*, 75(3):949, 2003.

[24] Sascha Sadewasser and Thilo Glatzel, editors. *Kelvin Probe Force Microscopy*, volume 48 of *Springer Series in Surface Sciences.* Springer Berlin Heidelberg, Berlin, Heidelberg, 2012.

[25] S. Hudlet, M. Saint Jean, C. Guthmann, and J. Berger. Evaluation of the capacitive force between an atomic force microscopy tip and a metallic surface. *The European Physical Journal B-Condensed Matter and Complex Systems*, 2(1):5–10, 1998.

[26] M. Guggisberg, M. Bammerlin, Ch. Loppacher, O. Pfeiffer, A. Abdurixit, V. Barwich, R. Bennewitz, A. Baratoff, E. Meyer, and H.-J. Güntherodt.

Separation of interactions by noncontact force microscopy. *Physical Review B*, 61(16):11151–11155, April 2000.

[27] Hans J. Hug, B. Stiefel, P. J. A. van Schendel, A. Moser, R. Hofer, S. Martin, H.-J. Güntherodt, Steffen Porthun, Leon Abelmann, J. C. Lodder, Gabriel Bochi, and R. C. O'Handley. Quantitative magnetic force microscopy on perpendicularly magnetized samples. *Journal of Applied Physics*, 83(11):5609, 1998.

[28] J.D. Jackson and K. Müller. *Klassische Elektrodynamik*. de Gruyter, 2002.

[29] Tim Williams. *EMC for product designers*. Newnes, Oxford, 2007.

[30] David Brown, David Harrold, and Roger Hope. *Control engineering: control system power and grounding better practice*. Newnes, Amsterdam ; Boston, 2004.

[31] Felipe Aguilar Sandoval, Mickael Geitner, Éric Bertin, and Ludovic Bellon. Resonance frequency shift of strongly heated micro-cantilevers. *Journal of Applied Physics*, 117(23):234503, June 2015.

[32] Jason W. Li, Jason P. Cleveland, and Roger Proksch. Bimodal magnetic force microscopy: Separation of short and long range forces. *Applied Physics Letters*, 94(16):163118, 2009.

[33] Tom\'{a}s R. Rodr\'{i}guez and Ricardo Garc\'{i}a. Compositional mapping of surfaces in atomic force microscopy by excitation of the second normal mode of the microcantilever. *Applied Physics Letters*, 84(3):449, 2004.

[34] Daniel Forchheimer, Daniel Platz, Erik A. Tholén, and David B. Haviland. Simultaneous imaging of surface and magnetic forces. *Applied Physics Letters*, 103(1):013114, 2013.

[35] M. J. Higgins, R. Proksch, J. E. Sader, M. Polcik, S. Mc Endoo, J. P. Cleveland, and S. P. Jarvis. Noninvasive determination of optical lever sensitivity in atomic force microscopy. *Review of Scientific Instruments*, 77(1):013701, 2006.

[36] F.J. Giessibl, H. Bielefeldt, S. Hembacher, and J. Mannhart. Imaging of atomic orbitals with the Atomic Force Microscope — experiments and simulations. *Annalen der Physik*, 10(11-12):887–910, November 2001.

[37] Shigeki Kawai, Thilo Glatzel, Sascha Koch, Bartosz Such, Alexis Baratoff, and Ernst Meyer. Time-averaged cantilever deflection in dynamic force spectroscopy. *Physical Review B*, 80(8), August 2009.

[38] P. J. A. van Schendel, H. J. Hug, B. Stiefel, S. Martin, and H.-J. Güntherodt. A method for the calibration of magnetic force microscopy tips. *Journal of Applied Physics*, 88(1):435, 2000.

[39] I. Schmid, M. A. Marioni, P. Kappenberger, S. Romer, M. Parlinska-Wojtan, H. J. Hug, O. Hellwig, M. J. Carey, and E. E. Fullerton. Exchange Bias and Domain Evolution at 10 nm Scales. *Physical Review Letters*, 105(19), November 2010.

[40] D. Rugar, B.C. Stipe, H.J. Mamin, C.S. Yannoni, T.D. Stowe, K.Y. Yasumura, and T.W. Kenny. Adventures in attonewton force detection. *Applied Physics A*, 72(S1):S3–S10, March 2001.

[41] L. Piraux, V. A. Antohe, F. Abreu Araujo, S. K. Srivastava, M. Hehn, D. Lacour, S. Mangin, and T. Hauet. Periodic arrays of magnetic nanostructures by depositing Co/Pt multilayers on the barrier layer of ordered anodic alumina templates. *Applied Physics Letters*, 101(1):013110, 2012.

[42] T. Hauet, L. Piraux, S. K. Srivastava, V. A. Antohe, D. Lacour, M. Hehn, F. Montaigne, J. Schwenk, M. A. Marioni, H. J. Hug, O. Hovorka, A. Berger, S. Mangin, and F. Abreu Araujo. Reversal mechanism, switching field distribution, and dipolar frustrations in Co/Pt bit pattern media based on auto-assembled anodic alumina hexagonal nanobump arrays. *Physical Review B*, 89(17), May 2014.

[43] A. N. Bogdanov and D. A. Yablonskii. Thermodynamically stable" vortices" in magnetically ordered crystals. The mixed state of magnets. *Zh. Eksp. Teor. Fiz*, 95:182, 1989.

[44] Naoto Nagaosa and Yoshinori Tokura. Topological properties and dynamics of magnetic skyrmions. *Nature Nanotechnology*, 8(12):899–911, December 2013.

[45] Tony Hilton Royle Skyrme. A unified field theory of mesons and baryons. *Nuclear Physics*, 31:556–569, 1962.

[46] Albert Fert, Vincent Cros, and Joao Sampaio. Skyrmions on the track. *Nat Nano*, 8(3):152–156, March 2013.

[47] R. Tomasello, E. Martinez, R. Zivieri, L. Torres, M. Carpentieri, and G. Finocchio. A strategy for the design of skyrmion racetrack memories. *Scientific Reports*, 4:6784, October 2014.

[48] S. Mühlbauer, B. Binz, F. Jonietz, C. Pfleiderer, A. Rosch, A. Neubauer, R. Georgii, and P. Böni. Skyrmion lattice in a chiral magnet. *Science*, 323(5916):915–919, 2009.

[49] X. Z. Yu, Y. Onose, N. Kanazawa, J. H. Park, J. H. Han, Y. Matsui, N. Nagaosa, and Y. Tokura. Real-space observation of a two-dimensional skyrmion crystal. *Nature*, 465(7300):901–904, June 2010.

[50] Niklas Romming, Christian Hanneken, Matthias Menzel, Jessica E. Bickel, Boris Wolter, Kirsten von Bergmann, André Kubetzka, and Roland Wiesendanger. Writing and Deleting Single Magnetic Skyrmions. *Science*, 341(6146):636–639, August 2013.

[51] Seonghoon Woo, Kai Litzius, Benjamin Krüger, Mi-Young Im, Lucas Caretta, Kornel Richter, Maxwell Mann, Andrea Krone, Robert Reeve, Markus Weigand, and others. Observation of room temperature magnetic skyrmions and their current-driven dynamics in ultrathin Co films. *arXiv preprint arXiv:1502.07376*, 2015.

[52] S. Rohart and A. Thiaville. Skyrmion confinement in ultrathin film nanostructures in the presence of Dzyaloshinskii-Moriya interaction. *Physical Review B*, 88(18), November 2013.

[53] M. Heide, G. Bihlmayer, and S. Blügel. Dzyaloshinskii-Moriya interaction accounting for the orientation of magnetic domains in ultrathin films: Fe/W(110). *Physical Review B*, 78(14), October 2008.

[54] A. Fert and Peter M. Levy. Role of anisotropic exchange interactions in determining the properties of spin-glasses. *Physical Review Letters*, 44(23):1538, 1980.

[55] Gong Chen, Tianping Ma, Alpha T. N'Diaye, Heeyoung Kwon, Changyeon Won, Yizheng Wu, and Andreas K. Schmid. Tailoring the chirality of magnetic domain walls by interface engineering. *Nature Communications*, 4, October 2013.

[56] Gong Chen, Alpha T. N'Diaye, Yizheng Wu, and Andreas K. Schmid. Ternary superlattice boosting interface-stabilized magnetic chirality. *Applied Physics Letters*, 106(6):062402, February 2015.

[57] Hongxin Yang, André Thiaville, Stanislas Rohart, Albert Fert, and Mairbek Chshiev. Anatomy of Dzyaloshinskii-Moriya Interaction at Co / Pt Interfaces. *Physical Review Letters*, 115(26), December 2015.

[58] Olivier Boulle, Jan Vogel, Hongxin Yang, Stefania Pizzini, Dayane de Souza Chaves, Andrea Locatelli, Tevfik Onur Mente?, Alessandro Sala, Liliana D. Buda-Prejbeanu, Olivier Klein, Mohamed Belmeguenai, Yves Roussigné, Andrey Stashkevich, Salim Mourad Chérif, Lucia Aballe, Michael Foerster, Mairbek Chshiev, Stéphane Auffret, Ioan Mihai Miron, and Gilles Gaudin. Room-temperature chiral magnetic skyrmions in ultrathin magnetic nanostructures. *Nature Nanotechnology*, 11(5):449–454, January 2016.

[59] Yonko Millev. Bose-Einstein integrals and domain morphology in ultrathin ferromagnetic films with perpendicular magnetization. *Journal of Physics: Condensed Matter*, 8(20):3671, 1996.

[60] Dang Duc Trong, Cao Xuan Phuong, Truong Trung Tuyen, and Dinh Ngoc Thanh. Tikhonov's Regularization to the Deconvolution Problem. *Communications in Statistics - Theory and Methods*, 43(20):4384–4400, October 2014.

[61] A. Tikhonov. Solution of incorrectly formulated problems and the regularization method. In *Soviet Math. Doklady*, volume 4, pages 1035–1038, 1963.

[62] William H. Press, Saul A. Teukolsky, William T. Vetterling, and Brian P. Flannery. *Numerical Recipes 3rd Edition: The Art of Scientific Computing*. Cambridge University Press, New York, NY, USA, 3 edition, 2007.

[63] A. Bogdanov and A. Hubert. Thermodynamically stable magnetic vortex states in magnetic crystals. *Journal of Magnetism and Magnetic Materials*, 138(3):255 – 269, 1994.

[64] Mirko Baćani, Miguel A. Marioni, Johannes Schwenk, and Hans J. Hug. How to measure the local Dzyaloshinskii Moriya Interaction in Skyrmion Thin Film Multilayers. *arXiv preprint arXiv:1609.01615*, 2016.

# List of acronyms

$LCF$ lever-canting-Function.

$TF$ tip-transfer-function.

**ASI** with asymmetric interfaces.

**Co** cobalt.

**CP** contact potential.

**CPD** contact potential difference.

**DAC** digital-to-analog converter.

**DM** Dzyaloshinskii-Moriya.

**Ir** iridium.

**MFM** Magnetic Force Microscopy.

**MFM** Magnetic Force Microscope.

**ML** monolayers.

**Ni** nickel.

**PEEM** Photoemission Electron Microscopy.

**PLL** Phase Locked Loop.

**PSD** position sensitive photodetector.

**Pt** platinum.

**Q** quality factor.

**SFM** Scanning Force Microscopy.

**SFM** Scanning Force Microscope.

**SI** with symmetric interfaces.

**SNR** signal-to-noise ratio.

**STM** Scanning Tunneling Microscopy.

**STXM** Scanning Transmission X-ray Microscopy.

**TEM** Transmission Electron Microscopy.

**Ti** titanium.

**UHV** ultra high vacuum.

**VSM** vibrating sample magnetometry.

**XMCD** X-ray Magnetic Circular Dichroism.

# Acknowledgments

I want to thank my supervisors at Empa, Miguel Marioni and Hans Hug for their inspiring as well as challenging advice, guidance and support throughout the past years. I will keep the hours of our enthusiastic and inspiring conversations in mind. I also want to thank you for making my thesis possible and especially for providing the freedom for my scientific creativity. I would do it again!

Thanks also to Prof. Martino Poggio for being co-referee of the thesis and Prof. Ernst Meyer who agreed to chair my defense talk.

I want to thank all my co-workers for the great atmosphere in the lab, in the office, at the rooftop and the barbecue. Special thanks go to Sasa Vrankovic and Günther Hobi for their everlasting technical support and Mirko Bacani for carrying out the measurements of the skyrmion samples. Thanks go also to Sara Romer and Niraj Joshi who introduced me to the machines in the lab.

A warm thank you goes to my family and my parents who greatly supported my education and thus made this thesis possible to a large degree.

Most of my friends are not listed here, but be assured, we had a good time which deserves a big thank you.

Finally I want to give a heartfelt thank you to Luisa for being herself and for the time we spent and will spend together. I am looking forward!

# List of publications

- K. Muthukumar, H. O. Jeschke, R Valentí, E. Begun, J. Schwenk, F Porrati and M. Huth
  *Spontaneous dissociation of $Co_2(CO)_8$ and autocatalytic growth of Co on $SiO_2$: A combined experimental and theoretical investigation*
  Beilstein J. Nanotechnol. 2012, 3, 546–555. doi:10.3762/bjnano.3.63

- J. Schwenk, M.A. Marioni, S. Romer, H.J. Hug
  *Non-contact bimodal magnetic force microscopy*
  Applied Physics Letters 104(11), 2014 doi:10.1063/1.4869353

- T. Hauet, L. Piraux, S.K. Srivastava, V.A. Antohe, D. Lacour, M. Hehn, F. Montaigne, J. Schwenk, M.A. Marioni, H.J. Hug, O. Hovorka, A. Berger, S. Mangin, F. Abreu Araujo
  *Reversal mechanism, switching field distribution and dipolar frustrations in Co/Pt bit pattern media based on AAO auto-assembled hexagonal nanobump arrays*
  Physical Review B 89(17):174421 2014 doi:10.1103/PhysRevB.89.174421

- A. Benassi, J, Schwenk, M. A. Marioni, H. J. Hug, D. Passerone
  *Microscale Motion Control through Ferromagnetic Films*
  Advanced Materials Interfaces 1(4) 2014 doi:10.1002/admi.201400023

- T. Jäger, Y. E. Romanyuk, B. Bissig, F. Pianezzi, S. Nishiwaki, P. Reinhard, J. Steinhauser, J. Schwenk, A. N. Tiwari
  *Improved open-circuit voltage in Cu(In,Ga)Se2 solar cells with high work function transparent electrodes*
  Journal of Applied Physics 117(22):225303 2015 doi:10.1063/1.4922351

- J. Schwenk, X. Zhao, M. Baćani, M. A. Marioni, S. Romer, H. J. Hug
  *Bimodal Magnetic Force Microscopy with Capacitive Tip-Sample Distance Control*
  Applied Physics Letters 107(13) 2015 doi:10.1063/1.4932174